High resolution whole heart T1 mapping

Nordio, Giovanna

Awarding institution:
King's College London

King's College of London

High resolution whole heart T1 mapping

Giovanna Nordio

Supervised by
Professor René M. Botnar
Dr. Markus Henningsson

Thesis submitted to King's College of London
for the degree Doctor of Philosophy
September 2018

Abstract

Myocardial fibrosis is one of the most common manifestations of several cardiomyopathies and one of the main predictors of future cardiac events. Magnetic resonance imaging has been established as an emerging and powerful modality for the differentiation between healthy and non-healthy myocardium in a broad spectrum of cardiac diseases. Late gadolinium enhancement (LGE) is the reference technique for the visualization of myocardial scar and focal fibrosis, however it cannot visualize diffuse fibrosis. In contrast, quantitative myocardial T1 mapping allows the detection of both local and diffuse fibrosis, and it has been investigated as a potential new diagnostic tool for the assessment of different cardiomyopathies. Several T1 mapping techniques have been proposed in the last ten years, which are mostly restricted to two-dimensional (2D) imaging with limited spatial resolution, allowing the acquisition of a single slice in one breath-hold. In contrast, free-breathing three-dimensional (3D) quantitative T1 mapping benefits from a complete myocardial coverage with higher signal-to-noise ratio (SNR) and spatial resolution than a 2D acquisition. However, 3D acquisitions require longer scan time and consequently a free-breathing acquisition is mandatory.

In this work a new 3D saturation recovery T1 mapping technique, called 3D SASHA, is presented, which provides whole-heart coverage during free-breathing. For respiratory motion compensation a 1D diaphragmatic navigator was used. However, this approach may only achieve a scan efficiency of approximately 50%, prolonging the scan time considerably. To shorten the acquisition a new solution is proposed, which instead combines the 3D SASHA imaging sequence with a 2D fat image navigator (fat-iNAV) for respiratory motion compensation. Motion estimation from the fat-iNAV may be more robust as image contrast using fat excitation is less affected by signal changes caused by the different saturation times compared to a water signal based navigator due to the short

T1 of fat. The proposed fat-iNAV permits to estimate the respiratory motion of the heart with a higher accuracy, allowing 100% respiratory scan efficiency and predictable scan time.

Another important aspect of the myocardial T1 mapping technique is to ensure an optimal trade-off between accuracy and precision. 3D SASHA imaging technique has shown higher accuracy in the estimation of the myocardial T1 than the clinically used inversion recovery based 2D MOLLI technique, but has lower precision. Here, a new approach is proposed, which combines the 3D SASHA sequence with a post-processing 3D Beltrami denoising method to improve the precision while maintaining the accuracy. After denoising, the precision of the 3D SASHA myocardial T1 mapping is substantially improved and is similar to that of 2D MOLLI T1 mapping, while preserving the higher accuracy and whole coverage of 3D SASHA. In addition, the proposed 3D Beltrami denoising approach is used to accelerate the 3D SASHA acquisition by reducing the number of T1-weighted images (from nine to three) used for the fitting process without affecting the accuracy and precision of the T1 map.

Acknowledgements

During these years in London and at King's College I have been extremely lucky to meet so many great people, who have made the PhD a wonderful journey.

This research would not have been possible without the help and support of my supervisors, Professor René Botnar and Dr Markus Henningsson. Thank you for sharing with me your immense knowledge, for believing on my work and for guiding me through the PhD.

I would like to thank Dr Torben Schneider, for always answering my questions and for being my mentor with the scanner.

I would like to thank Gastao, Aurelien, Teresa and Imran, for helping me with the correction of the thesis.

I would like to thank all my colleagues from the KCL group, for the help, support and company during these years. And of course thank you for sharing with me your heart at the scanner.

Thank you to all my friends, in Italy and all around the world. It is wonderful to know you have so many people who love you, despite the distance.

Thank you Manu, my positive energy, for always being there.

Most of all, I want to thank my family, who supports and loves me unconditionally.

The work in this dissertation was supported by King's College London & Imperial College London EPSRC Centre for Doctoral Training in Medical Imaging (EP/L015226/1).

Contents

List of figures

List of tables

List of abbreviations

1D	One-Dimensional
1D-NAV	One-Dimensional Navigator
2D	Two Dimensional
3D	Three Dimensional
AHA	American Heart Association
ARA	accept-reject algorithm
bSSFP	balanced Steady-State Free Precession
CMR	Cardiac Magnetic Resonance
ECG	Electrocardiogram
ECM	Extracellular matrix
ECV	Extracellular volume
fat-iNAV	Fat image-based navigator
FA	Flip angle
FFT	Fourier transform
FOV	Field of view
FH	Foot-Head
GRAPPA	Generalized autocallibrating partially parallel
GRE	Gradient echo
iNAV	Image-based navigator
LGE	Late Gadolinium Enhancement
LL	Look-Locker
MI	Myocardial Infarction
MOLLI	Modified Look-Locker Inversion recovery
MRI	Magnetic Resonance Imaging
MT	Magnetization Transfer
PD	Proton density
RF	Radiofrequency
RL	Right-Left
ROI	Region of interest

SASHA	Saturation recovery single-shot acquisition
SD	Standard deviation
SNR	Signal-to-noise ratio
SE	Spin Echo
T1	spin-lattice relaxation
T2	spin-spin relaxation
TD	Delay Time
TE	Echo Time
TI	Inversion Time
TR	Repetition Time
TS	Saturation Time
TV	Total Variation
VCG	Vector electrocardiogram

Chapter 1

1.1 Introduction

Myocardial fibrosis is one of the most common manifestations of several cardiomyopathies and one of the main predictors of future cardiac events (1). Therefore, an imaging technique that permits imaging the heart, assessment of myocardial fibrosis and monitoring of disease progression non-invasively would be of great clinical interest. Cardiac magnetic resonance (CMR) is a non-invasive imaging modality that is currently widely used in clinical practice, since it provides both anatomical and functional information, as well as information on tissue composition, with high image resolution (2). The use of gadolinium-based extracellular contrast agents allows for assessment of myocardial ischemia and infarction and also aids the identification of tissue composition. First pass perfusion imaging using saturation recovery sequences enables the qualitative and quantitative assessment of myocardial perfusion with high spatial resolution and good coverage. Late gadolinium enhancement (LGE) sequences are routinely used to identify the presence of myocardial fibrosis or infarction, where the extent of scar trasmurality provides valuable information about myocardial viability in cases of ischaemic

cardiomyopathy (3). However, LGE CMR is unable to reliably detect diffuse fibrosis that can be present in conditions such as hypertrophic cardiomyopathy or amyloidosis. In addition recent studies have shown that after contrast enhanced magnetic resonance imaging (MRI) there is risk of gadolinium deposition in the brain (4), enforcing the need of a free-contrast imaging technique. To identify diffuse fibrosis, an alternative approach has been proposed, called myocardial T1 mapping, which allows for differentiation between normal and fibrotic myocardium based on their water content (native T1 mapping). T1 refers to the longitudinal magnetization relaxation, which is a physical property of tissue, and is increased in the presence of fibrosis compared to healthy myocardium. T1 mapping in combination with a gadolinium-based contrast agent and with the knowledge of the blood haematocrit value permits the assessment of the extracellular volume (ECV), which has been shown to be in good agreement with collagen deposition, typically observed in myocardial fibrosis. While both pre- and post-contrast T1 values are field and sequence dependent, ECV is field strength independent but depends on the accurate knowledge of the blood haematocrit value.

In the past 20 years different techniques have been proposed for myocardial T1 mapping, which utilise either inversion recovery or saturation recovery radiofrequency pulses or a combination of both to generate a series of images with T1-weighted contrast, which will be discussed in detail in chapter 3 (5–7). The MOdified Look-Locker Inversion recovery (MOLLI) and the Saturation Recovery Single-Shot Acquisition (SASHA) are two of the main techniques for myocardial T1 mapping. These techniques acquire single shot 2D images with different T1 weighting, allowing imaging a single slice of the heart in one breath-hold. The slow acquisition speed of standard MRI sequences only permits acquisition of a single 2D slice in one breath-hold. However, recent studies have shown

the possibility of acquiring multiple slices in a single breath-hold by using multislice excitation pulses (8).

A free-breathing 3D imaging technique for myocardial T1 mapping would be preferable since this could allow for improvements in image resolution, and complete volumetric coverage of the heart, providing clinicians with a potentially better understanding and visualization of disease processes and the anatomical association/proximity to key structures such as the coronary vasculature.

There are still some limitations that prevent the implementation of high resolution 3D imaging, such as spatial resolution, heart rate variability and respiratory motion. For respiratory motion, usually a navigator gating approach is used, which tracks the displacement of the lung-liver interface and to gate the data to end-expiration using an accept-reject algorithm, which will be explained in Chapter 4.

Another important aspect to consider with myocardial T1 mapping is the trade-off between good quantification accuracy, precision and reproducibility. An ideal myocardial T1 mapping technique should provide good accuracy, precision and reproducibility at the same time (9). 2D MOLLI provides precise but inaccurate T1 measurements, while 2D SASHA is more accurate but less precise than 2D MOLLI.

In summary, the current limitations of T1 mapping include 1) T1 maps require acquisition of multiple 2D slices with limited spatial resolution to cover the whole-heart, 2) respiratory motion correction in 3D acquisitions is performed with navigator gating, which often leads to long and unpredictable scans times, 3) 3D T1 mapping leads to long acquisition times as multiple T1-weighted images need to be acquired and 4) accurate and precise quantification is needed. Figure 1.1 shows a schematic diagram of the rationale behind the works presented in this PhD thesis. First I propose a novel 3D T1 mapping imaging sequence based on saturation-recovery, called 3D SASHA (10), which allows

complete volumetric coverage of the heart in free-breathing. With the proposed imaging sequence it is possible to achieve improved volumetric coverage of the heart during a free-breathing acquisition. The proposed 3D SASHA imaging sequence permits higher accuracy and improved precision, however its precision is still lower compared to 2D MOLLI (5). In order to further improve the precision of the proposed myocardial T1 mapping technique, the 3D SASHA imaging sequence was combined with a 3D post-processing denoising technique (11). A 3D denoising approach was also exploited in order to further accelerate the 3D SASHA acquisition by enabling the acquisition of fewer saturation time points. In addition, an alternative approach for respiratory motion compensation, the image-based navigation, was investigated, which allows for 100% scan efficiency in order to accelerate the acquisition and to further improve image resolution.

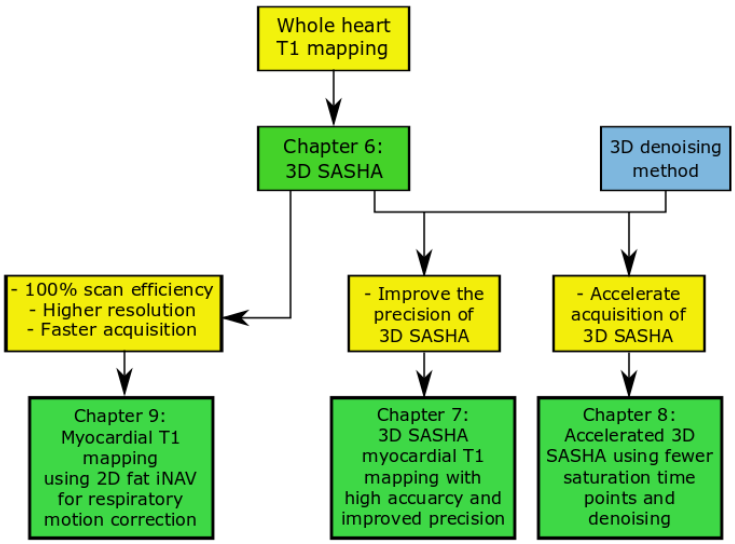

Figure 1.1: Schematic diagram of the works developed in this PhD thesis. The yellow boxes contain the aims and the justifications behind the conducted studies (green boxes). In each green box it is specified in which chapter the work is presented. The blue box contains a technique that has been used in order to in part solve the problems of precision and long scan time.

1.2 Outline of the thesis

Chapter 2 explains how the myocardium is organized and which are the main cells involved in the process of myocardial fibrosis. A clinical motivation is given to explain the importance of MRI and in particular of myocardial T1 mapping for the visualization and detection of myocardial fibrosis. Some selected clinical applications of myocardial T1 mapping are also presented.

Chapter 3 first introduces the basic concepts of MR physics. Subsequently, the basic concept of myocardial T1 mapping is introduced, including MR acquisition, magnetization preparation and data fitting. Finally, an overview of the state-of-the-art T1 mapping techniques is presented.

Chapter 4 discusses the challenges of acquisition time and introduces respiratory motion compensation and correction techniques for myocardial T1 mapping.

Chapter 5 presents image reconstruction and post-processing steps that can be performed after image acquisition, including SENSE image reconstruction, denoising techniques for T1 mapping and image analysis considerations.

Chapter 6 presents a novel motion corrected 3D T1 mapping imaging technique based on saturation recovery magnetization preparation, called 3D SASHA. The sequence was validated and tested on a T1 phantom and in healthy subjects.

Chapter 7 combines the 3D SASHA imaging technique with an extension of the 2D Beltrami regularization technique for 3D denoising. Results from a T1 phantom and in vivo data in healthy subjects are presented.

Chapter 8 proposes an approach to accelerate the 3D SASHA sequence by utilizing fewer saturation time points for data fitting, which is enabled by the 3D Beltrami denoising approach, presented in chapter 7. Results from a T1 phantom, prospective and retrospective in vivo human data are presented.

Chapter 9 combines 3D SASHA imaging sequence with a fat image-based navigator for respiratory motion compensation to achieve 100% scan efficiency. Results of the proposed approach are presented for a T1 phantom and healthy subjects.

Chapter 10 summarizes the findings of the works presented in this thesis. Future work and possible extensions of the proposed works are discussed.

Chapter 2 – Clinical motivation

2.1 The normal myocardium

The myocardium contains different types of cells including: cardiomyocytes, endothelial cells, cardiac fibroblasts, and smooth muscle cells (12). All these cells play a crucial role in maintaining the structure and functionality of the myocardium. Any alteration of the normal behaviour of these cells can cause cardiac dysfunction. In particular, cardiac fibroblasts are involved in several important cardiac processes: they maintain the homeostasis of the extracellular matrix (ECM) and the cardiac vessels, they are involved in cardiac electrical activity, and they produce cytokines and growth factors (**Error! Reference source not found.**) (13). Particularly, one of the main functions of cardiac fibroblasts is the synthesis, homeostatic maintenance and degradation of the ECM (14). ECM is an essential component in a healthy heart since it connects and surrounds the cells, (fibroblasts, myocytes, immune cells, cardiac progenitors, vascular cells and many other types), it is involved in the transmission of cardiac forces through the cardiac tissue and the mechanical signals to the single cells. In a healthy heart, the ECM and cardiac fibroblasts make up 2-4% and 6% of the structure of the myocardium, respectively (14).

After myocardial injury, an increased concentration of cardiac fibroblasts is found in the myocardium, which consequently alters the structure and functionality of the ECM. A higher amount of active cardiac fibroblasts can lead to the production and accumulation of de-novo synthesized ECM proteins, specifically an increase in extracellular collagen leading to myocardial remodelling and stiffening, called fibrosis (13). Myocardial fibrosis is one of the most common histological markers for the extent of myocardial disease. Myocardial fibrosis causes increased mechanical stiffness, diastolic and systolic dysfunction and abnormal cardiac remodelling (15). The distribution of myocardial fibrosis can appear as focal scar or diffuse ECM remodelling, which depends mainly on the underlying cause and the type of pathology (1).

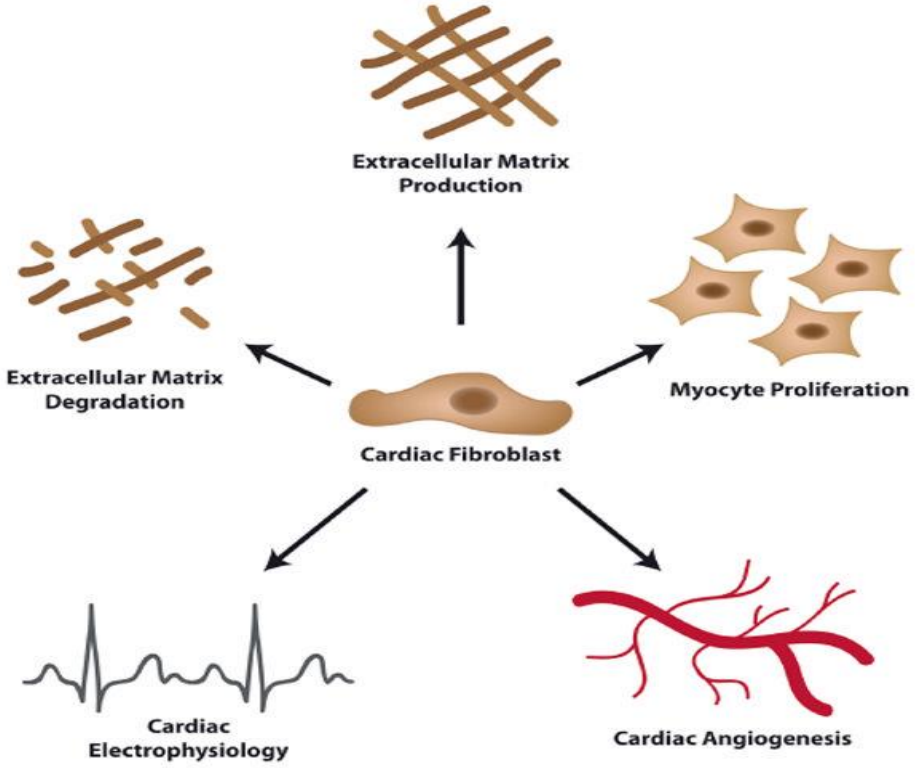

Figure 2.1: Schematic diagram illustrating the main functions of the cardiac fibroblasts (13).

Myocardial fibrosis can be classified as either replacement fibrosis or interstitial fibrosis (13). Replacement fibrosis is mainly due to the replacement of necrotic cells by the plexiform fibrosis and it can manifest itself either with local scar (ischemic

cardiomyopathy, myocarditis, sarcoidosis) or in a more diffuse pattern (hypertrophic cardiomyopathy, chronic renal insufficiency, toxic cardiomyopathies, miscellaneous inflammatory disease). In contrast interstitial fibrosis is mostly diffuse and is caused by an increased production and accumulation of collagen in the extracellular space of the myocardium (1). Such interstitial fibrosis can be present in patients with hypertension and diabetes mellitus, as well as in the aging heart and idiopathic dilated cardiomyopathy.

2.2 Myocardial tissue characterization with cardiac magnetic resonance

Originally biopsy was the only available technique to assess myocardial fibrosis. This technique allows absolute quantification of fibrosis. However, it is invasive, it has large sampling errors and carries a potential risk of complications. CMR imaging is an established non-invasive imaging modality for the assessment of the cardiac anatomy and function. In addition, CMR has been demonstrated to be an effective technique for myocardial tissue characterization using late gadolinium enhancement MRI and myocardial T1 and T2 mapping.

2.2.1 Late Gadolinium Enhancement

LGE is the clinical gold standard imaging technique to visualize the presence of scars and local fibrosis in the myocardium. LGE combines the use of a gadolinium-based contrast agent together with an inversion-recovery based technique in order to visualize the presence of myocardial scars. The technique consists of a bolus injection of gadolinium, and after 5-10 minutes T1-weighted images are acquired, described in chapter 3, with a tissue specific inversion time, which is chosen to completely null the signal from healthy myocardium. This enhances the contrast between scar and normal myocardium, as the

gadolinium-based contrast agent is trapped in scar tissue due to slower washout compared to healthy tissue (Figure 2.2).

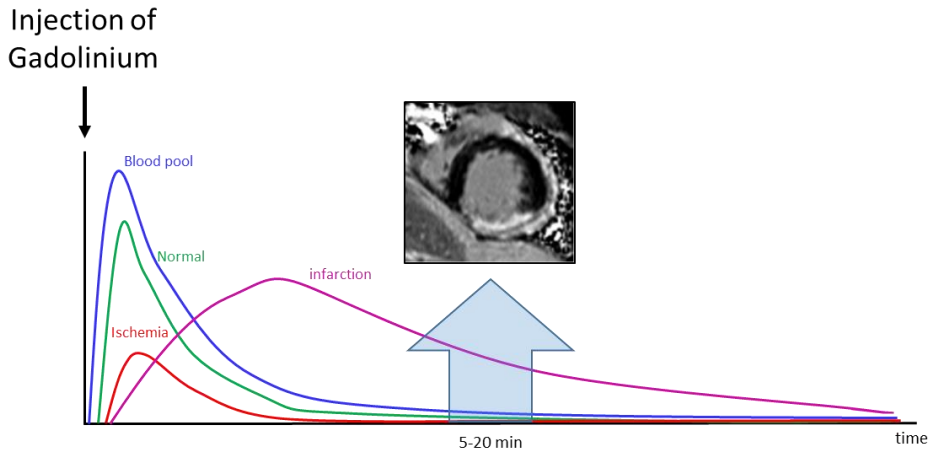

Figure 2.2: Gadolinium uptake from the different types of tissues as a function of time (adapted from (96)).

The washout of the contrast agent in fibrotic and healthy myocardium is different due to the differences in concentration of capillaries and ECM between the two tissues. Since there is a higher concentration of ECM in fibrotic tissue and reduced presence of vessels, the washout of the contrast agent will be slower. Consequently, the higher concentration of gadolinium in infarcted tissue will cause a faster T1 relaxation of the nearby protons leading to a shortening of the T1 relaxation time in the corresponding tissues. This technique is used in clinical practice to image the presence of scars both in ischemic and non-ischemic cardiomyopathies (3,15). Figure 2.3 shows different patterns of late gadolinium enhancement for different cardiomyopathies. It has been demonstrated that LGE is an effective technique to visualize the presence of myocardial scars and dense fibrosis, however diffuse fibrosis can be difficult owing to more subtle changes in the appearance of the myocardium on inversion recovery LGE imaging.

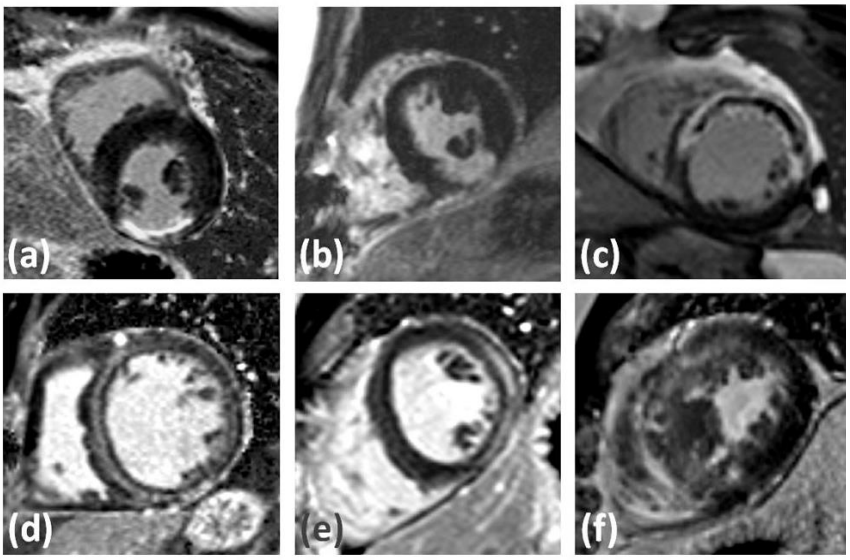

Figure 2.3: Examples of late gadolinium enhancement images: (a) sub-endocardial chronic MI, (b) transmural chronic MI, (c) acute MI with dark core due to microvascular obstruction, (d) mid-wall enhancement in patient with myocarditis, (e) sub-epicardia enhancement in patient with myocarditis, (f) scar in a patient with HCM (97).

2.2.2 T1 mapping and its clinical applications

Myocardial T1 mapping overcomes some of the limitations of the LGE technique, since it allows the detection and visualization of both dense local and diffuse fibrosis. In fact T1 mapping, enables direct signal quantification of the relaxation time T1 on a pixel-by-pixel basis, which permits differentiating between healthy and diseased tissues (16).

T1 mapping can be used pre-contrast to measure native myocardial T1, which can be advantageous in patients with renal impairment. It has been demonstrated that an increase of native T1 can be due to presence of increased water content (oedema) and increase of interstitial space (17). In contrast, a decrease of the native T1 can be related to lipid or iron overload. T1 mapping can also be performed post-contrast, and together with the knowledge of pre-contrast T1 value and the blood haematocrit, the ECV fraction can be estimated (18). ECV is an important biomarker for tissue remodeling as it estimates the interstitial space and extracellular matrix composition, which are altered in tissues affected by diffuse fibrosis (19).

Haff et. al presented an interesting overview of the clinical use of T1 mapping and ECV quantification.

Figure 2.4 demonstrates the complimentary diagnostic value of native T1 mapping and ECV quantification in various cardiac diseases. Native T1 mapping can detect and differentiate between acute and chronic myocardial infarction (MI), with higher T1 values found for acute than chronic MI (18). The combination of native T1 mapping and ECV can also be accurate techniques to detect myocarditis, as well as non-ischemic cardiomyopathies, such as amyloidosis where global patterns myocardial infiltration can sometimes impede qualitative LGE assessment. In contrast, T1 mapping is a quantitative tissue characterisation technique that allows for detection of diffuse fibrosis or

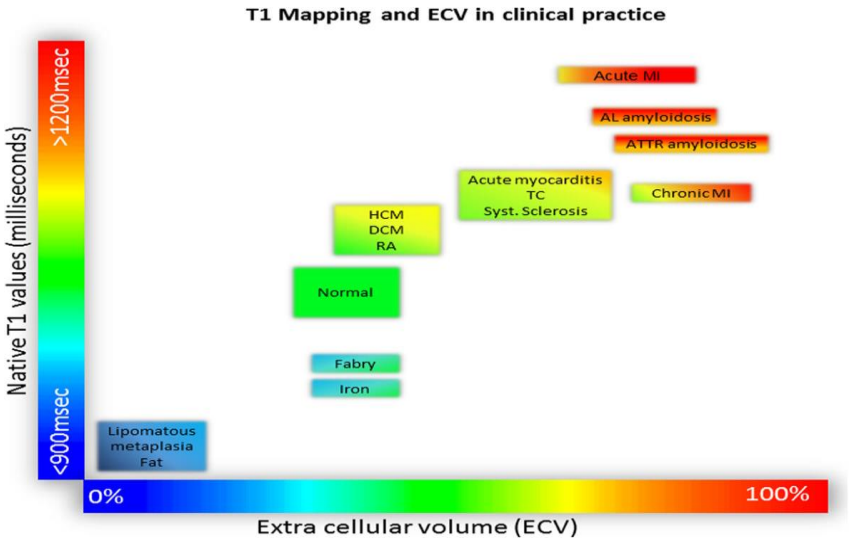

Figure 2.4: Myocardial tissue characterization based on the native T1 and ECV fraction (18).

myocardial infiltration characteristic of different types of non-ischaemic cardiomyopathy.

In summary myocardial T1 mapping is a technique with potential diagnostic and prognostic value for assessment of multiple cardiomyopathies. Compared to LGE, T1 mapping allows for detection of both local and diffuse fibrosis in a non-invasive and contrast-free imaging approach.

Chapter 3 – Myocardial tissue characterization with T1 mapping

3.1 Basic principles of MRI

The primary source of the magnetic resonance imaging signal are the hydrogen atoms, which make up 75% of the human body. The hydrogen atoms have an odd atomic number and they possess an angular momentum $\vec{J}$, called spin. If a group of atoms with a nuclear angular momentum, called spin system, are placed in an external magnetic field B_0, the nuclei will precess around their own axis, generating a magnetic field, called magnetic moment $\vec{\mu}$ (Figure 3.1). The angular and the magnetic momentum are related by the following equation

$$\vec{\mu} = \gamma \vec{J} \qquad [1]$$

where γ is the gyromagnetic ratio. The spins precess at a frequency called Larmor frequency, the natural resonance frequency of a spin system, which is defined by the following equation

$$\omega = \gamma B_0 \qquad [2]$$

However in practice a spin system resonates at a range of resonance frequencies due to system imperfections or magnetic gradient fields, and each group of nuclei that precesses

with the same resonance frequency is called an isochromat. The rotational movement of the spin system is called nuclear precession (20).

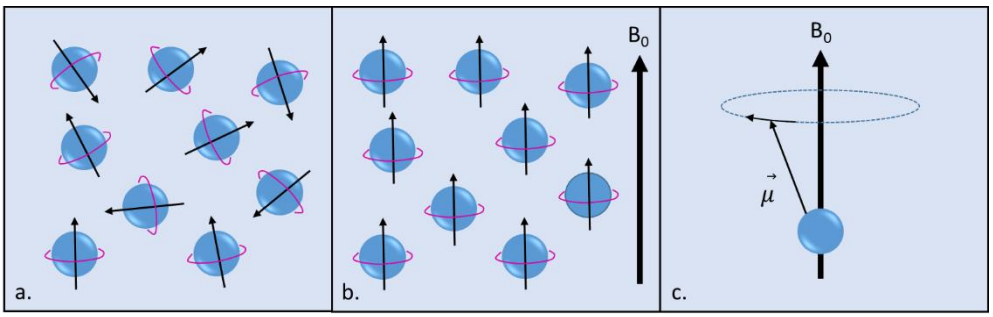

Figure 3.1: a) Spin system of hydrogen atoms; b) The hydrogen spins align to the external magnetic field B_0. c) The nuclear precession of a single hydrogen atom when an external magnetic field B_0 is applied.

By convention, the external magnetic field B_0 is defined as the z direction (z), while the transverse direction is perpendicular to it (xy). At equilibrium, the net magnetization M is aligned along the z axis (M_z), while its transverse component (M_{xy}) is zero.

The spins move away from their equilibrium position when an oscillating external magnetic field B_1, also called radiofrequency (RF) pulse, is applied perpendicular to B_0 and consequently some or all of the magnetization M is tipped to the transverse plane as M mutates about the orientation of the B_1 field. The amount of M_z converted to M_{xy} depends on the RF pulse flip angle, which is a function of the amplitude and duration of the pulse. The longer or stronger B_1 the higher the flip angle, resulting in a larger proportion of M_z converted to M_{xy}. Once the RF pulse has terminated, the spins relax back to the equilibrium by releasing energy to the environment. During the relaxation process the precessing transverse magnetization can be detected with a receiver coil due to the change in magnetic flux (Faraday's Law) (21,22). The relaxation of the spins is controlled by two time constants: the spin-lattice relaxation (T1), which describes the relaxation of the longitudinal magnetization M_z, and the spin-spin relaxation (T2), which describes the decay of the transverse magnetization M_{xy}.

3.2 Contrast imaging

Each pixel of an MR image has an associated signal intensity, which is the magnetic response of the hydrogen nuclei of the corresponding tissue to the static magnetic field and the pulse sequence parameters (23). After perturbation of the magnetization by an RF pulse, the hydrogen nuclei recover back to their initial thermal equilibrium and their behaviour can be described by two main parameters: the longitudinal relaxation time (T1) and the transverse relaxation time (T2). The relaxation times T1 and T2 vary depending on the different molecular environment of the tissues, and this results in a different image contrast, making it possible to distinguish between different tissues.

3.2.1 T1 relaxation time

The relaxation time T1, also called spin-lattice relaxation time, describes the recovery of the spins to their thermal equilibrium position after being perturbed by an external excitation. At thermal equilibrium, the spins are aligned along the z axis, parallel to the static magnetic field B_0. The application of an external excitation RF pulse with amplitude B_1 tips the longitudinal magnetization M_z into the transverse plane. Once the external excitation is switched off, the spins begin to relax back toward their initial equilibrium by transferring energy to the surrounding (lattice), following a recovery model, first described by Felix Bloch:

$$M_z(t) = M_0 - [M_0 - M_0(0)]e^{-\frac{t}{T_1}} \qquad [3]$$

where M_z is the magnetization at time t after the application of an external excitation, M_0 is the magnetization at equilibrium, $M_0(0)$ is the magnetization after the application of the external excitation RF pulse and T1 is the time required for M_z to recover back to the 63% of M_0 (Figure 3.2).

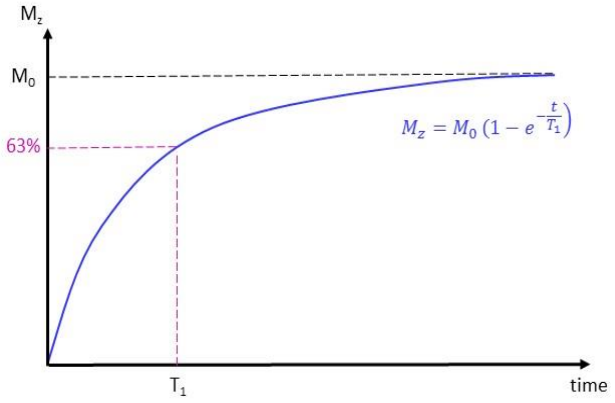

Figure 3.2 Longitudinal relaxation after a saturation pulse modelled by the equation shown in the figure. The T1 is the time at which 63% of the Mz magnetization has been recovered.

The intensity and frequency of the interactions between the excited spins and the lattice depend on the nature and mobility of the molecules in the matter. The molecular tumbling rate, also called correlation time τ_C, is used to characterize the motion of a molecule and is defined as the minimum time for a molecule to rotate one radian (~57˚). When there is a "good" interaction between the molecule and the surrounding tissue, the energy of the spins can be transferred to the lattice, and this occurs as an oscillating magnetic field at or near the Larmor frequency (Figure 3.3). When a molecule tumbles really fast, as the free water, its correlation time τ_C is short and the frequency of the oscillating magnetic field is higher than the Larmor frequency, leading to long T1 relaxation. On the other hand, larger molecules (i.e. fat) as well as bound water, have a lower molecular tumbling rate with a fraction of motion states that match with the Larmor frequency, leading to short T1 relaxation (24,25).

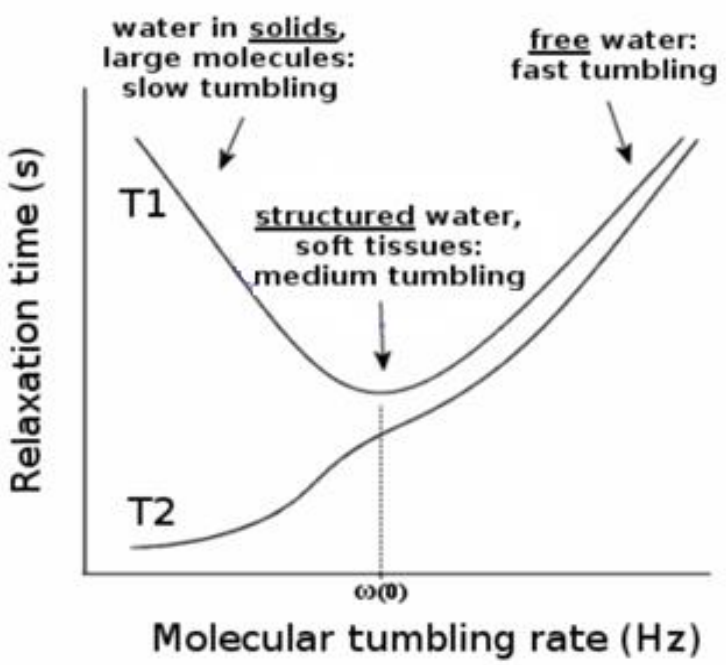

Figure 3.3: T1 and T2 as a function of molecular tumbling rate. At the Larmor frequency the T1 is minimum (25).

With higher magnetic field strength, the Larmor frequency increases and consequently the number of protons (spectral density) available to transfer energy to in the lattice reduces, leading to longer T1 relaxation (Figure 3.4) (22).

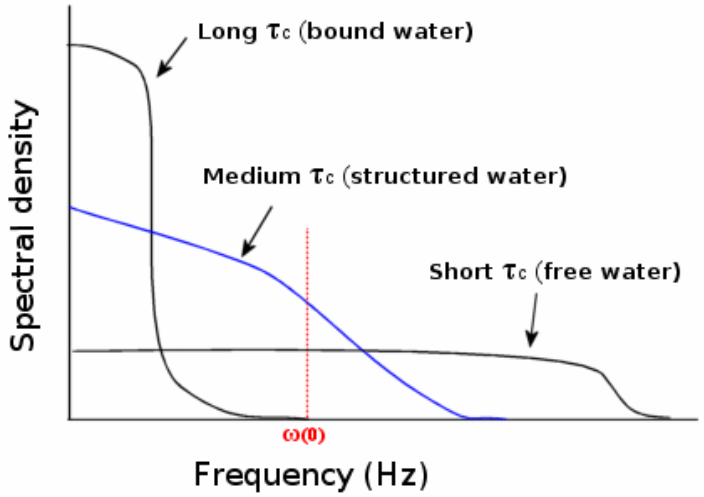

Figure 3.4: Dependency between frequency and spectral density. At higher magnetic field strength, the Larmor frequency increases and the spectral density decreases, leading to a longer T1 relaxation.

3.2.2 T2 relaxation time

The relaxation time T2, called spin-spin relaxation, describes the de-phasing of the spins due to their mutual interaction. The transverse magnetization M_{xy} is generated by applying an excitation pulse. Once the pulse is switched off, M_{xy} starts to decay with a rate described by:

$$M_{xy}(t) = M_{xy}(0)e^{-\frac{t}{T_2}} \qquad [4]$$

where T2 is the time at which the transverse magnetization has reached the 37% of its initial value (Figure 3.5).

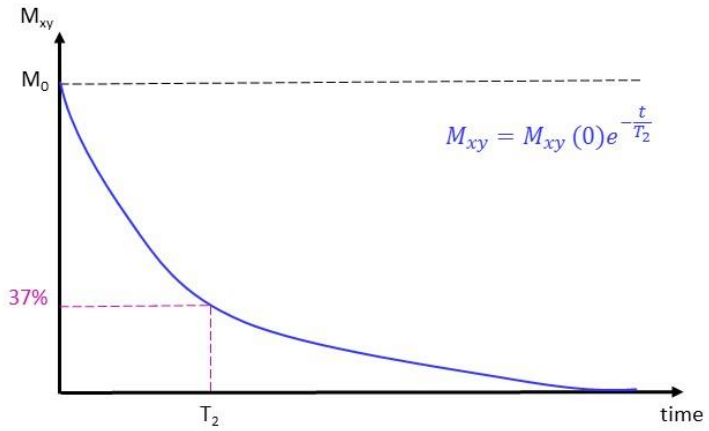

Figure 3.5: T2 relaxation decay modeled by the equation shown in figure. The T2 is the time at which 37% of the transverse magnetization has decayed.

In T2-weighted images, blood and fat signal is usually suppressed in order to improve the image quality and contrast. Consequently a higher contrast is generated between the edema, which has longer T2 value and brighter signal, and the surrounding tissue, with lower T2 values and thus lower signal.

A faster and apparent T2 decay, called T2*, can also occur due to a combination of spin-spin relaxation (T2) and field inhomogeneity (T2') as descried by:

$$\frac{1}{T2^*} = \frac{1}{T2} + \frac{1}{T2'} \qquad [5]$$

Tissues with a higher level of iron deposition have higher T2* value, which is clinically used to assess iron overload in hepatic and myocardial tissue (26).

3.3 Pulse sequences

3.3.1 Spin-echo sequences

The single-echo radiofrequency (RF) spin-echo sequences (SE) consist of an excitation pulse with a flip angle of 90˚ degrees, followed by one refocusing pulse with a flip angle of 180˚ degrees applied after half the echo time (TE) of TE/2, as shown in Figure 3.6, to generate a spin echo at time TE. SE sequences can also include multiple-echoes when more than one refocusing pulse is used. Compared to the gradient-echo (GRE) sequences (which will be described later), SE sequences are more robust to artefacts from off-resonance effects, such as magnetic field inhomogeneity and magnetic susceptibility, due to the 180˚ RF pulse that refocuses the off-resonance effects.

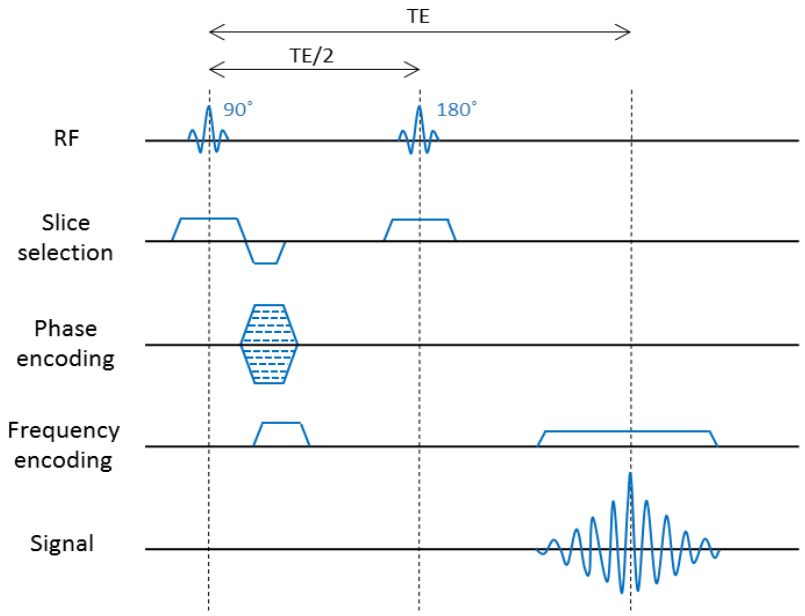

Figure 3.6: Schematic diagram of the single-echo radiofrequency spin-echo sequence (TE = echo time; RF = radiofrequency pulse).

With SE sequences it is possible to obtain images with a specific contrast weighting by adjusting the repetition time (TR) and the echo time values. T1 contrast can be obtained

with short TR and TE, while T2 contrast can be obtained with long TR and TE thus considerably prolonging the scan time or acquisition window. In addition, SE sequences are more sensitive to cardiac and respiratory motion, which limits their use for cardiac imaging, where a shorter TR and acquisition window is usually desirable to minimize cardiac motion.

3.3.2 Gradient-echo sequences

The GRE sequences are better suited for fast scanning and 3D volume imaging than spin-echo sequences, since a shorter TR can be used to minimize motion artefacts. In addition, GRE sequences are less sensitive to flow artefacts compared to spin echo sequences, which collectively makes them more suitable for cardiac imaging. GRE T1-weighted images can be obtained by adjusting the flip angle of the acquisition or by adding an inversion or saturation RF pulses preceding the GRE readout. In contrast to SE sequences, it is not possible to obtain T2 contrast with GRE sequences due to the absence of a refocusing pulse, and thus the contrast depends on T2*. GRE sequences consist of a single RF excitation pulse, which is typically followed by imaging gradients (G_{slice}, G_{phase}, $G_{measurement}$) in all three directions to rephase spins in the slice selection direction, to phase encode the MR signal in the 'phase encoding' direction and to frequency encode the MR signal in the readout or measurement direction by first dephasing the spin isochromats, followed by a rephasing gradient Gr with opposite polarity, as shown in Figure 3.7, to generate a gradient echo signal. The flip angle of the GRE RF pulses can be smaller than 90˚ degrees, which lowers the transmitted RF energy, reducing the patient heating. As a result shorter TR and TE may be used with GRE, thus allowing faster image acquisition compared to SE. As the TR in GRE sequences is usually shorter than the duration of the T2* decay, there may be some transverse magnetization left prior to the next RF excitation which could result in unwanted echo refocusing and associated image artefacts.

Spoiler gradients at the end of the readout gradient are therefore usually used to destroy any remaining transverse magnetization. Another approach is to refocus all magnetization as done in balanced Steady-State Free Precession (bSSFP) gradient-echo sequences, which is an alternative to overcome this problem. By recycling the transverse magnetization with balancing gradients the echo signal becomes higher (leading to higher SNR) and independent of TR making this a very fast sequence. However, if the B_0 field is inhomogeneous gradient balancing can lead to destructive interference, so called

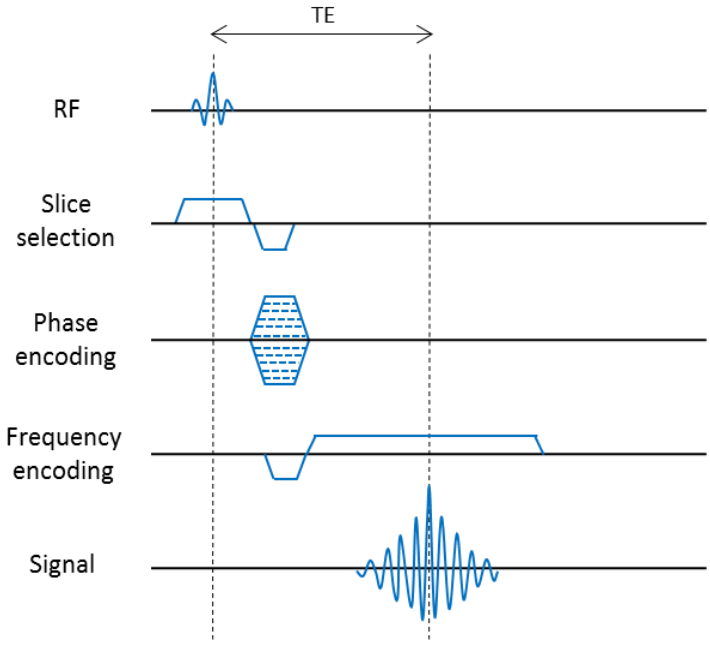

Figure 3.7: Schematic diagram of the gradient-echo sequence.

banding artifacts. As a result, bSSFP is most commonly used on relatively low field strengths (1.5T) where the B_0 is more homogenous, while gradient spoiling is used at higher field strengths 3T where sufficient B_0 homogeneity is harder to achieve.

3.3.3.1 Spoiled gradient echo

For a spoiled gradient-echo sequence, the transverse magnetization should be zero before each excitation. One way to achieve this is to use a long TR, four-five times longer than T2, to ensure that the transverse magnetization is zero before the next RF excitation.

However this solution is impractical since it implies long acquisition times, limiting its clinical applicability. RF and gradient spoiling are instead two different and practical solutions that are used for spoiled gradient-echo sequences. With RF spoiling a phase offset is applied to each successive RF excitation pulse, ensuring that residual magnetization from different excitations will not be in phase. Gradient spoiling refers to the use of very strong spoiler gradients after signal acquisition in order to dephase the remaining transverse magnetization.

3.3.3.2 Balanced steady-state free precession

A bSSFP sequence is characterized by balanced gradients, i.e. the sum of the gradient areas in each of the encoding directions is zero in one TR. Compared to the spoiled gradient-echo sequence, the residual transverse magnetization from one excitation is not destroyed, but is gradient refocused and used in the next TR. Consequently the magnetization will be composed by a mixture and superposition of remaining longitudinal and transversal magnetization. After a certain number of repetition times, the magnetization will reach a so-called steady-state for free-running bSSFP sequences and this steady-state will be maintained nearly constant for the rest of the acquisition, in the absence of flow and motion (27). In cardiac imaging, where synchronization with the electrocardiogram (ECG) may be required, it is necessary to wait few repetition times in order to reach a pseudo steady-state, during which the signal does not oscillate anymore and thus do not cause artefacts. Usually, few startup echoes without data sampling are performed before the image acquisition in order to limit this problem. The steady-state signal for bSSFP is influenced by the flip angle of the RF pulse and is proportional to the ratio T2/T1. The stop bands are influenced by TR and are centered around TR/2. The bSSFP sequence permits to achieve high SNR and good intrinsic blood-myocardium

contrast independent of the TR, which makes it an ideal sequence for fast imaging and cardiovascular applications.

3.4 Magnetization preparation for T1 mapping

Quantitative T1 mapping relies on the spin-lattice relaxation phenomena. In order to generate a T1 map, the characteristic relaxation recovery curve (Figure 3.2) is sampled at different time points, where each point corresponds to an image with a specific T1 contrast. An exponential model is then used to fit the points along the curve and to generate a final T1 map using a pixel-wise fitting approach. Each pixel of the T1 map represents the T1 value of the corresponding tissue in the image.

There are two main magnetization preparation approaches that can be used to generate the T1 contrast, the inversion-recovery and the saturation-recovery based imaging techniques. Recently T1 mapping imaging techniques have been proposed, which instead use a combination of both inversion and saturation recovery pulses (7).

3.4.1 Inversion recovery

An inversion-recovery based technique applies an 180˚ RF pulse to excite and perturb the longitudinal magnetization M_z. T1-weighted images are then acquired at different time points, called inversion time (TI), along the recovery-curve. The first inversion-recovery based T1 mapping technique was proposed in 1980 by Look and Locker, called the Look-Locker (LL) technique (28). With this technique, an inversion recovery pulse is applied and data are acquired repeatedly to create multiple images along the T1 recovery curve. The next inversion recovery pulse is applied after 5*T1 of the longest expected T1 species, in order to allow a full recovery of the magnetization. The technique was successfully applied to neurological studies but not yet for cardiac imaging, since the T1-

weighted images were acquired continuously without taking into account any cardiac motion. Initial attempts to enable myocardial T1 mapping using LL technique involved synchronization with the ECG signal to ensure that a specific T1 was acquired at the same cardiac phase, minimising cardiac motion for each T1 (29). However, in this approach the inversion time images were acquired at different cardiac phases, leading to motion between images, precluding pixel-wise T1 quantification. Although this technique is not suitable for pixel-wise T1 mapping, since each TI is acquired at a different cardiac phase, it is commonly used auxiliary to LGE imaging in order to find the optimal inversion time to null the signal from the myocardium.

MOLLI (5) technique was proposed as an extension of LL technique for cardiac applications to allow both for pre- and post-contrast T1 mapping. Compared to the original LL technique, data are acquired at a specific time during the cardiac cycle along the different heartbeats, and the acquisition window is set to coincide with mid-diastole with a duration of maximum 200 ms. This effectively minimizes cardiac motion between subsequent T1-weighted images and enables pixel-wise T1 estimation. Secondly, successive LL experiments are performed with different TIs and the data of each different experiment are then merged together to form a unique data set. The latest principle allows to increase the number of samples along the relaxation curve compared to LL, which results in improved precision of the T1 measurements. The original MOLLI pulse sequence consists of three successive LL experiments, respectively with three, three and five readouts (3-(3)-3-(3)-5), with a pause of three heartbeats between each LL experiment to allow for T1 recovery. Figure 3.8 shows a schematic diagram of the acquisition and fitting of the MOLLI technique.

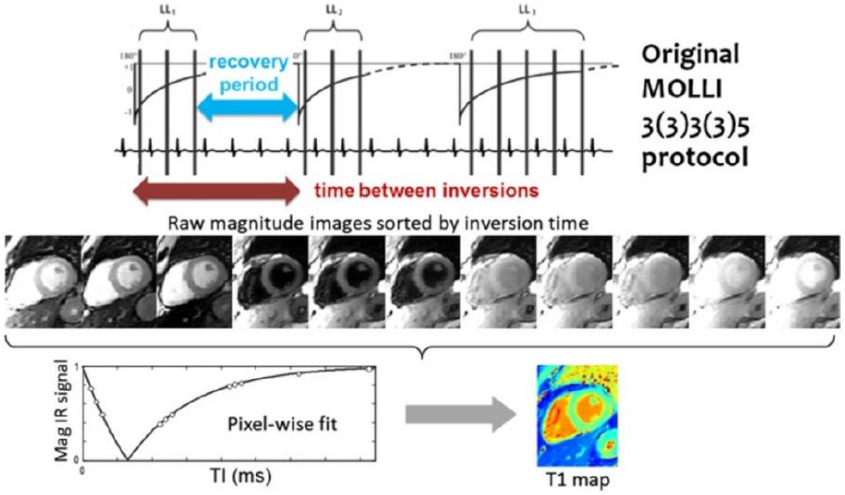

Figure 3.8: Schematic diagram of the original 3-3-5 MOLLI protocol and the corresponding acquired T1-weighted images. The images are then sorted by the inversion time and a pixel-wise fitting approach is used to obtain the T1 map (16).

The first image of each LL experiment is acquired at TI time after a non-slice selective adiabatic 180° pulse and a delay time (TD) after the R-wave. Subsequent images are then acquired in each heart beat after the time TD after the R-wave. The acquired T1-weighted images are then fitted pixel-by-pixel to the following signal model:

$$S(t) = A - Be^{-\frac{t}{T_1^*}} \qquad [6]$$

where A is a scaling factor of the signal intensity, B represents the quality of the inversion pulse, and $T1^*$ is the apparent longitudinal relaxation time. The bSSFP readout allows the inversion recovery curve to be closer to the theoretical recovery curve compared to a spoiled gradient echo readout as less of the longitudinal magnetization is being utilised (30). In addition MOLLI is highly heart rate dependent, and this is due to the time between the inversions and the influence of the bSSFP readouts. MOLLI is also T2 and magnetization transfer (MT) dependent, which lead to an error in the T1 estimation. These are all factors that affect the accuracy of the T1 measurements. Consequently a correction is needed to obtain less biased T1 values:

$$T1 = T1^{*}\left(\frac{B}{A} - 1\right) \qquad [7]$$

Another limitation of MOLLI is the long breath-hold (17 heartbeats) required to acquire a 2D single slice image. A different sampling scheme of MOLLI (5-(3)-3) has been proposed as an alternative solution to the long breath-hold as well as the heart rate sensitivity, which permits to reduce the total number of heartbeats to 11.

Other solutions have been proposed called Shortened MOLLI (ShMOLLI) (31), which uses a 5-(1)-1-(1)-1 acquisition scheme and allows for a 9 heartbeats breath-hold. To allow the magnetization to have enough time to completely recover between the successive LL experiments, a new concept of conditional data analysis is used, with which the short and long T1 are differentiated and evaluated with a different number of samples. For long T1 only the first five images are used, and this allows to lessen the heart rate effect. The T1 maps generated with ShMOLLI and MOLLI do not present significant differences, but the duration of the single breath-hold is considerably reduced to 9 heartbeats compared to the 17 needed with MOLLI. In this way image artefacts due to respiratory motion are limited and the dependency to heart rate variability is reduced, thus increasing the final accuracy.

3.4.2 Saturation recovery

The T1 contrast can also be obtained by using a saturation-recovery based technique, where instead a 90˚ degree pulse is applied to perturb the longitudinal magnetization. A 2D imaging technique, called SASHA (6), has been proposed that acquires a 2D single slice in a breath-hold. Images at different time points, called saturation times (TS), are acquired along the T1 recovery curve and fitted to the following signal model to obtain a parametric T1 map:

$$S(t) = A - B\,exp\left(-\frac{t}{T1}\right) \qquad [8]$$

where A is a scaling factor of the signal intensity, B takes into account the saturation efficiency and T1 is the longitudinal relaxation time.

Figure 3.9 illustrates the acquisition scheme proposed for the 2D SASHA imaging sequence. First an image without any magnetization preparation is acquired, as a measurement of the fully recovered M_z magnetization, and successively ten images are acquired at different TS. Compared to an inversion-recovery pulse, a 90° RF saturation pulse (with associated spoiler gradients) permits to completely erase the history of the longitudinal magnetization, thus eliminating any dependency between the different acquisitions. This implies that there is no need for a recovery time between the acquisitions and there is no need to apply any additional correction to T1. A saturation-recovery based imaging sequence is also less sensitive to the heart rate variability, which makes the technique better suitable for a 3D extension and it is also less sensitive to T2 and MT than MOLLI.

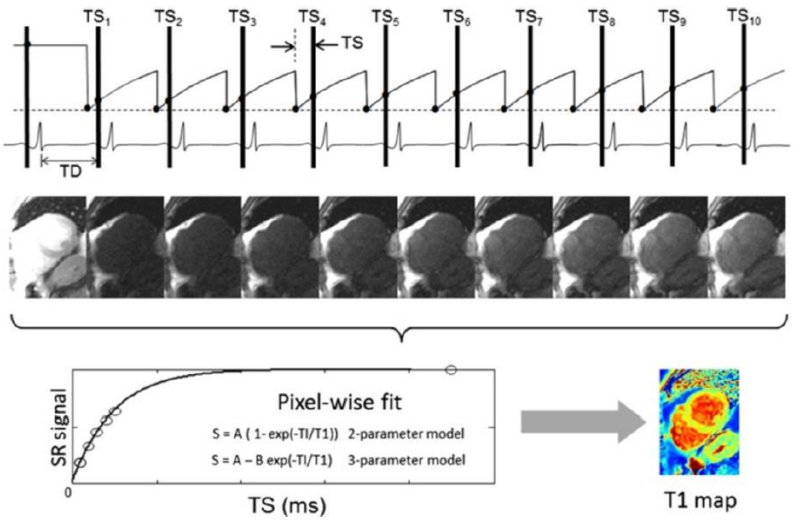

Figure 3.9: Schematic diagram of the 2D SASHA imaging sequence. The T1-weighted images are acquired at different saturation timed TS and then are fitted along he T1 recovery curve, to obtain a final T1 map (16).

A different solution has been also proposed, which combines the inversion-recovery and the saturation-recovery pulses for myocardial T1 mapping, called saturation pulse prepared heart rate independent inversion recovery (SAPPHIRE) pulse sequence (7). Figure 3.10 shows a schematic diagram of the SAPPHIRE acquisition. First an image without any magnetization preparation is acquired. Successively a saturation pulse is applied after the R-wave of each heartbeat to erase the history of the magnetization, followed by an inversion-recovery pulse at the time TS-TI. A total of nine images are acquired consecutively, where for each image the TI changes in order to generate different T1 contrast.

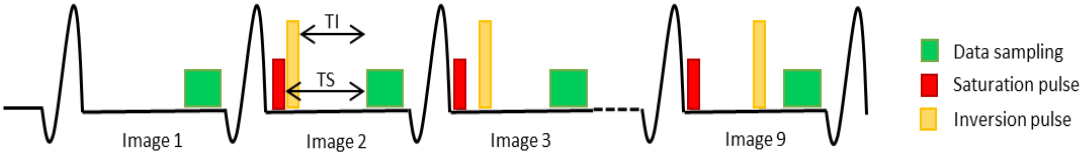

Figure 3.10: Schematic diagram of the SAPPHIRE imaging sequence. The first image is acquired without any magnetization preparation, followed by the acquisition of eight images by applying a saturation pulse at the saturation time TS and a variable inversion time TI. (Adapted from *(7)*)

SAPPHIRE was proposed in order to combine the advantages of MOLLI and SASHA. The inversion recovery pulse permits to increase the dynamic range, which improves the precision of the T1 maps; the saturation-recovery pulse, instead, erases the history of the magnetization thus eliminating the need of a rest period and consequently decreasing the duration of the breath-hold. In addition, SAPPHIRE proposes a solution for the heart rate dependency of MOLLI.

3.5 Fitting model

Once the T1-weighted images are acquired at different inversion or saturation times, a mathematical model of the longitudinal magnetization is required to enable T1 estimation.

One approach is to use a multi-parameter curve fitting analysis, where the images are fitted pixel-by-pixel along a model describing the T1 relaxation curve. The model can contain different numbers of unknowns (T1, equilibrium M_z, etc.), which are estimated after an iterative pixel-wise fitting approach. Incorporating additional parameters into the model reduces systematic errors (accuracy), while increasing the sensitivity to noise (precision), and there is often a trade-off between accuracy and precision in T1 mapping. In the original implementation of the MOLLI sequence, T1-weighted images are acquired at different inversion times using a bSSFP readout and a three parameter model is used to estimate the parameters (5). The fitting model used to describe the T1 recovery and the correction for T1 is shown in Equation 6 and 7. To generate a MOLLI T1 map in a clinically feasible scan time multiple images are acquired per inversion pulse, leading to systematic underestimation of T1 as the readouts also perturb the M_z magnetization. In addition the T1 estimation is also affected by T2 and MT sensitivity of MOLLI. These are the reasons why it is necessary to correct the measured T1* in order to obtain the real T1 measurement.

A saturation recovery based T1 mapping techniques acquires T1-weighted images at different saturation times. Compared to the inversion-recovery method, the saturation-recovery technique only acquires one image per saturation pulse and therefore measures the true T1 recovery. A two- or three-parameter fitting model is usually used, respectively:

$$S(t) = A\,(1 - \exp(-t/T1)) \qquad [9]$$

$$S(t) = A - B\,\exp(-t/T1) \qquad [10]$$

The two-parameter signal model (equation 9) permits to achieve more precise estimations. However, it does not take into account the imperfections related to the saturation recovery pulse and it leads to T2 and MT sensitivity. In contrast, the parameter

B of the three-parameter signal model (equation 10) takes into account the saturation efficiency of the saturation-recovery pulse, thus the fitting allows to get a more accurate T1 map. However, there is a loss in precision due to cost required to estimate the additional parameter.

Dictionary based fitting is an alternative approach that has been recently proposed to obtain simultaneous measurements of different parameters, such as T1, T2, proton density (PD), B_0 inhomogeneity (32). Either one of the above described T1 mapping methods is used or a single acquisition such as in MR fingerprinting, where the acquisition parameters are varied in a pseudorandom fashion, such that each tissue generates a unique signal evolution. A dictionary is then built, with its entries being signal evolutions of M_z with different combinations of the parameters of interest (T1, T2, PD, etc.) derived from the Bloch equations or the extended phase graph formalism (33). The signal evolution of the acquired images are then compared with all the entries of the dictionary using a pattern recognition algorithm, in order to find the signal from the dictionary that best corresponds to the observed signal evolution (34). This permits to automatically assign to each voxel the parameters that were used to simulate the resulting best match. There are different type of pattern recognition algorithms that can be used for this purpose, such as the dot product and the least square method. The dictionary needs to contain a wide range of combinations of the parameters to be estimated in order to be highly accurate and to guarantee a correct estimation of the tissue parameters, which may require long computation times for the recognition algorithm to find the best match.

3.6 Accuracy, precision and reproducibility for T1 mapping

A myocardial T1 mapping technique is effective when it achieves high accuracy, precision and reproducibility of the T1 measurements (9). Accuracy and precision are

usually validated on a T1 phantom with known T1 and T2 values. Accuracy is the difference between measured and true value, while the precision is evaluated in terms of variability between the different measurements and it is inversely proportional to the standard deviation. The reproducibility is the capability of a technique to provide the same results between different experiments, independently of the subjects and machine, which would make the technique more clinically reliable.

Both accuracy and precision can be affected by different factors: the choice of the sequence parameters, the scanner used for imaging, the fitting model, motion artefacts, partial volume effect, tissue characteristics and patient factors, such as heart rate and respiratory motion (16). The reproducibility relates to the dependency of the technique to heart rate, T2 or other aspects, which can alter the final T1 estimation.

SASHA and SAPPHIRE are more accurate than MOLLI and ShMOLLI, since they are less dependent to heart rate and sequence parameters such as flip angle or TR. However the variability in T1 maps is greater compared to MOLLI and ShMOLLI, which means that the precision is reduced. The precision of SASHA, however, can change depending on the fitting model used (6). In fact a three-parameter fitting model permits to reconstruct more accurate 3D SASHA T1 map, which is noisier due to the additional parameter that has to be estimated. On the other hand, a two-parameter model reduces random errors and thus improves the final precision. However, it does not take into account the imperfect saturation and it leads to T2 and MT sensitivity, which affects the final accuracy (16).

In terms of reproducibility, no significant differences have been found and all the techniques have shown similar level of reproducibility (9).

Chapter 4 – Motion compensation and correction for T1 mapping

4.1 3D T1 mapping: speed as a challenge

Most of the clinically used T1 mapping techniques acquire a series of T1-weighted 2D images in one single breath-hold. To minimize scan time, often only three short axis slices (base, mid, apical) are acquired in T1 mapping. However, the myocardial T1 measured in these three slices does not necessarily characterize the entire ventricle. In addition, as myocardial fibrosis can be localized or diffuse, this approach may underestimate the true burden of fibrosis. To address this problem, a free-breathing navigator gated slice-interleaved T1 sequence, called STONE (35), has been proposed, which allows to acquire five interleaved slices after one initial inversion pulse. More specifically, after each inversion pulse, slices 1 to 5 are spread over five heartbeats whereby the inversion time is TI + n*RR-interval, with n being the current heartbeat after inversion. This is then repeated five times with the order of the slices interchanged every time so that for each slice all possible inversion times have been acquired. As the STONE sequence only samples one point along the T1 recovery curve after each inversion pulse per slice, no T1 correction is required and thus STONE is more accurate than MOLLI and results in longer

myocardial T1 values in vivo. However, the longitudinal magnetization may be disturbed by the imperfect slice profile of the imaging sequence and residual cardiac and respiratory motion.

Although the STONE technique improves myocardial coverage, spatial resolution is still limited (in plane resolution = 2.1 mm and slice thickness = 8 mm) and coverage not complete. Therefore a 3D imaging technique with true 3D volumetric coverage of the heart, higher image resolution and SNR than that achievable today with 2D imaging technique would be desirable. With 3D imaging, slices can be reconstructed consecutively, without the need to leave any slice gap. In addition, a 3D acquisition would also permit to reformat the images in arbitrary imaging planes. A post-contrast 3D T1 mapping technique has been already proposed, which allows for free-breathing 3D volumetric assessment of myocardial fibrosis (36). However, pre-contrast T1 mapping is more challenging, since pause cycles are needed for a full recovery of the magnetization, the SNR is lower due to the longer T1 pre-contrast, and respiratory motion estimation more difficult to estimate correctly.

There are some aspects that need to be taken into account in order to perform a 3D T1 mapping acquisition. The duration of a high-resolution 3D acquisition is longer than a 2D single slice acquisition, and consequently a variable heart rate can severely affect the magnetization recovery and quality of the acquired images. In addition, due to the extended scan time associated with a high-resolution 3D image acquisition of the heart, it is necessary to acquire data in free-breathing and consequently a respiratory motion compensation technique is mandatory. The SASHA T1 mapping technique is a promising approach for the implementation of a volumetric free-breathing T1 mapping technique of the whole heart. This is due to the use of the saturation recovery pulses for the magnetization preparation, which makes SASHA less dependent on a stable heart rate

compared to MOLLI. In addition, the saturation pulse permits to completely erase the history of the magnetization, which implies that no resting periods are required to wait for full M_z recovery, improving the scan efficiency.

4.2 Cardiac motion compensation and correction

In CMR it is necessary to synchronize image acquisition with the cardiac cycle in order to limit cardiac motion and improve image quality. The cardiac cycle consists of two periods: systole, when the heart contracts and pumps the blood out of the ventricles; and diastole, when the heart relaxes and refills with blood. An ECG is used to measure the electrical activity of the heart and to identify at which cardiac phase the images are acquired. This technique is called ECG-triggering and can be performed both prospectively and retrospectively (Figure 4.1).

With prospective ECG-triggering, images are acquired during a specific cardiac phase after a user defined trigger delay between the R wave of the ECG and the center of k-space. The data acquisition usually lasts for 100-150 ms, called acquisition window, which is typically in mid-diastole and coincides with the quiescent phase in the cardiac cycle. The retrospective acquisition permits to acquire the data continuously during the cardiac cycle. A fixed number of cardiac phases are then defined and data are assigned to a specific cardiac phase using interpolation algorithms.

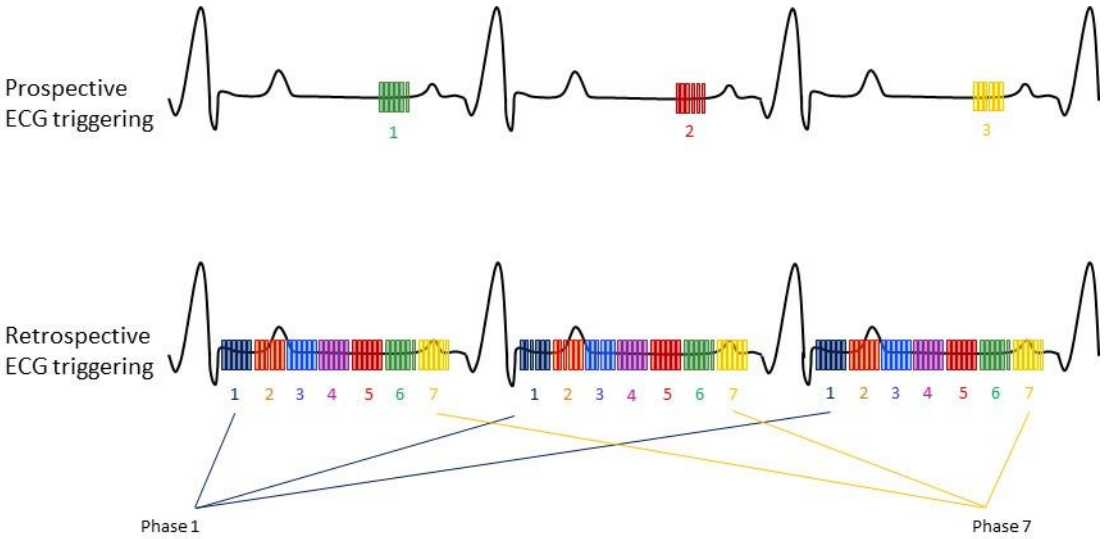

Figure 4.1: Schematic diagram for the prospective and retrospective ECG triggered and gated acquisitions. With the prospective ECG gating, the images are acquired during a specific cardiac phase (end-diastole). With the retrospective ECG gating, the data are acquired continuously during the cardiac cycle. Successively, the data are reordered and assigned to a specific cardiac phase.

The ECG-synchronized acquisition can be a single-shot or a segmented acquisition. With a single-shot acquisition the image (single phase) or images (multi-phase) is acquired in a single cardiac cycle in real-time. This technique allows fast data acquisition and is more robust to ECG and breath-hold variability. However, it is limited by low spatial and temporal resolution. With the segmented acquisition a fixed number of segments (k-space lines) are acquired in each heartbeat spread over several consecutive heartbeats and then collated to reconstruct the image. Consequently, using this approach it is possible to reduce the length of the acquisition window, thus increasing the spatial and temporal resolution. On the other hand, this approach is more sensitive to breath-hold and heart rate variability, as data are acquired over a longer period.

4.3 Respiratory motion compensation

Another type of motion that needs to be considered in CMR is the respiratory motion. Respiratory motion introduces artefacts that can severely deteriorate image quality,

potentially leading to wrong clinical interpretation and diagnosis. The simplest approach to deal with respiratory motion is to acquire images during a breath-hold. This is not always possible due to compromised breath holding capabilities in many patients. In addition, breath holding limits the achievable spatial resolution. Alternatively, different solutions of respiratory motion compensation have been proposed in order to allow for a free-breathing acquisition. An external device such as the respiratory bellow could be used for external respiratory monitoring (37). This technique provides high temporal resolution and is independent of the MR acquisition, so it can be acquired separately without affecting the steady-state of the magnetization. However, the information provided by this technique is not quantitative, and only informs about the timing of inspiration and expiration but not its amplitude. Hence additional information is necessary to compensate for more complex motion (e.g. affine or non-rigid) of the heart.

4.3.1 Respiratory navigators

An alternative solution for respiratory motion detection and correction are the respiratory navigators. Respiratory navigators are integrated within the MR acquisition and allow estimating the motion of the heart and surrounding tissues. There are different implementations of respiratory navigators: 1) diaphragmatic navigator, 2) self-navigation and 3) image-based navigator (38).

Diaphragmatic navigator

A diaphragmatic navigator is a 1D signal (1D dNAV) acquired perpendicular to the diaphragm, which estimates the foot-head (FH) motion of the lung-liver interface (Figure 4.2) (38). It is acquired immediately prior to image acquisition, in order to reduce the temporal distance between the motion estimation and the actual acquisition. It has been widely used in cardiac MR, since it can be easily combined with different cardiovascular imaging sequences and it is relatively easy to use.

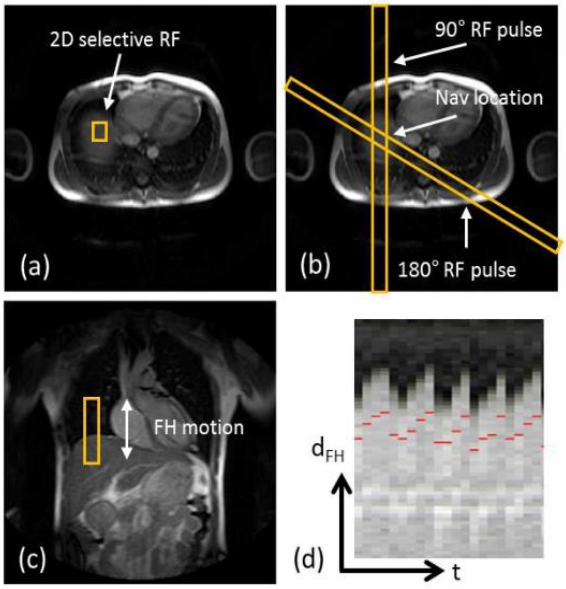

Figure 4.2: a-c) Planning of the 1D NAV at the scanner. d) Visualization of the 1D signals coming from the lung-liver interface. Adapted from (38).

The 1D dNAV is usually combined with a respiratory gating strategy, called accept-reject algorithm (ARA) (41), in order to reduce the amount of respiratory motion to correct for. With the ARA algorithm, a gating window of usually 5 mm is placed in end-expiration and only data acquired inside this gating window are accepted. A standard scaling factor of 0.6 is used to relate the FH displacement of the lung-liver interface to the heart motion (42). This approach has been effectively used in different cardiac studies (43), however it has several drawbacks. First of all, the scan time is unpredictable: with a gating window of 5 mm, the navigator efficiency can be between 25-50%, and it can easily further drop in patients with irregular breathing patterns. From the 1D dNAV only the FH motion can be estimated, allowing only translational FH motion correction. In addition, respiratory motion is usually estimated from the motion of the lung-liver interface (diaphragm) and consequently a motion model is required to translate diaphragmatic motion to cardiac motion which then can be applied as a phase shift in k-space to each shot to correct for FH motion.

Self-navigation

In order to overcome some of the limitations of the 1D dNAV, a different approach has been proposed, called self-navigation (44). With self-navigation the central line of k-space is acquired repetitively (40), preceding each k-space segment and aligned with the FH direction. From this line, which is a projection image of the excited 3D volume, the respiratory motion of the heart is estimated directly in FH direction. Compared to the 1D dNAV, there is no need to use a standard scaling factor to relate the diaphragmatic and respiratory cardiac motion, since self-navigation allows for direct measurement of cardiac motion. However, since the line is a projection of the entire field of view (FOV), it also includes information from the surrounding static tissues, which can affect the performance of the self-navigator. In addition, to obtain a reliable signal from the centre of k-space line, typically a principal component analysis (PCA) of the signal from all coil elements is performed to obtain the respiratory signal. As the PCA signal is unit less, the signal cannot be used for respiratory motion correction but only for data gating or binning. In this case, self-navigation will leave intra-bin motion uncorrected.

Image-based navigator

With the image-based navigator a 2D or 3D low resolution image is acquired in each heartbeat prior to the main imaging sequence (45–47). Compared to self-navigation, the advantage is that it is possible to separate the motion of the heart from the motion of the surrounding static tissues. This permits to apply more advanced motion corrections algorithms including 2D or 3D translational, affine or non-rigid rather than a simple translational FH correction available that 1D dNAV or 1D self-navigation provides. One limitation of this approach is that the acquisition of the image-based navigator could affect the signal or cause artefacts in the subsequent image acquisition. To overcome this problem, if a bSSFP is used, the image navigator can be implemented by encoding the start-up echoes used to drive the magnetization into the steady state thereby not or only

minimally affecting image quality (48). A particular challenge in T1 mapping is that the contrast of the image navigators depends on the saturation or inversion time, which may be suboptimal for time points close to the zero crossing of the blood magnetization. An alternative approach to address this problem is to use the epicardial fat signal to estimate the respiratory motion of the heart (49,50). This fat-iNAV, which only excites the fat protons, does not affect the water signal, and for this reason it could be effectively used in combination with myocardial T1 mapping. An application of this fat-iNAV for myocardial T1 mapping will be presented in Chapter 9.

4.4 Respiratory translational motion correction

With CMR it is possible to correct for the respiratory motion both prospectively and retrospectively. Prospective motion correction permits to update and correct the k-space before each image acquisition, while the retrospective motion correction is done as a post-processing step.

Translational motion correction allows to correct for 2D motion, e.g. in FH and right-left (RL) direction, and it can be performed both prospectively and retrospectively. 2D translational motion is estimated by selecting a region of interest (ROI) around the heart in the iNAVs. An iNAV is chosen as reference frame, typically at end-expiration, and then translational motion can be estimated between the reference and any subsequent iNAV using image registration with a certain similarity measure, e.g. normalized cross-correlation or sum of squared distance.

Translational motion Δa_x in the image domain in the encoding direction x causes a phase shift θ_x defined by:

$$\theta_x = \frac{2\pi \Delta a_x}{FOV_x} \qquad [11]$$

which is inversely proportional to the FOV_x of the image.

With the retrospective translational motion correction, the phase shift is applied in the k-space domain as follows

$$k_j' = k_j e^{i\theta_x j} \qquad [12]$$

where $k_j$is the raw data sampled at index j of the k-space with encoding direction x and k_j' is the motion corrected raw data.

Translational motion correction is the simplest approach to use in CMR, however an affine model may be more adequate to describe the motion of the heart, since it takes into account not only translation but also rotation, sharing and scaling.

Alternatively a more complex, non-rigid motion correction of the heart can also be used. With this approach a 3D non-rigid motion is estimated from the data itself. Using a 1D self-gating signal or image navigators, which are acquired on a beat-to-beat basis, the acquired data are then grouped in different positions along the respiratory cycle, called respiratory bins. Subsequently, data in each bin can be aligned with the centre of the bin using the respiratory motion curves derived from 1D self-gating or image navigators, which is referred to as intra-bin translational motion correction. These bins, which contain undersampled k-spaces, are then reconstructed using iterative SENSE (51), compressed sensing or low rank reconstruction, with SENSE being explained in chapter 5. In a second step, 3D non-rigid deformation fields can be estimated in a bin-to-bin fashion through image registration using the end-expiration bin as reference. The non-rigid motion fields obtained from this bin-to-bin registration can then be used in a general matrix description motion corrected reconstruction (52,53) to obtain motion corrected high-resolution 3D datasets. This approach permits to correct for more complex respiratory motion estimation and correction of the heart due to the increased spatial information provided at each bin. However, it can be challenging particularly for myocardial T1 mapping, since it could affect the T1 quantification.

Chapter 5 – Post-processing

5.1 MR reconstruction

The MR signal is acquired in the k-space domain, and is transformed in the image domain through a process called image reconstruction.

The simplest approach is to reconstruct an image from a fully-sampled Cartesian sampling acquisition. If we consider the discrete linear problem:

$$S = Ex \qquad [13]$$

where S is the vector of sampled k-space data, E is the encoding matrix containing the coil sensitivities, Fourier transform (FFT) and k-space sampling, and x the vector of the unknown parameters, then the image reconstruction consists in the direct inversion of the encoding matrix. If the data are not sampled using a Cartesian trajectory (e.g. radial or spiral samplings (54,55)), the acquired data has to be resampled on a rectilinear grid, followed by an FFT. This process is often referred as gridding reconstruction.

Most MR acquisitions are nowadays accelerated and only a small portion of the k-space data is acquired. When the MR acquisition is accelerated, the Nyquist criteria is violated, consequently a simple FFT is not enough to recover the image and, hence, additional *a*

priori information need to be added into the reconstruction process in order to recover the original image.

One way to overcome the prohibitively long scan times of 3D acquisition is through undersampled image acquisitions, and subsequent parallel imaging or compressed sensing image reconstruction.

Parallel imaging is a widely used technique that allows to accelerate the acquisition, in the order of 2-3 in one phase encoding direction by 2-3x undersampling k-space of each individual image and exploiting the information provided by multi-array coils, yet at a SNR penalty that is proportional to the local coil geometry. Sensitivity encoding (SENSE) (56) and generalized autocalibrating partially parallel (GRAPPA) (57) are the two main parallel imaging techniques: with SENSE the images are reconstructed in the image domain, while with GRAPPA the reconstruction occurs in the k-space domain. In this thesis, I only focus on SENSE reconstruction for Cartesian sampling.

5.1.2 SENSE reconstruction

SENSE reconstruction permits to accelerate the acquisition by increasing the space between the sampling positions in the phase-encoding direction of the k-space by an acceleration factor R. The FOV of the images consequently reduces and this causes aliasing artefacts in the reconstructed images. In order to recover the full FOV images, the information from the multi-array coils are used to separate the superimposition of the signals. In fact each pixel has a different weight according to the local coil sensitivities (C) at that specific location. If we consider an image acquired with an acceleration factor of R=2, using two coils, C_1 and C_2, the signal of the aliased pixel at the position (x, y) can then be expressed by the following equations, which are visually shown in Figure 5.1:

$$S_1(x,y) = C_1(x,y)\rho(x,y) + C_1\left(x, y + \frac{FOV}{2}\right)\rho\left(x, y + \frac{FOV}{2}\right) \quad [14]$$

$$S_2(x,y) = C_2(x,y)\rho(x,y) + C_2\left(x, y + \frac{FOV}{2}\right)\rho\left(x, y + \frac{FOV}{2}\right)$$

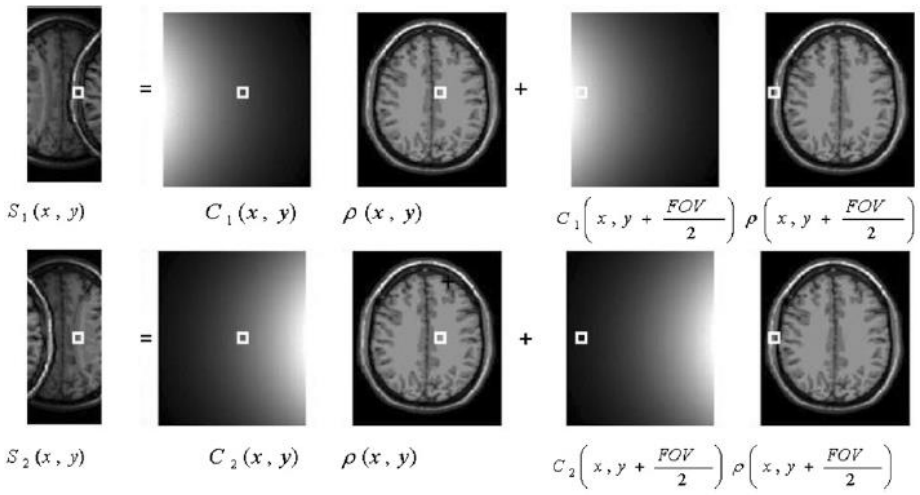

Figure 5.1: Illustration of SENSE principles, which are described in equations [14]. Adapted from (98).

The only requirement in order to solve the equations below and to recover the unfolded image is to have at least the same number of coils as the acceleration factor used.

The limitation of the SENSE reconstruction is the loss of SNR in the reconstructed image with reduced phase-encoding (SNR^{acc}) compared to the SNR in the image with full-encoding (SNR^{full}), which can be defined as:

$$SNR^{acc} = \frac{SNR^{full}}{g\sqrt{R}} \quad [15]$$

The loss of SNR is then proportional to the square root of the acceleration factor R and the geometry factor g, also called *g-factor*, which depends on the geometry of the coils.

5.2 Denoising regularization techniques

In multiple scenarios, the acquired samples are generally corrupted by noise, making the reconstruction problem more complex. The reconstruction problem can be rewritten as

$$S = Ex + \varepsilon \qquad [16]$$

where ε denotes the noise (generally unknown).

Noise is an inherent component of MRI that could severely perturb the accuracy and precision of the images acquired and, therefore, compromise the diagnostic value of multi-parametric images. In myocardial T1 mapping, noise can be related to the choice of the acquisition parameters and the fitting model used. Denoising algorithms could be used in order to reduce the level of noise in the images *x*, leading to improved precision in quantification. Different regularization techniques can be applied as a post-processing step for denoising leading to improved precision in quantification. Tikhonov regularization (58) has been widely used in different MR scenarios to provide noise free images. In 1992, Rudin, Osher and Fatemi (59) introduced total variation regularization (TV) for real-world image denoising. TV exploits the edge information in the image to allow high-denoising quality while preserving edges information and sharpness. A modification of TV has also been proposed, referred as Beltrami (60), which exhibits the same good properties of TV (high denoising quality and sharpness), but improves the denoising quality on flat areas (e.g. blood pool, white matters).

In this study a new 3D denoising post-processing approach, which extends the Beltrami regularization, is presented, originally proposed for 2D denoising of real-world images, to multi-contrast 3D MR acquisitions (11,61). The proposed technique is applied to 3D myocardial T1 mapping to recover T1 maps with high quality and improved diagnostic value.

Considering a dataset S of n real-valued images i={1,…,n} obtained after MR reconstruction, the denoising problem aims at finding the images p free of noise ε, given the measurements S, defined as $S = p + \varepsilon$. This is an ill-posed problem which can be solved with a least-square optimization frame-by-frame:

$$\widehat{p_i} = \min_{p_i}\{\|p_i - S_i\|_2^2 + \lambda R(p_i)\} \quad [17]$$

where R is the Beltrami regularization function, while λ is the nonnegative regularization parameter that imposes the degree of closeness of the prior knowledge (p_i) to the data. Thus, $\widehat{p_i}$ is obtained by solving the minimization problem in equation [17]. With the Tikhonov regularization method, the regularization function is defined as $\|p_i\|_2^2$, while for the TV approach the regularization term is defined as $\|\nabla p_i\|_1$, where ∇ is the multi-dimensional gradient (i.e. here the gradient of the images is constrained) and $\|\quad\|_n$ is the ln-norm. The Tikhonov regularization permits to obtain a smooth solution, while the TV permits to preserve the edges of the image. On the other, hand the limitation of the TV approach is that it introduces staircasing artefacts on flat areas. As previously mentioned, Beltrami regularization can be used to further improve denoising quality. The regularization function used in the Beltrami method is defined as

$$\sqrt{1 + \beta^2|\nabla p_i|^2} \quad [18]$$

which proposes a good compromise between the smooth solution of Tikhonov and the edge-preservation of TV due to the Beltrami constant β.

5.3 The Beltrami-regularized denoising filter for parametric mapping technique

Parametric mapping techniques can be severely affect by noise, which can results in a reduction of precision and accuracy. The denoising regularization methods could help improve the SNR of the T1-weighted images, consequently improving precision and

accuracy of the final T1 map. However, it is necessary to adapt the formulation of these techniques in order to exploit the correlation and redundancy observed in the parameter dimension.

Bustin et al. (61) have proposed a novel denoising approach, based on the Beltrami regularization method, which exploits the spatial gradients of each T1-weighted image and the common edge information between T1-weighted images with varying contrast. Two main contributions have been added to the original single-frame Beltrami denoising formulation: a vectorized formulation and an anisotropic term.

5.3.1 Vectorized Beltrami-regularized denoising

The original Beltrami regularization was applied independently on a single frame. If instead the correlation in the spatio-temporal space is considered, then the single-frame Beltrami formulation can be modified as follows:

$$\sqrt{1+\beta^2\sum_{i=1}^{n}|\nabla p_i|^2} \qquad [19]$$

which enforces the presence of same features in different frames p_i, while variations within the same frame are treated as noise. This would allow to weight and preserve the presence of common edges in the different frames.

5.3.2 Anisotropic Beltrami

The isotropic single-frame Beltrami regularization is substituted with an anisotropic term, thus the regularization formulation becomes:

$$\sqrt{1+\beta^2\sum_{i=1}^{n}|\nabla^w p_i|^2} \qquad [20]$$

where the gradient transformation is weighted by a weighting factor w, defined as $w(p_i) = e^{-\frac{(\nabla p_i)^2}{h^2}}$, which penalizes the gradient depending on its local orientation in order

to decrease local smoothing in the directions where sharp transitions are observed. The weight is updated at each iteration of the optimization, and h is a smoothing parameter.

By combining equation [20] in the optimization problem [17], the final formulation for the Beltrami anisotropic denoising is obtained:

$$\widehat{p_i} = \min_{p_i} \left\{ \|p_i - S_i\|_2^2 + \lambda \sqrt{1 + \beta^2 \sum_{i=1}^{n} |\nabla^w p_i|^2} \right\} \qquad [21]$$

5.4 Image analysis

For myocardial T1 mapping technique, accuracy and precision are calculated in order to evaluate the performance of the imaging technique. After an initial validation of the T1 mapping technique using a phantom with known T1 and T2 values, a ROI is usually selected in the myocardial septum of the myocardial T1 map, since this cardiac region is less affected by susceptibility artefacts. Mean and standard deviation of the measurement inside the ROI are calculated and used as an estimate of T1 accuracy and precision respectively. There are no reference gold standard values for myocardial T1, however already available and validated myocardial T1 mapping techniques are used for comparison.

In this thesis, the comparison between the different T1 mapping techniques is performed using the Bland-Altman plot, where mean ± 2 standard deviation (SD) are estimated.

The AHA segmentation is used to evaluate the measured T1 accuracy and precision across the whole left ventricle, allowing a 3D visualization of the heart.(62)

Chapter 6 – 3D myocardial T1 mapping using saturation recovery

The main idea of the study has been conceived and designed by Professor René Botnar, Dr Markus Henningsson (MH) and Giovanna Nordio (GN). MH and GN implemented the sequence in the Philips pulse programming environment, GN performed the acquisition of the data and the statistical analysis. Dr Torben Schneider helped with the implementation of the sequence. Dr Amedeo Chribiri and Dr Adriana D.M. Villa helped with the analysis of the images.

The manuscript was written and reviewed by all authors and it was published in the *Journal of Magnetic Resonance Imaging* (10).

This study was presented at the Society for Cardiovascular Magnetic Resonance (SCMR) in Washington 2017.

6.1 Introduction

As mentioned in Chapter 4, 3D myocardial T1 mapping is desirable since it permits whole coverage of the heart in free-breathing with higher SNR and image resolution. The existing MOLLI and SASHA techniques are 2D imaging techniques and they require an

acquisition during a long breath-hold to compensate for respiratory motion (6,63). Due to the increased scan time associated with higher-resolution 3D image acquisition of the heart, free-breathing imaging is necessary and respiratory motion compensation becomes imperative to ensure diagnostic image quality. Some techniques for 3D T1 mapping have been already proposed (35,64,65). However, these are based on an inversion recovery acquisition and consequently they are heart rate dependent.

Instead the SASHA sequence appears to be a promising candidate for volumetric free-breathing T1 mapping of the whole-heart, due to its high scan efficiency and quantification accuracy and its robustness to heart rate variations, which may occur over the course of a 5-10 minute scan.

In this chapter a multi-shot high resolution 3D myocardial T1 mapping technique based on a saturation recovery acquisition, called 3D SASHA, is presented, combined with a 1D diaphragmatic navigator for respiratory motion compensation. The imaging technique was tested and validated on a T1 phantom and on healthy volunteers.

6.2 Material and methods

6.2.1 Pulse Sequence Scheme

All data were acquired on a 1.5T Ingenia MR system (Philips, Best, The Netherlands). The proposed 3D SASHA pulse sequence enables the acquisition of whole-heart T1 mapping in free-breathing. To this end, the 2D SASHA sequence (6) was modified to make the sequence compatible with a 3D segmented k-space acquisition. The sampling scheme used for 3D SASHA is shown in Figure 6.1a. First, all image k-space segments with no magnetization preparation were acquired, called "infinity image" (by assuming it is acquired after an infinite saturation delay time during data fitting). This was followed by the interleaved segmented acquisition with preceding saturation pulse and increasing

saturation delays. To ensure all k-space segments of the infinity image were acquired at equilibrium magnetization, "pause" cardiac cycles were added between the acquisitions of these segments. During these pauses, all RF pulses and data acquisition were switched off to allow for full T1 recovery.

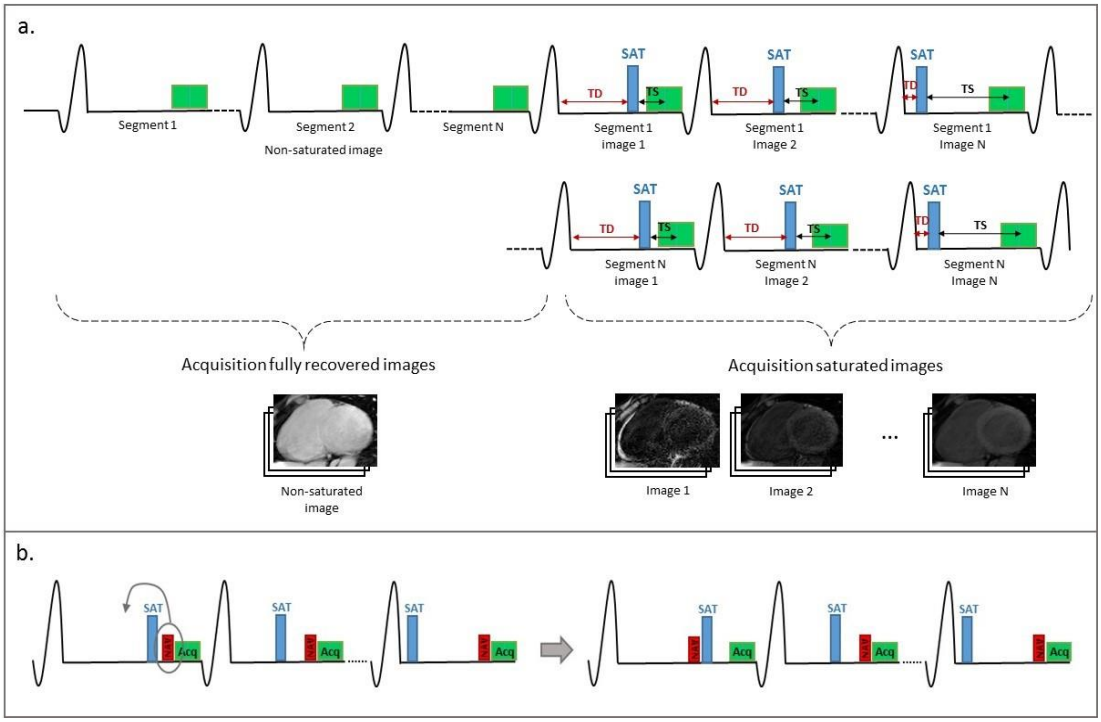

Figure 6.1: a) Schematic diagram of the 3D SASHA pulse sequence. First the images without any magnetization preparation are acquired, then an interleaved acquisition is used for the saturated images, where the saturation times (TS) and the delay time (TD) is varied. b) For the shortest TS the position between the saturation pulse (SAT) and the navigator (NAV) is swapped.

To compensate for respiratory motion a 1D dNAV was used. Typically the navigator is performed immediately before the image acquisition to allow prospective motion correction and ensure high temporal correlation between the 1D dNAV and image acquisition. However, for the shortest saturation time the navigator signal may be insufficient for reliable motion estimation. Therefore, the position between the saturation pulse and the navigator was swapped for the shortest saturation time (40 ms) (Figure 6.1b).

To minimize the sensitivity to B_1 inhomogeneities the saturation pulse used for imaging was a composite saturation pulse with a train of four rectangular pulses with numerically optimized flip angles (respectively 72˚, 92˚, 126˚, 193˚) each followed by a dephasing gradient (66). Imaging was performed with a combination of 12-channel posterior and 16-channel anterior torso coils coil and the heart rate was monitored using the vector electrocardiogram (VCG) for the whole duration of the scan.

Data acquisition was performed with a segmented 3D bSSFP technique and imaging parameters included: FOV = 300 x 300 x 90 mm^3, TR/TE = 3.2/1.6 ms, image resolution = 1.4 x 1.4 mm^2, slice thickness = 8 mm, FA = 35°, parallel imaging with SENSE factor of 2 in phase encoding direction, 10 start-up echoes, Cartesian acquisition with radial k-space shutters, slice-selective RF pulse. Thirty segments of the k-space were acquired per heart-beat with a low -high k-space ordering and an acquisition window duration of 90ms.

6.2.2 Simulations

The proposed segmented multi-shot SASHA pulse sequence was simulated using the Bloch equations in MATLAB R2014a (The MathWorks; Natick, USA). The simulations were performed to analyze the effect of the added “pause” cardiac cycles between acquisitions of the infinity images and to investigate the optimal number of pauses for a given heart rate to ensure complete longitudinal magnetization recovery. The simulations for a SSFP sequence were performed for heart rates between 60-100 beats per minute (bpm), T1 of 1100 ms (pre contrast myocardial T1 at 1.5T), T2 of 45 ms, 40 RF excitations per segment, flip angle (FA) of 35°, TR of 2.8 ms, and for different numbers of “pause” cardiac cycles.

6.2.3 Phantom Experiments

A phantom with 9 agar/$NiCl_2$ vials was used for imaging, with T_1 values ranging from

250ms to 1500 ms (67), to compare T1 measurements between the gold standard inversion-recovery spin echo (IRSE) technique, 2D MOLLI, 2D SASHA and the proposed 3D SASHA. The IRSE pulse sequence was performed with ten inversion times varying from 100 to 2000 ms. The reference T1 measurements were compared to 2D MOLLI, 2D SASHA and the proposed 3D SASHA, in order to validate the imaging technique. Sequence parameters for the spin echo sequence were: FOV = 200 x 200 mm^2, image resolution = 3.1 x 3.1 mm^2, 10 mm slice thickness, TR = 8000 ms and TE = 5.9ms. The 3(3)3(3)5 2D MOLLI sequence was acquired with the following parameters: FOV=300x280mm, TR/TE = 2.6/1.3, image resolution = 1.7 x 2.1 mm, slice thickness = 10 mm, FA = 35°, scan time of about 12 seconds. The acquisition parameters for the 2D SASHA sequence were: FOV = 300 x 280 mm^2, TR/TE = 2.6/1.3, image resolution = 1.7 x 2.1 mm^2, slice thickness = 10 mm, FA = 70°, 100-700 ms TS for a heart rate of 60 bpm, parallel imaging with SENSE factor of 2 in phase encoding direction. For the 3D SASHA sequence the TS were 100-700 ms for a heart rate of 60 bpm. All three imaging techniques were reconstructed to the same in plane resolution of 1.25 x 1.25 mm^2.

The proposed 3D SASHA sequence was acquired with fewer T1-weighted images along the Mz recovery curve compared to the conventional 2D SASHA sequence (nine instead of eleven, including the “infinity” image) in order to keep the total scan time within 5 minutes.

All sequences were triggered with a simulated heart rate of 60 bpm and signal reception was performed with a combination of the 12-channel posterior and 16-channel anterior torso coils.

To validate the findings of the simulations and evaluate the optimal flip angle and number of “pause” heart cycles added between acquisitions of the fully recovered “infinity” images, the phantom was imaged using the 3D SASHA sequence with different number

of pauses and by changing the flip angle within the range from 25° to 85° with 10° increments. This experiment was repeated for 3D SASHA with 0, 1, 2 and 3 pause cycles for the infinity image.

6.2.4 In Vivo Studies

The study was performed in accordance with the Declaration of Helsinki (2000). All subjects involved in this study provided written informed consent with study approval from the institutional review board (15/NS/0030). Ten healthy volunteers without a history of heart disease were imaged using 2D MOLLI, 2D SASHA and 3D SASHA sequences. The same imaging parameters used for the phantom experiment were employed for the in vivo study. The acquisition of the 3D SASHA sequence was performed in free-breathing with a nominal scan duration of 4:14 (min:sec) for a heart rate of 60 bpm and 100% scan efficiency. A 1D diaphragmatic navigator was used for respiratory motion compensation with a gating window of 5 mm and a tracking factor of 0.6. Following the validation with Bloch simulations and phantom studies, three "pause" cardiac cycles were used for all in-vivo imaging.

6.2.5 Image Analysis

The T1 maps were reconstructed offline using MATLAB (The MathWorks; Natick; USA). The T1 values were calculated by fitting the image signal intensities to a three-parameter exponential recovery curve using the fitting procedure proposed by Barral et al. (68). The T1 fit of both the phantom and in vivo reconstructed T1 maps was evaluated to ensure good quality data. ROIs were manually drawn on the phantom images and in the myocardium and the measured average T1 values were expressed as mean ± standard deviation.

Accuracy and precision are the two criterions used to evaluate the efficiency of quantitative T1 mapping (16). For the phantom experiments the accuracy of the 3D

SASHA T1 maps was evaluated by comparing the mean T1 values with the reference measurements from the IRSE experiment using a Kruskal-Wallis test. A Bland-Altman analysis was performed to compare the different techniques and to evaluate the agreement between them. For in vivo studies the myocardial T1 values were compared with the values measured with the 2D SASHA and 2D MOLLI sequences.

The standard deviation of the T1 measurements was used to quantify the precision, i.e. the spatial variability of T1 across the selected ROI, of each imaging technique (9).

Sharpness of the myocardial borders was used as a criterion to quantify the performance of motion correction and was measured using dedicated software. The sharpness was calculated as a percentage of the steepness of the edges of the myocardium, where 100% corresponds to an ideal step edge (69). Measurements were done on the myocardial septum for both the 2D SASHA and the 3D SASHA T1 maps. Two blinded expert reviewers (Reviewer 1 with more than 10 years, and Reviewer 2 with 5 years of experience in cardiovascular MR) scored the T1 maps of all volunteers based on image quality, which includes both myocardial sharpness and signal homogeneity. The scale for scoring the image quality was: 1 poor, 2 average, 2 good, 3 very good and 5 excellent image quality. The Wilcoxon rank t-test was used to evaluate the statistical difference between 2D SASHA and 3D SASHA. The median was calculated and presented together with the 75% and 25% of the median itself (70).

The AHA 17 segments (62) models for the 2D SASHA and 3D SASHA techniques were used to compare the two techniques and to provide a 3D visualization of the left ventricle. The myocardial T1 values of the whole volume were measured for 16 AHA segments (excluding the apical segment 17, not included in short axis view as per clinical standard) in three slices (apex, mid, base). Each segment of the final model was calculated as the average of the same segment between all the volunteers.

For statistical analysis GraphPad Prism version 5 for Windows, GraphPad Software, La Jolla California USA, was used and *p*-values <0.05 were used to define the statistical significance.

6.3 Results

6.3.1 Simulations

Figure 6.2 shows the steady-state M_z magnetization for a tissue with T1 similar to healthy myocardium on 1.5T (T1 = 1100 ms) during the acquisition of the infinity image as a function of different numbers of "pause" cardiac cycles (from zero to three). The recovery of M_z depends both on the number of pauses added between the infinity images and on the heart rate. M_z returns to the equilibrium magnetization after two pause cardiac cycles for heart rates lower or equal than 60 bpm. However three pauses are more robust for higher heart rates, and may ensure full recovery of M_z even in the presence of change in heart rate from 60 to 100 bpm, which can occur during 5 to 10 minutes scan. Thus three pauses were chosen for all in-vivo studies.

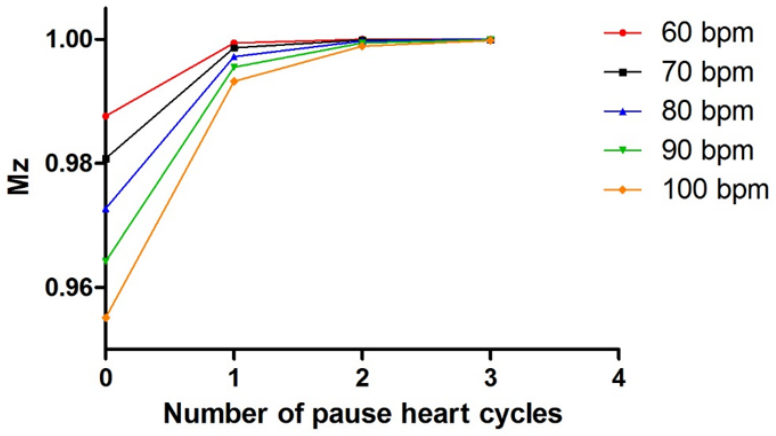

Figure 6.2: The graph shows the recovered longitudinal magnetization Mz (y-axis) as a function of different number of "pause" cardiac cycles (x-axis) between the acquisitions of the images without any magnetization preparation, for different heart rates.

6.3.2 Phantom Experiments

Table 1 summaries the mean values and standard deviations calculated with IRSE, 2D MOLLI, 2D SASHA and 3D SASHA sequences. A ROI was selected for each of the nine vials of the phantom and the average T1 value calculated.

The 3D SASHA T1 map appears more homogeneous and less noisy compared to the 2D SASHA T1 map (Figure 6.3a). 3D SASHA and 2D SASHA were found to have similar accuracy, while 2D MOLLI generally underestimates the T1 values. Although fewer T1-weighted images were used for the 3D SASHA compared to 2D SASHA (9 for 3D SASHA versus 11 for 2D SASHA) the precision of the 3D SASHA is higher, as measured by the lower standard deviation (Figure 6.3b-c).

Table 1: Mean and standard deviation for all the phantom vials, respectively for spin-echo, 2D MOLLI, 2D SASHA and 3D SASHA sequences.

Phantom vial	Reference T1 [ms]	Spin-echo T1 [ms]	2D MOLLI T1 [ms]	2D SASHA T1 [ms]	3D SASHA T1 [ms]
1	430 ms	431.8 ± 10ms	391 ± 5ms	434.9 ± 7ms	442.4 ± 4ms
2 (Myocardial-like)	1090 ms	1111.6 ± 31ms	915.8 ± 5ms	1104 ± 14ms	1091.5 ±9ms
3	458 ms	459.4 ± 9ms	450.2 ±3ms	462.4 ± 6ms	471.2 ± 5ms
4	562 ms	569.3 ± 13ms	498 ± 4ms	571.1 ± 11ms	566.2 ± 6ms
5	1333 ms	1379.7 ± 55ms	1086.8 ± 8ms	1374.3 ± 26ms	1362.6 ± 13ms
6 (Blood-like)	1489 ms	1559.8 ± 62ms	1381.6 ± 8ms	1519.1 ± 26ms	1506.4 ± 19ms
7	300 ms	301 ± 7ms	275.4 ± 3ms	305.2 ± 8ms	310.7 ± 3ms
8	803 ms	811.6 ± 17ms	698.4 ± 4ms	815.1 ± 13ms	799.1 ± 5ms
9	255 ms	253.9 ± 6ms	250.9 ± 4ms	260.7 ± 4ms	268.8 ± 4ms

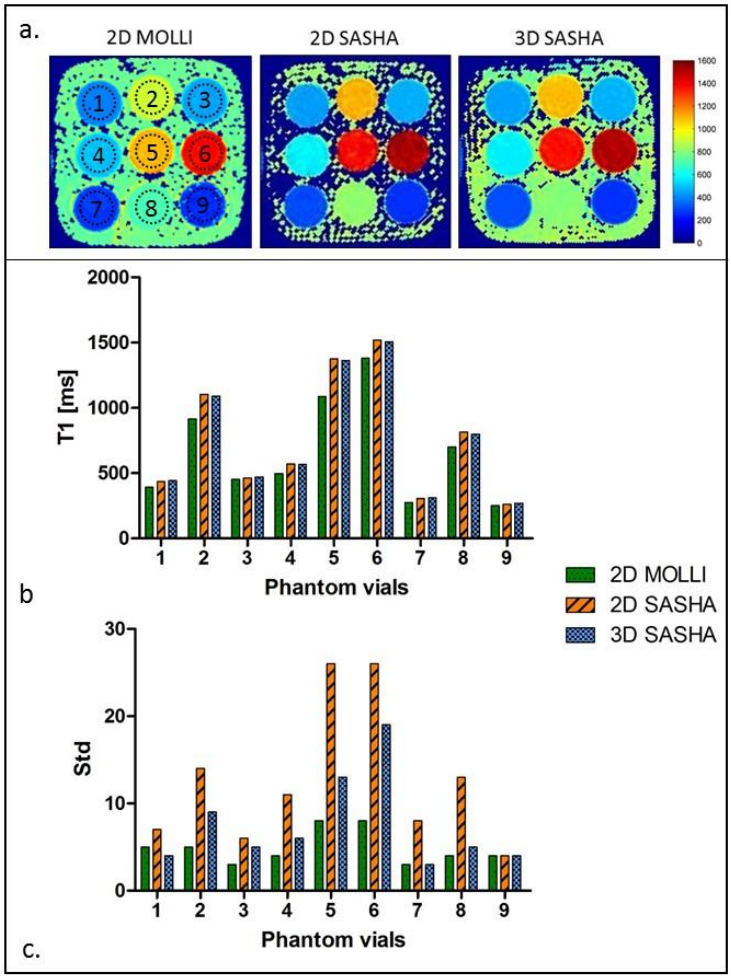

Figure 6.3: a) T1 map of the phantom obtained using the 2D MOLLI, 2D SASHA and3D SASHA sequences. b-c) Mean and standard deviation of the measured T1 values for all the nine vials.

The Bland-Altman analysis in Figure 6.4a compares the reference T1 values measured with the IRSE sequence with the T1 values measured respectively with 3D SASHA and 2D SASHA sequences. For the 3D SASHA the mean difference is 6.6 ms and the limits of 95% agreement are -36.6ms and 49.8ms, while for the 2D SASHA the mean difference is 3.5ms and the limits of 95% agreement are -25.3 ms and 32.3 ms. The 3D SASHA T1 values are in good agreement with the 2D SASHA T1 values with significant correlation ($p<0.0001$, $r=0.9998$). The estimated T1 values using the 3D SASHA and the 2D SASHA sequences correlate extremely well ($r=0.9997$) with the IRSE sequence (Figure 6.4b-c). The agreement in T1 values between the 3D SASHA and IRSE was confirmed by the Kruskal-Wallis test ($P=0.9947$). The T1 estimation for the vial with the highest T1 value

deviated from the expected line of identity due to an insufficient recovery time between successive inversion pulses used for the IRSE sequence. This led to a wrong estimation of the highest T1 values with the IRSE sequence and consequently to a mismatch between the 3D SASHA and the IRSE T1 value for the vial with the highest T1.

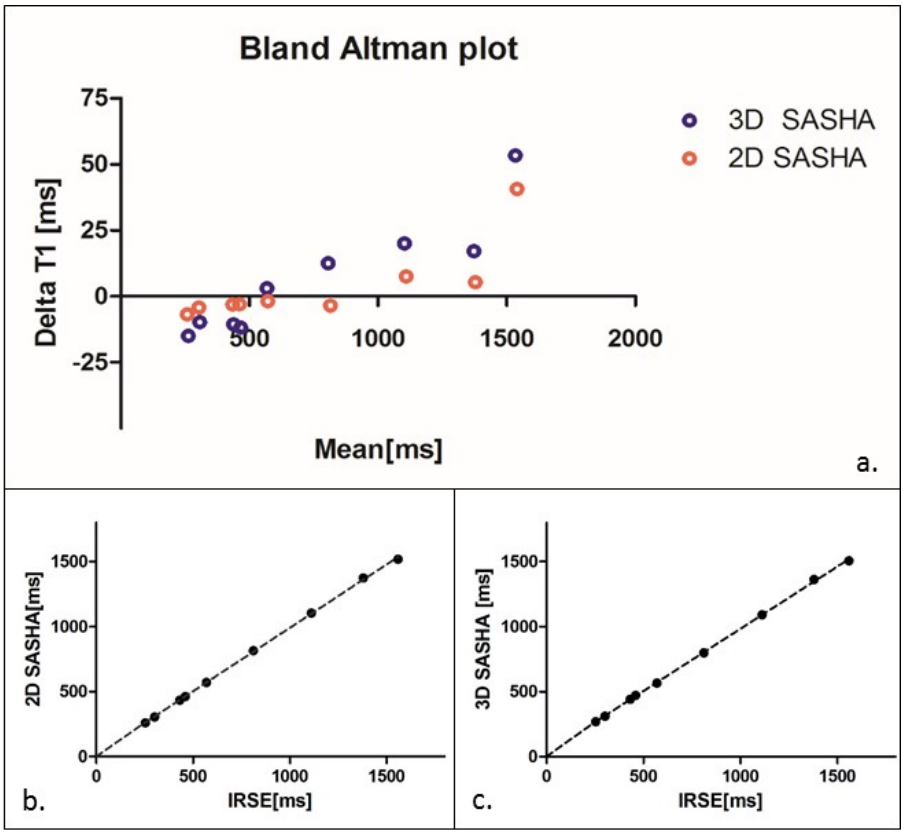

Figure 6.4: a) Bland-Altman analysis between IRSE and 2D SASHA (in red), and 3D SASHA (in blue) sequences for the T1 phantom. b-c) Agreement between IRSE and 2D SASHA and 3D SASHA sequences.

Figure 6.5 shows the results obtained from the phantom experiment using different combination of flip angles and number of "pause" heart cycles; only the results from the vial with myocardial-like T1 are illustrated. The graph shows the difference between the reference T1 value and the measured T1 values, and the best agreement is obtained using a flip angle of 35° and three "pause" heart cycles, which confirms the results obtained from the simulations.

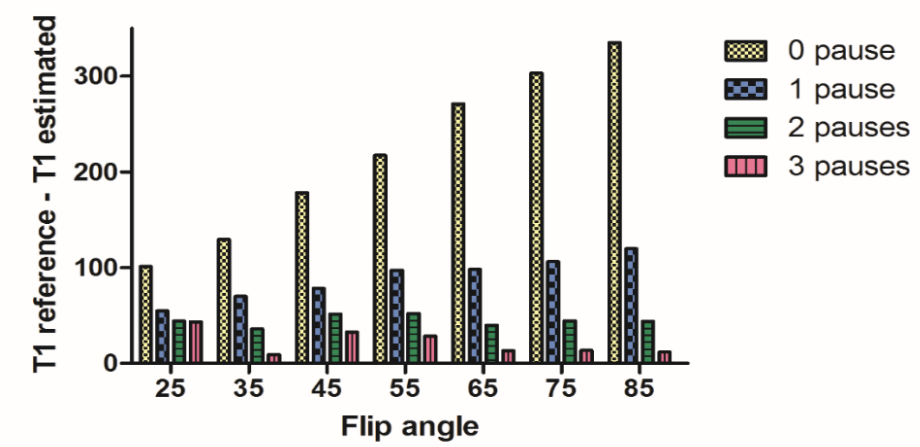

Figure 6.5: The graph shows the difference between the gold standard T_1 and the measured T_1 for the vial number 2 (reference T1 = 1090 ms) on the T1 phantom, using different combination of number of pauses between the acquisition of the "infinity" images (from 0 to 3) and flip angles (from 25° to 85°).

6.3.3 In Vivo Studies

Figure 6.6a shows the myocardial T1 maps of three volunteers obtained with the 2D MOLLI, 2D SASHA and 3D SASHA sequences. The single T1-weighted images acquired for volunteer 2 are shown in Figure 6.6b. For all volunteers there was good agreement between the myocardial T1 values measured with the 2D SASHA and the 3D SASHA sequences, while the T1 values obtained with 2D MOLLI sequence were considerably lower (Figure 6.7a). A trend of improvement in terms of precision was visible with the proposed imaging technique compared with the 2D SASHA (Figure 6.7b). The average T1 values of all subjects for the 2D MOLLI, 2D SASHA and 3D SASHA sequences were 881 ± 32 ms, 1181.2 ± 32 ms and 1153.6 ± 28 ms, respectively.

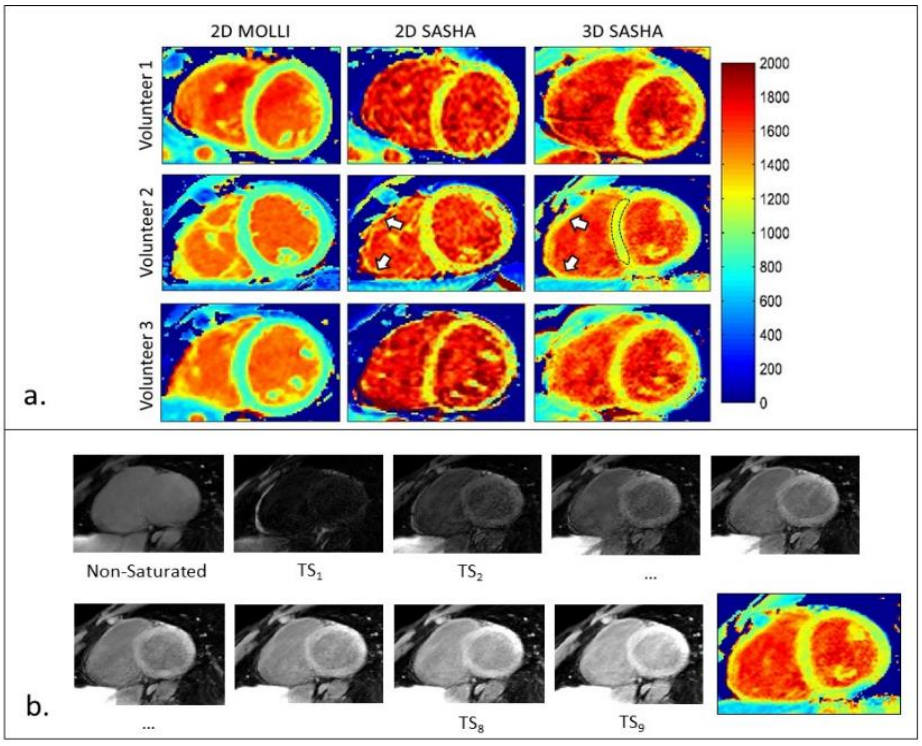

Figure 6.6: a: Mid-ventricular myocardial T1 maps of three healthy subjects using the sequences 2D MOLLI, 2D SASHA, and 3D SASHA sequences. The average T1 values were calculated by manually drawing an ROI in the septum of the myocardium. The higher resolution of the 3D SASHA technique allows to better delineate the right ventricle (white arrows). b: Nine images acquired at different saturation times for

The duration of the 3D SASHA scan was of 12:1 ± 1:3 (min:sec) with a scan efficiency of 32%.

The average myocardial border sharpness measured on the 2D SASHA T1 maps was significantly higher compared to 3D SASHA T_1 maps (respectively 26%±2 and 18%±3).

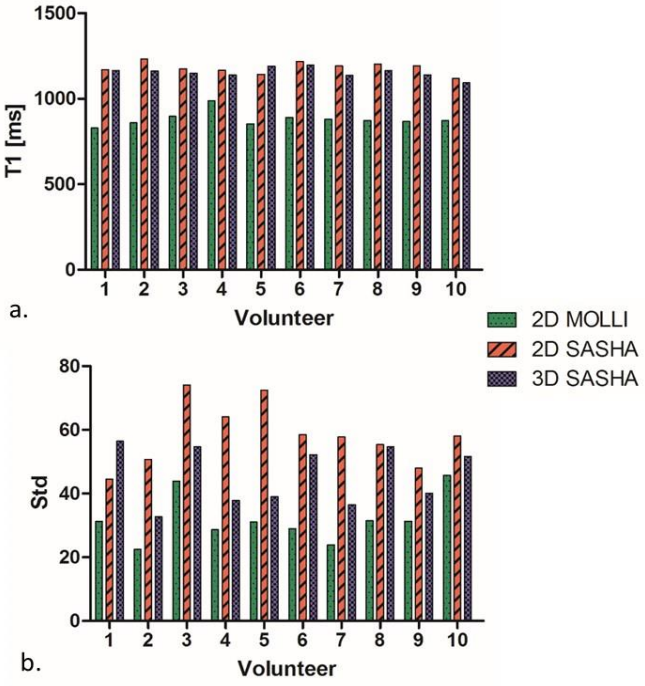

Figure 6.7: Mean and standard deviation of the myocardial T1 measurements of the ten healthy subjects using 2D MOLLI, 2D SASHA and 3D SASHA sequences.

The agreement in image quality between the observers was 80% for the 2D MOLLI T1 maps, and 50% for the 2D SASHA and 3D SASHA T1 maps. In general, a better image quality for the 2D MOLLI T1 maps is observed (median 5, 75% of the median of 5, 25% of the median of 4), with significant statistical difference with both 2D and 3D SASHA (respectively p=0.0053 and p=0.0047). There was no statistical difference between 2D SASHA (median 2, 75% of the median = 3, 25% of the median = 2) and 3D SASHA (median 3, 75% of the median = 3, 25% of the median = 2).

Figure 6.8 shows the bull's eye plots of the left ventricle for the 2D SASHA and 3D SASHA imaging sequences. The AHA model is calculated for both the mean and standard

deviation of the T1 values measured across the left ventricle. The average myocardial T1 values are homogeneous across the left ventricle for both the two imaging techniques. The standard deviation for the 3D SASHA is lower compared to the 2D SASHA, which could be explained by the theoretical higher SNR for the 3D technique. However, higher standard deviation was observed in the inferior wall of the basal slice, which could be explained by slice profile imperfection and motions artefacts.

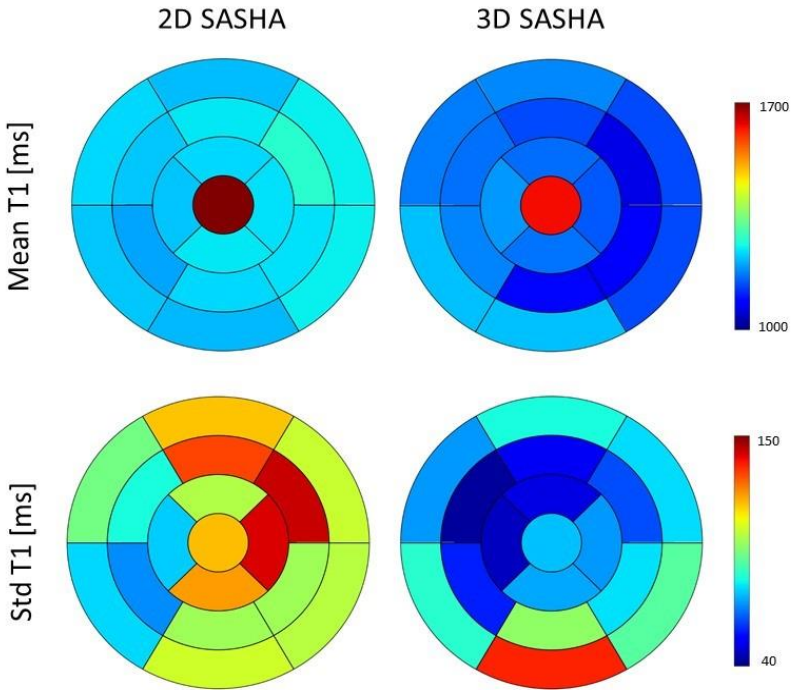

Figure 6.8: Bull's eye plots of the left ventricle. Mean T1 values (top raw) and standard deviations of the T1 measured (bottom raw) are shown for both 2D SASHA and 3D SASHA sequences. Each segment is the average between the ten volunteers and it contains the average myocardial T1. The red central segment represents the blood.

6.4 Discussion

In this study a free-breathing 3D SASHA sequence for T1 mapping of the whole left ventricle has been proposed and validated. The sequence has been validated with simulations, phantom and in vivo experiments.

The proposed 3D T1 mapping approach was based on the well-established 2D SASHA pulse sequence design (6). The main difference between 2D SASHA and the proposed 3D sequence was that segmented k-space acquisition was required to enable high-resolution 3D acquisition. A Cartesian acquisition with radial k-space shutter was used, which is commonly used for magnetization prepared whole-heart imaging. However, no further analysis was conducted to investigate the effect of the acquisition scheme.

The in vivo studies confirm the phantom measurements in terms of accuracy between 2D SASHA and 3D SASHA sequences, as similar average myocardial T1 values were obtained. The standard deviations of the 3D T1 measurements were lower compared to the 2D SASHA. Improved subjective image quality with 3D SASHA over 2D SASHA was observed, although this finding was not significant. This could be attributed to the fact that a 3D imaging sequence inherently benefits from higher SNR compared to a 2D method.

As demonstrated in the phantom experiments, the proposed 3D T1 mapping imaging sequence improves accuracy compared to 2D MOLLI and precision compared to 2D SASHA. This is a promising result and warrants further evaluation of the 3D SASHA imaging technique in clinical practice. Future works will investigate the T2 dependency of the proposed 3D SASHA sequence. Also a free-breathing T1 mapping approach would be useful in patients who cannot hold their breath due to respiratory problems. In this study it was not possible to correctly validate the T1 of the blood, since the T1 phantom used had only T1 values within the range of 250-1500ms. However, a correct estimation of blood T1 would have important further implications for ECV mapping.

Other 3D T1 mapping techniques have been already proposed (35,64,65), which use an inversion recovery pulse to generate T1 weighting. The proposed 3D SASHA technique uses a saturation recovery pulse, which has the advantage of completely erasing the

history of the longitudinal magnetization between the acquisitions, thus reducing the heart rate dependency as well as improving scan efficiency. Further work will investigate other available T1 mapping techniques with the proposed 3D SASHA sequence. For the 3D SASHA imaging techniques, an incomplete and incorrect saturation could be an important source of errors in the final T1 map. In the proposed 3D SASHA sequence a composite saturation pulse has been used, with a saturation efficiency of 0.989 ± 0.005, estimated from the exponential fitting curve (6). The high saturation efficiency confirms the results already reported from previous studies (6). The sharpness of the septum was significantly lower with the 3D SASHA compared to the 2D SASHA T1 map. This is likely due to residual respiratory motion artefacts. Improved respiratory motion compensation strategies, such as self-navigation (71) or image-based navigation (48,52,72) may improve image sharpness while simultaneously helping to reduce scan time. Nevertheless, the visual score test showed a trend of improved image quality for the 3D SASHA compared to the 2D SASHA T1 maps. In general better image quality and better visualization of the myocardial borders would be beneficial where trasmurality of scar should be assessed. In addition, high resolution T1 mapping may be especially beneficial for fibrosis quantification in the thin wall of the right ventricle. However, with the proposed 3D SASHA T1 mapping sequence it is still challenging to quantify the thin wall of the right ventricle due to the limited spatial resolution. Higher and isotropic spatial resolution, as well as more advanced respiratory motion compensation techniques, would be necessary in order to quantify small structures. The AHA model showed in general a good homogeneity of the myocardial T1 values measured across the left ventricle. However, T1 values in the lateral wall of the mid ventricle were somewhat lower compared to other segments. This is consistent with previous findings showing lower T1

values in this region, which is likely due to susceptibility artefacts caused by the air-myocardium interface (73).

In this work a 3(3)3(3)5 MOLLI scheme was used, which was the clinically used T1 mapping technique at the time of the study. Recently, the 5-3 MOLLI scheme has become more popular, due to the shorter breath-hold duration. Further work is required to compare the precision, accuracy, and clinical merits of more recent T1 mapping techniques with the proposed 3D SASHA (74).

The proposed 3D SASHA imaging sequence has been extensively tested and validated with simulations, phantom studies and in vivo experiments on healthy volunteers. Simulations with heart rates in the range of 60-100 bpm have been used to identify the number of pause heart cycles that ensure full recovery of the magnetization. Further simulations with higher ranges of heart rate would potentially highlight benefits of using the 3D SASHA compared to the 2D MOLLI imaging sequences. Further work is also required to evaluate this technique in patients with myocardial scar, as well as for post-contrast T1 mapping.

Image resolution of the 3D SASHA sequence is mainly limited by the scan time, which is approximately 12 minutes for the current spatial resolution of 1.4 x 1.4 x 8 mm^3. The implementation of novel motion compensation techniques, such as image-based navigation, correcting for both translational and non-rigid motion (48), removes the requirement for gating and allows to use all acquired data for image reconstruction thereby significantly reducing scan time or increasing spatial resolution. In addition, improved motion compensation may also improve myocardial sharpness and overall image quality. The use of compressed sensing reconstruction could also further accelerate imaging time (75).

An additional step of retrospective image registration (76) or removal of severely motion corrupted images could be beneficial to correct for residual motion in the T1 map, which could further improve the reliability of the T1 measurements.

Scan time is also affected by the number of pauses added between the k-space segments of the infinity images. Reduction of the number of pauses could be achieved by introducing some subject specific correction in the fitting step. A reduced number of images acquired with the 3D SASHA sequence could be another possible solution to shorten the acquisition time, although the trade-off between quantification precision and total acquisition time will have to be investigated further.

In conclusion, the proposed 3D SASHA T1 mapping technique allows acquiring high-resolution myocardial T1 maps of the whole left ventricle completely in free breathing with good accuracy. While the accuracy is in the range of the 2D SASHA sequence, the precision is improved.

Chapter 7 - 3D SASHA myocardial T1 mapping with high accuracy and improved precision

The main idea of the study has been conceived and designed by Professor René Botnar, Dr Claudia Prieto, Dr Freddy Odille, Giovanna Nordio (GN) and Dr Aurelien Bustin (AB). GN implemented the imaging sequence, acquired and analysed the data, AB implemented the denoising algorithm and analysed the data.

The manuscript was written and reviewed by all authors and it was published in the *Magnetic Resonance Materials in Physics, Biology and Medicine* journal (11).

This study was presented by GN at the Society for Cardiovascular Magnetic Resonance (SCMR) in Barcelona 2018, and at the 26th Scientific Meeting of the International Society for Magnetic Resonance in Medicine meeting in Paris, France 2018.

7.1 Introduction

Chapter 6 presents a new 3D saturation recovery based myocardial T1 mapping technique, which permits to acquire the whole left ventricle under free-breathing conditions. This technique has been successfully validated in healthy subjects and showed

higher accuracy in the estimation of myocardial T1 than the clinically used inversion recovery based 2D MOLLI technique. Although the precision of the 3D SASHA T1 map has been shown to be superior to 2D SASHA, it is still lower than that of 2D MOLLI. This lower precision is due in part to the low dynamic range of the signal intensity when using saturation pulses, which makes saturation-recovery-based T1 mapping sequences more sensitive to noise. A precise estimation of myocardial T1 values is important to achieve higher reproducibility and ultimately improve diagnostic utility.

To address this issue, efficient 2D denoising techniques have been recently proposed to reduce noise in the native T1-weighted images, while preserving the inherent cardiac structures (61,77). Jang *et al* (77) employed 2D denoising based on a tissue similarity distance to reduce the sensitivity to noise of 2D STONE (35) T1 mapping when three-parameter fitting is employed. Bustin *et al* (61) developed a 2D denoising method using the Beltrami regularization to improve the precision of 2D breath-hold saturation-based myocardial T1 mapping sequences while maintaining accuracy of T1 quantification. This feature preserving regularization technique can greatly reduce the staircasing effect (78) often associated with other regularity priors. In this study, the use of the Beltrami regularization denoising approach to further improve the precision and image quality of the 3D free-breathing SASHA sequence is investigated. The Beltrami denoising framework will be investigated to exploit the spatio-contrast variation correlation in the native 3D T1-weighted images.

7.2 Material and Methods

7.2.1 3D Denoising

The Beltrami regularization for image denoising and enhancement was introduced for 2D natural images by Sochen, Kimmel and Malladi (79) and proposed for 2D MRI

myocardial T1 mapping denoising by Bustin *et al* (61). The potential of the Beltrami regularization framework lies in the general definition of the space-feature manifold and the choice of its metric. In particular, the regularization can be chosen such that the energy of the unknown image corresponds to an arbitrary interpolation between quadratic or total variation gradient penalties.

In this work, the Beltrami denoising framework is applied to 3D T1 mapping by exploiting the 3D spatial and T1 recovery dimension redundant information. This approach thus exploits the 3D spatial gradients of each T1-weighted image and the common edge information between T1-weighted images with varying contrast. A coupling between the T1-weighted images is performed as described by Bustin *et al* (61), to enforce common edge information across the 3D images in the T1 encoding direction. With this approach, common structures/edges in different T1-weighted images are preserved, while local intensity variations specific to each T1-weighted image are treated as noise, and thus reduced. Therefore, edges/details in the images will be better enhanced if they are present in multiple T1-weighted images.

Following the derivation in (8), the 3D Beltrami denoising framework for 3D T1 mapping can be expressed as the following optimization problem:

$$\widehat{m}_i = argmin_{m_i}\left\{\|m_i - d_i\|_2^2 + \lambda\sqrt{1+\beta^2\sum_{i=1}^{n}|\nabla^w m_i|^2}\right\} \quad [22]$$

where$\{\widehat{m}_i\}_{i=1}^{n}$ are the denoised 3D T1-weighted images for the contrasts $i = 1, \dots, n$, $\{d_i\}_{i=1}^{n}$ are the corresponding 3D T1-weighted images before denoising, λ is the regularization parameter that controls the trade off between the fidelity to the original acquired data and the Beltrami regularization term, β is the Beltrami constant that allows selection of any arbitrary interpolation between quadratic or total variation gradient penalties and$\{\nabla^w m_i\}_{i=1}^{n}$ are the 3D weighted-gradient transformation applied to the 3D

T1-weighted images with varying contrast. The weighted-gradient functions penalise the gradients depending on their local orientation in order to decrease local smoothing in the directions where sharp transitions are observed, with $w(m_i) = e^{-\frac{(\nabla m_i)^2}{h^2}}$ updated at each iteration of the optimization and h a smoothing parameter.

The optimization problem described above was solved using an efficient and simple primal-dual hybrid gradient algorithm (12,13). The parameters λ and h were set to 0.25 and 5 respectively, for all the experiments. These parameters were empirically optimized on three representative datasets to provide the best image quality and then the same parameters were employed in the remaining cases. A weight of 1.0 was employed for the Beltrami constant as indicated in (78).

7.2.2 Imaging

All imaging studies were performed on a 1.5T MR scanner (Ingenia, Philips, Best, The Netherlands). T1 mapping was performed using the saturation-based 3D SASHA sequence described in (10). Phantom and cardiac studies used a 28-channel coil. The images from phantom and healthy subjects were collected from the scanner in DICOM format and were loaded into a computer for offline image processing and analysis using MATLAB (MathWorks, Natick, MA).

7.2.3 Phantom Experiment

To evaluate the performance of the proposed 3D denoising algorithm on accuracy and precision of T1 values, a standardized phantom containing nine agar/$NiCl_2$ vials was used, with T1 values ranging from 250 to 1500 ms (67). The phantom was imaged using the gold standard 2D inversion-recovery spin echo (IRSE), the 2D MOLLI (3(3)3(3)5) and the proposed 3D SASHA imaging techniques. Acquisitions parameters for the 2D IRSE sequence were: FOV = 150 × 150 mm^2, image resolution = 1.95 × 1.95 mm^2, 10 mm slice

thickness, 20 TI varying from 50-5000 ms, TR(i) = 7000 ms plus the variable inversion time TI(i), and TE = 6 ms. Acquisition parameters for the 2D MOLLI sequence included: FOV = 300 x 280 mm, image resolution = 1.7 x 2.1 mm^2, slice thickness = 10 mm, TR/TE = 2.6/1.3 ms, FA = 35˚, acquired matrix = 176 x 132, scan time of 12 seconds. The acquisition parameters for the 3D SASHA sequence were: FOV = 300 x 300 x 90 mm^3, TR/TE = 3.2/1.6 ms, image resolution = 1.4 x 1.4 x 8 mm^3, FA = 35˚, acquired matrix = 216 x 214, saturation time within the range of 100-700 ms for a heart rate of 60 bpm, parallel imaging with a SENSE factor of 2 in the phase-encoding direction, nominal scan time approximately 4 minutes. Nine T1-weighted images were acquired, including one image without any magnetization preparation and eight images at different saturation times. All three imaging techniques were reconstructed to the same in-plane resolution of 1.25×1.25 mm^2.

7.2.4 In-vivo experiments

All subjects recruited to this study provided written informed consent with study approval from the Institutional Review Board (1/11/12). Fifteen healthy subjects without a history of cardiovascular disease were imaged using the 2D MOLLI and 3D SASHA sequences in the short-axis plane, using the same imaging parameters as for the phantom experiment. A total of eleven slices were acquired for the 3D SASHA sequence, with a slice oversampling factor of 1.14. The acquisition of the 3D SASHA sequence was performed in free-breathing with a nominal scan duration of 4:14 (min:sec) for a heart rate of 60 bpm and 100% respiratory scan efficiency. A 1D diaphragmatic navigator was used for respiratory motion compensation with a gating window of 5 mm and a tracking factor of 0.6 in the foot-head direction.

7.2.5 Image analysis

The 3D Beltrami denoising was applied to the magnitude 3D T1-weighted images of the 3D SASHA acquisition prior to performing the T1 fitting. T1 maps were reconstructed offline using MATLAB with a three-parameter fitting model for the T1-weighted images before and after denoising (68). A spatially matching ROI was manually drawn on the T1 map of the 2D IRSE (phantom only), 2D MOLLI, 3D SASHA before ('non-denoised 3D SASHA') and after ('denoised 3D SASHA') denoising in all vials for the phantom experiment as well as in the septum of the myocardium for the *in vivo* data. The mean and standard deviation of the T1 measurements were calculated and used as an estimation of accuracy and precision of the respective T1 mapping techniques. A Bland-Altman plot was used to compare the different imaging techniques for the phantom study. The precision measured on the 2D MOLLI, non-denoised and denoised 3D SASHA T1 maps of the healthy subjects were compared using a Mann-Whitney U-test. An AHA segmentation (62) was used to compare the accuracy and precision of the 3D SASHA before and after denoising and for a 3D visualization of the left ventricle. The cardiac volume was represented in 16 segments and three slices (apex, mid and base), with the segment 17 corresponding to the blood pool. The value in each segment was averaged within the fifteen healthy subjects.

For statistical analysis, GraphPad Prism v5 for Windows (GraphPad Software, La Jolla, CA) was used. Two-tailed values of $P < 0.05$ were considered statistically significant.

7.3 Results

7.3.1 Phantom experiments

2D MOLLI, non-denoised and denoised 3D SASHA T1 maps are shown in Figure 7.1 for the phantom experiment.

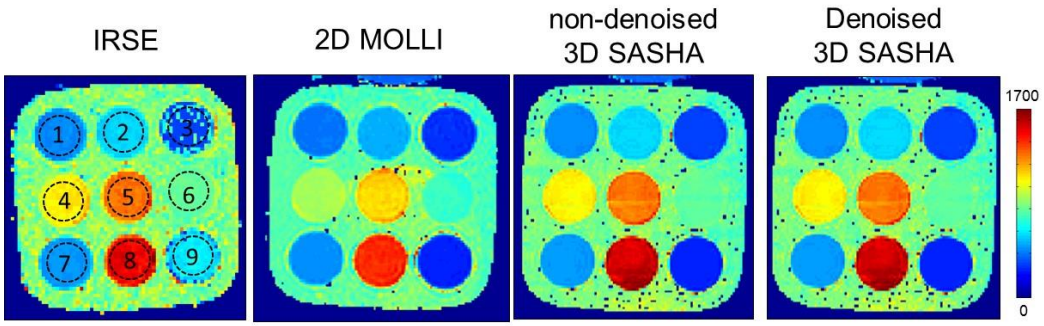

Figure 7.1: T1 maps of the T1 phantom using the following imaging sequence: IRSE, 2D MOLLI, 3D SASHA before and after denoising.

Mean and standard deviation values obtained for all the vials in the phantom for 2D IRSE, 2D MOLLI, and 3D SASHA before and after denoising are summarized in Table 2.

Table 2: Mean and standard deviation measured in all the vials of the T1 phantom using the imaging sequences: IRSE, 2D MOLLI, 3D SASHA before (non-denoised) and after

# vial	IRSE [ms]	2D MOLLI [ms]	non-denoised 3D SASHA [ms]	denoised 3D SASHA [ms]
1	428 ± 10	404 ± 7	433 ± 4	434 ± 4
2	559 ± 10	508 ± 8	560 ± 5	561 ± 4
3	309 ± 9	281 ± 12	306 ± 3	306 ± 3
4	1078 ± 24	934 ± 9	1067 ± 15	1061 ± 14
5	1283 ± 24	1150 ± 16	1272 ± 20	1277 ± 20
6	792 ± 13	737 ± 10	786 ± 8	789 ± 8
7	456 ± 8	454 ± 6	457 ± 4	458 ± 3
8	1507 ± 34	1459 ± 20	1555 ± 32	1565 ± 29
9	254 ± 6	252 ± 5	253 ± 2	253 ± 2

Accuracy and precision of the T1 values obtained before and after applying the 3D denoising technique to the phantom images are shown in Figure 7.2. The standard deviation measured on the 3D SASHA before and after denoising is quite small (2-30ms. As previously shown (10), 3D SASHA before denoising is highly accurate compared to the gold standard 2D IRSE, while 2D MOLLI generally underestimates the T1 values. The Bland-Altman plots in Figure 7.3 show the T1 underestimation typical of 2D MOLLI

(Figure 7.3a), and good agreement between the 2D IRSE and the 3D SASHA before (Figure 7.3b) and after (Figure 7.3c) denoising. For some vials of the phantom, the accuracy of the denoised 3D SASHA is slightly higher, with an increase of just few milliseconds (about 0.3%).

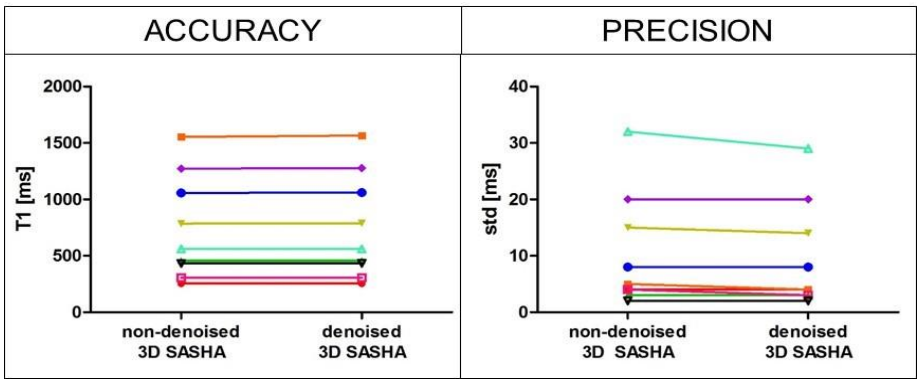

Figure 7.2: Comparison of the accuracy and precision of the 3D SASHA T1 map measured before (non-denoised 3D SASHA) and after (denoised 3D SASHA) applying the 3D denoising technique on all the vials of the phantom. Each colour of the graph corresponds to a different vial of the T1 phantom.

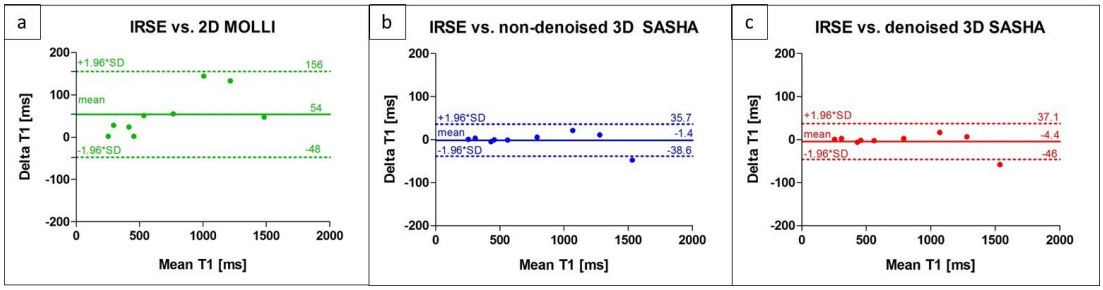

Figure 7.3: Bland-Altman plots comparing the gold standard inversion recovery (IRSE) technique with the 2D MOLLI (a), the non-denoised 3D SASHA (b) and the denoised 3D SASHA (c) techniques acquired on the T1 phantom. The bias and 95% limits of agreement are reported for each graph.

7.3.2 In vivo experiments

The total scan time for the 3D SASHA acquisition in healthy subjects was of 12:4 ± 1:1 (minutes:seconds) with an average scan efficiency of 36% and heart rates of 60-70 bpm. Figure 7.4 shows the average accuracy and precision for all healthy subjects measured on the 2D MOLLI T1 maps, and the non-denoised and denoised 3D SASHA T1 maps for a mid-ventricular slice (Figure 7.4a-c), as well as the Bland Altman plots comparing the T1

measurements and the precision of non-denoised 3D SASHA vs. denoised 3D SASHA (Figure 7.4b-d). There was a significant difference between the accuracy measured with 2D MOLLI and non-denoised and denoised 3D SASHA (P<0.0001), which confirms the typical T1 underestimation of the 2D MOLLI technique (Figure 7.4a). There was a statistical difference between the precision measured with 2D MOLLI and the non-denoised 3D SASHA (P = 0.005), and between the non-denoised and denoised 3D SASHA (P = 0.007). Conversely there was no statistical difference between 2D MOLLI and the denoised 3D SASHA T1 maps (P = 0.95) (Figure 7.4c).

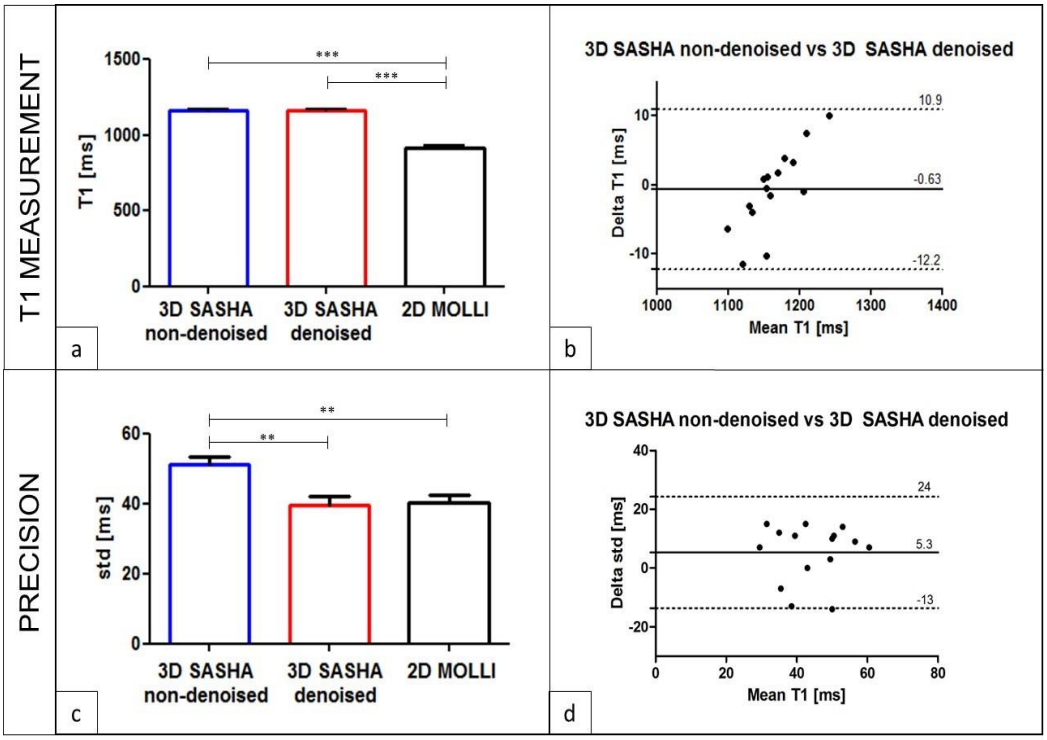

Figure 7.4: a-c) Accuracy and precision of 2D MOLLI and 3D SASHA before (non-denoised 3D SASHA) and after (denoised 3D SASHA denoised) 3D denoising averaged over the fifteen healthy subjects. The precision was measured in a region of interest placed in the myocardial septum of a mid-ventricular slice. Results are expressed as mean ± standard deviation. Differences with statistical significance are identified by *P < 0.05. b-d) Bland Altman plot comparing the accuracy (c) and precision (d) of non-denoised 3D SASHA vs. denoised 3D SASHA. The bias and 95% limits of agreement are reported for each graph.

The impact of the choice of the parameter h and λ on the image quality of the denoised 3D SASHA T1 map is shown in theFigure 7.5. The denoised T1 map becomes sharper

with higher value for the parameter *h*. However a too high value of *h* may result in patch like artefacts. The parameters λ and h were set to 0.25 and 5 respectively for all the experiments.

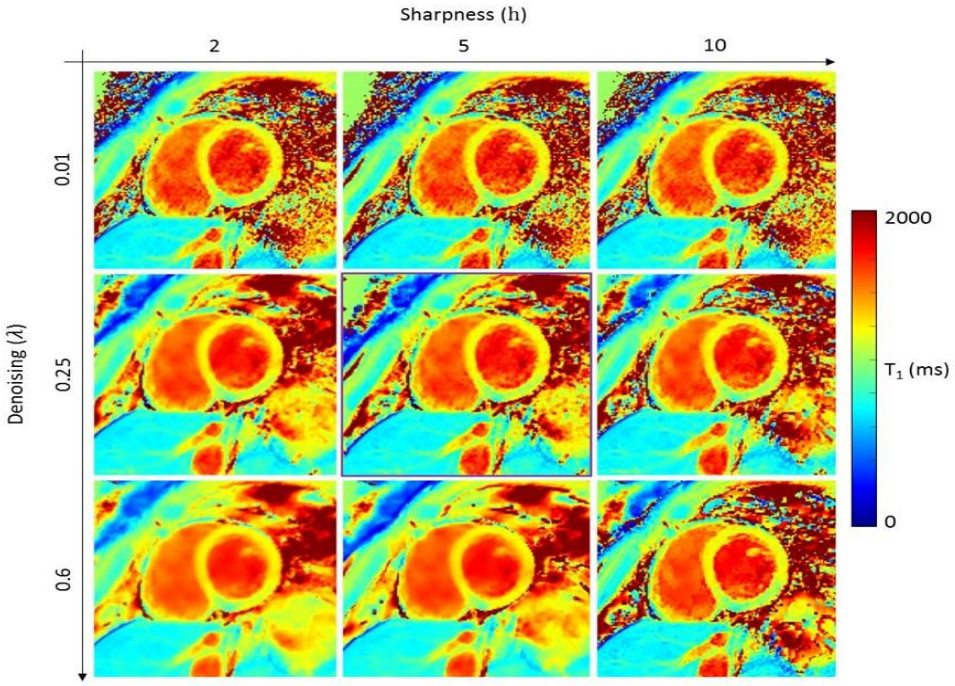

Figure 7.5: Impact of the choice of the parameters h and λ on the image quality of the denoised 3D SASHA T1 map. The sharpness of the structures in the T1 map is controlled by the parameter h, while the denoising effect is controlled by the parameter λ. The higher the sharpness parameter h, the sharper is the denoised T1 map. However a too high value of h results in patchy artefacts.

The accuracy and precision measured for each healthy subject for the 3D SASHA T1 maps computed before and after denoising are shown in Figure 7.6. The measurements were done in an apical, mid ventricular and basal septum. The accuracy was maintained after denoising with no statistical difference in all three slices (apex: $P = 0.38$, mid: $P = 0.88$ and base: $P = 0.35$). There was a significant improvement in precision of measurements in all the three slices, respectively (apex: $P = 0.013$, mid: $P = 0.007$, base: $P = 0.007$).

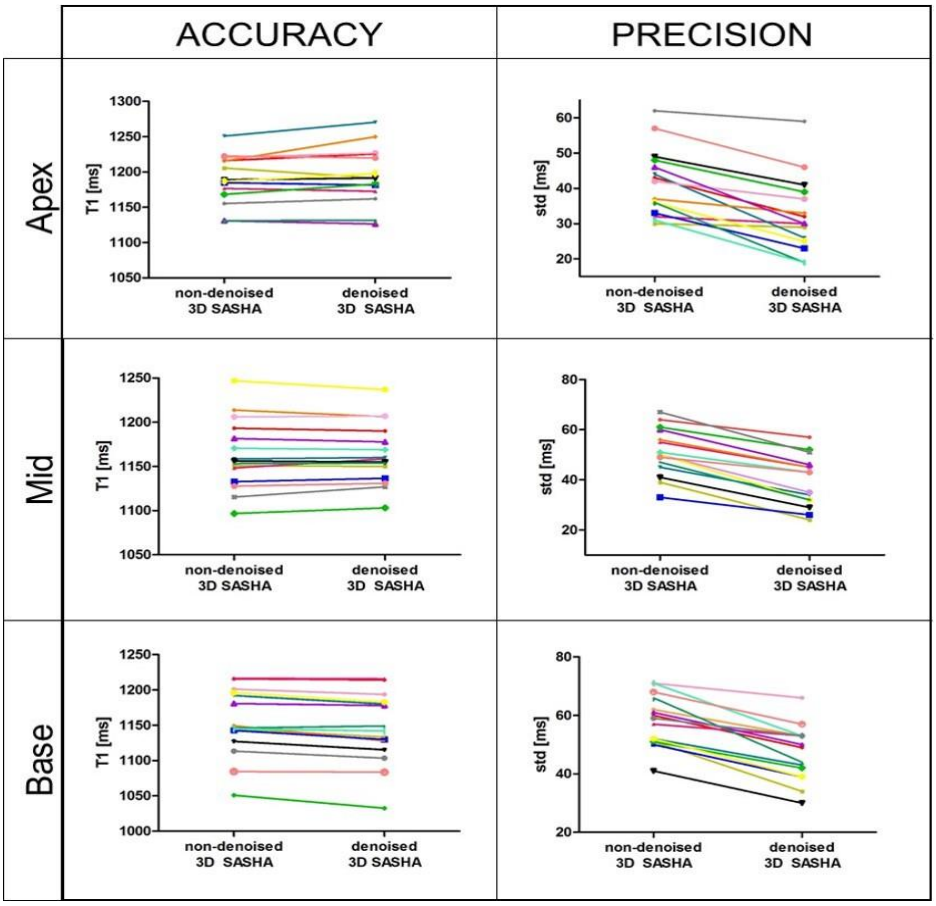

Figure 7.6: Comparison of the accuracy and precision of the 3D SASHA T1 map measured before (non-denoised 3D SASHA) and after (denoised 3D SASHA) applying the 3D denoising technique. The values have been measured in the septum of the myocardium for all subjects in the apical, mid-ventricular and base slices. Each color of the graph corresponds to a different healthy subject.

Figure 7.7 shows the 3D SASHA T1 maps before and after denoising for two representative subjects. The intensity profile in the bottom row of Figure 7.7 shows that after denoising the myocardial borders are maintained with 3D SASHA, while the signal is in general more homogeneous. The corresponding 2D MOLLI T1 maps before and after denoising are also included (mid slice) in Figure 7.7 for comparison purposes. The T1 values are slightly reduced along the inferior-lateral wall, which is probably due to susceptibility artefacts, residual motion or slice profile imperfection.

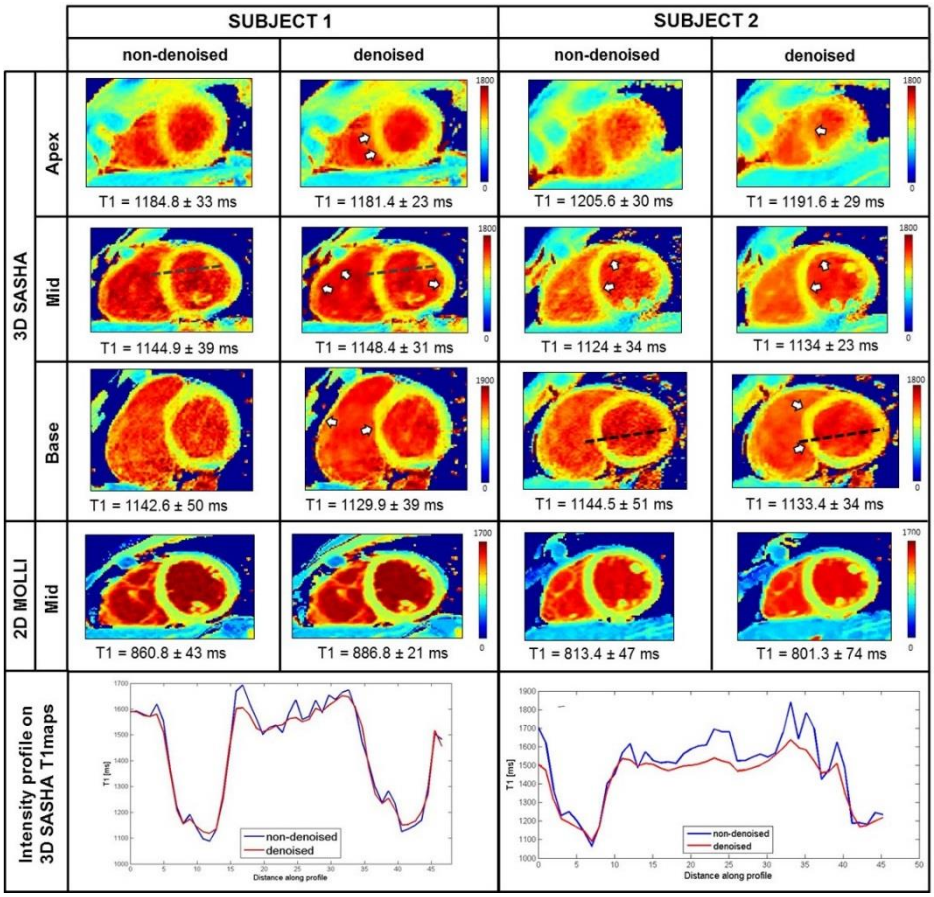

Figure 7.7: Myocardial T1 maps for two representative subjects. Representative T1 maps of the apex, mid and base slice before (non-denoised 3D SASHA) and after (denoised 3D SASHA) 3D denoising are shown in the first three rows. The white arrows show the improved myocardial delineation after denoising. In the forth row the 2D MOLLI T1 maps before and after denoising are shown. The intensity profiles (of the black dotted lines) in the last row show that after denoising the delineation of the myocardial borders and the papillary muscles are maintained, while the signal is in general more homogeneous. T1 values are expressed as mean±standard deviation.

Figure 7.8 shows the single T1-weighted images before and after 3D denoising and the corresponding 3D SASHA T1 map for a representative subject.

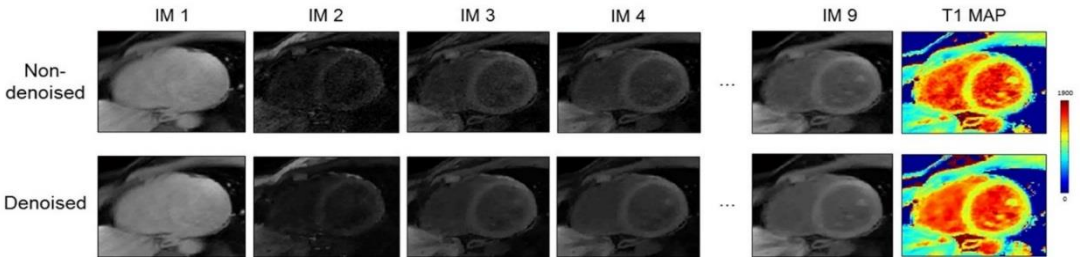

Figure 7.8: Single T1-weighted images before and after 3D Beltrami denoising and the corresponding 3D SASHA T1 map for a representative subject

Figure 7.9 shows the AHA segmentation of the non-denoised and denoised 3D SASHA approaches, both for the mean and standard deviation. In the whole volume the accuracy is maintained virtually constant between the non-denoised and denoised 3D SASHA approaches. The precision improves in all the segments after denoising, with a considerable improvement in precision for the blood pool represented in the central

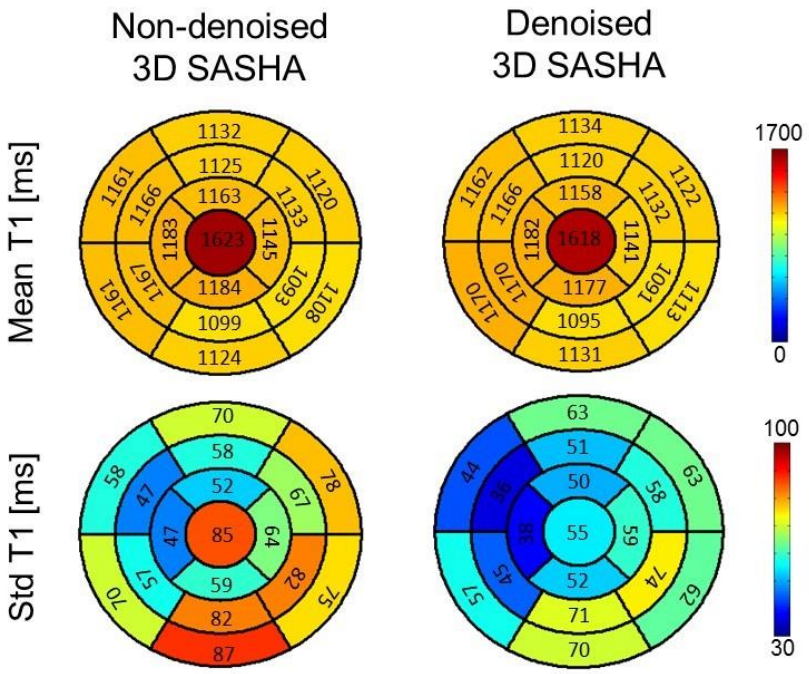

Figure 7.9: AHA segmentation of the left ventricle, shown for the non-denoised and denoised 3D SASHA (n = 15 subjects). The cardiac volume is represented in 16 segments and three slices (apex, mid and base), while the center represents the blood pool. The mean and standard deviation are indicated in all the segments. There is a good homogeneity of the myocardial T1 values across the left ventricle, while the precision improves after denoising particularly for the blood pool. The precision is slightly lower in the inferior-lateral wall, probably due to susceptibility artefacts

segment. There is a general increase of the standard deviation in the inferior-lateral wall, both before and after denoising, due to susceptibility artefacts or slice profile imperfection. The processing time required for the Beltrami denoising on one 3D cardiac volume was about 1 minute.

7.4 Discussion

This study introduces a 3D free-breathing SASHA T1 mapping framework with high accuracy and improved precision following implementation of a denoising step. 3D SASHA T1 mapping is characterized by higher spatial resolution, volumetric coverage and higher accuracy than the clinically used 3-(3)-3-(3)-5 2D MOLLI technique, however, its precision is lower (6,10). This study shows that it is feasible to obtain precision comparable to that of the 2D MOLLI technique while maintaining high accuracy and whole-heart coverage characteristic for 3D SASHA. This is achieved by applying a Beltrami denoising method to the T1-weighted 3D SASHA images prior to the T1 fitting. The denoising technique, proposed for 2D T1 mapping in (61), imposes edge-preserving regularity and exploits the co-occurrence of 3D spatial gradients in the native images by incorporating a multi-contrast Beltrami regularization.

In contrast to the technique presented in (35), where multi-slice denoising using local neighborhood averaging for each pixel was performed, 3D spatial gradients are used to exploit the redundancy and sparsity of the whole 3D volume and Beltrami regularization to exploit sparsity in the T1 recovery dimension. This sparse formulation has the advantage of being robust to high levels of noise and maintain sharp edges while avoiding computationally expensive reconstruction often associated with local filters. Compared to the 2D denoising technique introduced in (61), our framework further exploits

redundancy and sparsity in the whole 3D volume and provides whole-heart volumetric coverage with high in-plane spatial resolution.

As demonstrated in the phantom experiment, the accuracy of the 3D SASHA T1 map before and after denoising is comparable to the gold standard IRSE technique, with a slight increase of few milliseconds for some vials. In terms of precision, the improvement is small, due to the small range of standard deviation. Conversely, with the 2D MOLLI imaging technique the myocardial T1 was underestimated, as previously shown (63,81). *In vivo* experiments in healthy subjects demonstrated preserved accuracy of non-denoised and denoised 3D SASHA. In addition, the precision was considerably improved after denoising, with no statistical difference compared to 2D MOLLI T1 maps. However, 2D MOLLI data were only acquired for one single mid-ventricular slice compared to the 3D SASHA data that were acquired across the whole left ventricle. The AHA segmentation allows for better visualization of the effect of the 3D denoising method on the whole volume, both in terms of accuracy and precision. The precision is in general improved across the whole left ventricle, as well as in the blood pool indicated in the central segment. In fact, the denoising should have a bigger effect in areas with more noise or noise-like structures. As the blood pool signal is more inhomogeneous, we expect the denoising to be more efficient in that area. The variability of the precision measured in the myocardial inferior-lateral wall could be explained by the susceptibility artefacts and some residual motions (82). After denoising the delineation of the myocardial borders and papillary muscles is maintained, while the signal is in general more homogeneous.

For respiratory motion compensation, the 3D SASHA imaging sequence is combined with a 1D diaphragmatic navigator gating and tracking. The navigator generally allows for a respiratory scan efficiency of ~ 50%, however, markedly lower scan efficiencies (20-30%) are often observed in patients with more irregular breathing patterns. An

alternative respiratory motion compensation technique, such as image-based navigation and self-navigation (38,48), would permit 100% respiratory scan efficiency, thus reducing the scan time and consequently potential additional bulk motion artifacts associated with lengthy scans. Compared to 3D SASHA, 2D MOLLI permits to acquire one slice in only 12 seconds of breath hold. However if several slices are acquired, resting periods of at least the same duration of the breath-hold are necessary between the acquisition of each slice. Consequently, to acquire several slices and to achieve the same volumetric coverage of the 3D SASHA presented here, 2D MOLLI would require a total scan time of about 4 minutes. In addition, the 3(3)3(3)5 2D MOLLI has lower image resolution than 3D SASHA, instead a higher resolution would require a longer acquisition window, making the MOLLI scan more susceptible to cardiac motion.

The denoising approach applied in this study is a post-processing step and thus comes at no additional acquisition or reconstruction cost. The additional post-processing time of ~1 min per 3D volume to execute the denoising technique is reasonable and if clinically validated, in-line implementation would be feasible. The integration of the denoising algorithm in the reconstruction step may accelerate and simplify the whole framework and will be investigated in future work. Overall, 3D SASHA with denoising holds promise to provide accurate T1-values with reduced variability, which are current barriers to the widescale adoption of quantitative myocardial tissue characterization techniques in the clinical setting.

7.5 Conclusion

This study demonstrates the feasibility of the 3D Beltrami denoising technique to preserve accuracy and improve precision in myocardial 3D SASHA T1 mapping. Ultimately, this technique could enable accurate and more precise reconstruction of myocardial T1 maps,

with the potential to offer better visual image analysis and improved performance of post-processing procedures such as image registration and segmentation.

Chapter 8 - Accelerated 3D saturation-recovery based myocardial T1 mapping using fewer saturation time points and denoising

The main idea of the study has been conceived and designed by Professor René Botnar, Dr Claudia Prieto, Dr Aurelien Bustin (AB) and Giovanna Nordio (GN). GN implemented the imaging sequence, acquired and analysed the data, AB implemented the denoising algorithm.

The manuscript was written and reviewed by all authors and it has been submitted to the *Journal of Cardiovascular Magnetic Resonance.*

This study was presented by GN at the 26th Scientific Meeting of the International Society for Magnetic Resonance in Medicine meeting in Paris, France 2018.

8.1 Introduction

The free-breathing 3D SASHA (10) imaging technique, presented in Chapter 6, allows to provide whole-heart coverage with higher SNR and image resolution than with conventional 2D approaches. As the acquisition time of the 3D SASHA sequence is considerably longer than a breath-hold, a 1D dNAV was employed to enable 3D free-breathing T1 mapping (7).

2D and especially 3D T1 mapping techniques suffer from long acquisition times due to the need for acquiring several images along the inversion or saturation recovery curve. Different sampling schemes have been proposed for 2D MOLLI to reduce the number of heartbeats and thus shorten the length of the breath-hold, reducing the total number of heartbeats per breath-hold from 17 to 9 (31). Simultaneous multi-slice imaging techniques have been also investigated, both in free-breathing and in breath-hold, in order to accelerate the acquisition and to increase the volume coverage (8,35). Undersampling reconstruction techniques have been also investigated to accelerate the acquisition and improve the image resolution of the T1 maps (83–85).

This study proposes to accelerate the 3D SASHA acquisition by reducing the number of the T1-weighted images acquired along the saturation recovery curve. To maintain high accuracy and precision with fewer saturation points, we sought to investigate the merits of a novel 3D denoising technique applied directly to the T1-weighted images prior to T1 fitting, as described in chapter 7 in more detail. 2D denoising techniques based on tissue similarity distance (15) and based on Beltrami regularization (16) have been recently proposed to reduce the sensitivity to noise and improve the precision of 2D breath-hold myocardial T1 mapping sequences. Here the technique in (16) has been extended to enable accurate and precise 3D SASHA T1 mapping from fewer saturation points and thus shorter scan times. The proposed method was tested on a standardized T1 phantom,

10 healthy subjects with retrospectively reduced number of T1-weighted images and 10 healthy subjects with prospectively varied number of T1-weighted images.

8.2 Methods

8.2.1 Imaging sequence

The 2D SASHA T1 mapping sequence acquires eleven T1-weighted images at different saturation points (6). The original 3D SASHA T1 mapping sequence previously proposed in (10) acquires and fits nine T1-weighted images along the T1 recovery curve. In this study, for the 3D SASHA sequence the number of images acquired along the saturation recovery curve was varied between three and nine to investigate the effect of this reduction on the accuracy and precision of the T1 maps. Figure 8.1 shows the distribution of three and five time points along the T1 recovery curve used in this study. A time point without any saturation preparation was acquired at the beginning of the acquisition, which corresponds to a measurement of the fully recovered magnetization. The saturation time

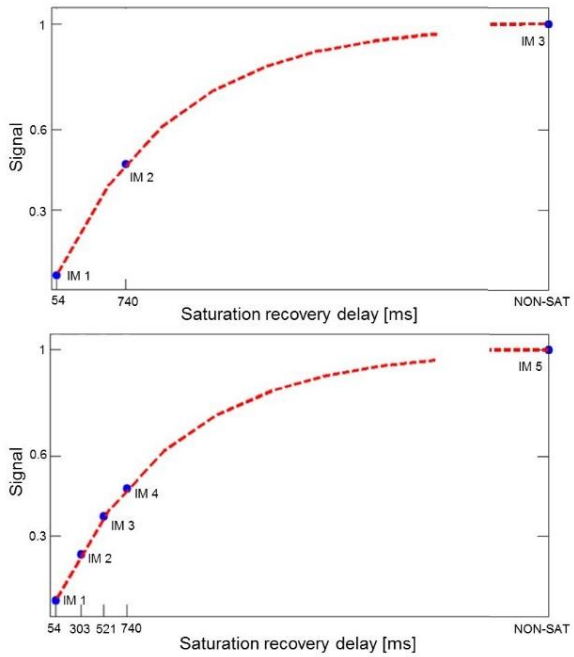

Figure 8.1: Distribution of three and five time points along the T1 recovery curve.

points were then acquired in order to be equally distributed between the minimum and the maximum saturation time (54 ms and 740 ms in Figure 8.1, for a heart rate of 60 bpm), following the original implementation of the 2D SASHA (6) imaging sequence.

8.2.2 3D Denoising

A reduced number of T1-weighted images is expected to decrease the precision of the corresponding T1 maps. In order to achieve high precision in spite of the reduced number of saturation recovery time points acquired, the 3D Beltrami denoising technique presented in chapter 7 is applied directly to the T1-weighted images prior to the T1 fitting. The 3D Beltrami regularization, expressed in [22], allows to preserve the edges, while reducing the noise of the images without introducing staircasing artefacts (78).

For all experiments the regularization parameter λ was set to 0.25, while the smoothing parameter h was set to 5. These parameters were empirically optimized to provide best image quality. A weight of 1.0 was employed for the Beltrami constant as indicated in (61).

8.2.3 Experiments

The proposed approach was evaluated in a standardized phantom with different T1 and T2 values and 20 healthy subjects. All imaging studies were performed on a 1.5T MR scanner (Ingenia, Philips, Best, The Netherlands). The study was performed in accordance with the Declaration of Helsinki (2000). All subjects recruited to this study provided written informed consent with study approval from the Institutional Review Board (1/11/12).

8.2.4 Phantom study

A standardized T1 phantom with nine agar/NiCl2 vials was used for imaging, with T1 values in the range of 250 to 1500 ms (67). The phantom was imaged using the original

3D SASHA sequence, with nine images acquired at different saturation points (54-650 ms). The number of T1-weighted images considered to generate the final 3D SASHA T1 map was reduced retrospectively from three to nine (step size of one). For each case T1 maps were obtained using a three parameter-fitting model before and after 3D denoising. An inversion recovery spin-echo sequence was used as reference method for the T1 values of the vials. The acquisition parameters used for the 3D SASHA sequence were: FOV = 300 x 300 mm^2, image resolution = 1.4 x 1.4 mm^2, slice thickness = 8 mm, flip angle = 35˚, TR/TE = 3.3/1.6. Sequence parameters for the spin-echo sequence were: FOV = 200 x 200 mm, image resolution = 3.1 x 3.1 mm^2, 10 mm slice thickness, TR = 8000 ms and TE = 5.9 ms. The phantom was acquired with a simulated heart rate of 60 bpm and using a combination of the 12-channel posterior and 16-channel anterior torso coils.

8.2.5 Healthy subjects study

The effect of reducing the number of T1-weighted images acquired along the recovery curve was studied in healthy subjects retrospectively and prospectively. For the retrospective study, data was collected in 10 healthy subjects using the original 3D SASHA sequence with nine images acquired at different saturation points. The number of T1-weighted images considered to generate the 3D SASHA T1 map was modified retrospectively from three to nine (step size of one) and mapping was performed before and after denoising. In addition, for the prospective study data was acquired in 10 additional healthy subjects using the 3D SASHA sequence with three, five and nine T1-weighted images along the recovery curve. The acquisition parameters used for the 3D SASHA sequence (both retrospective and prospective studies) were: FOV = 300 x 300 mm, image resolution = 1.4 x 1.4 mm^2, slice thickness = 8 mm, flip angle = 35˚, TR/TE = 3.3/1.6, subject specific mid-diastolic trigger delay, short-axis orientation, and 28-channel coil. 1D diaphragmatic navigator gating and tracking was used for respiratory

motion compensation with an end-expiratory 5 mm gating window. For both prospective and retrospective studies the 3D SASHA T1 map with nine images along the recovery curve, with saturation times varying between the subjects, was considered as the reference standard. 3D SASHA with nine images along the recovery curve has been previously compared against 2D SASHA showing excellent agreement in terms of accuracy (11).

8.2.6 Image analysis

3D denoising and three-parameter fitting were performed offline using MATLAB (MathWorks, Natick, MA). A myocardial T1 map was obtained for each acquisition, using different number of T1-weighted images, both before and after applying the 3D denoising method. A ROI was manually drawn in the septum of the myocardium for the mid slice T1 map in all the subjects. Mean and standard deviation in the selected ROI were calculated and used as a measurement of accuracy and precision of the T1 map. The measurements were compared using a Kruskal-Wallis test to identify if there was any significant difference between acquisitions with different numbers of T1-weighted images and between corresponding non-denoised and denoised T1 maps. For statistical analysis, GraphPad Prism v5 for Windows (GraphPad Software, La Jolla, CA) was used with a threshold of $P < 0.05$ to define the statistical significance. A Bland-Altman plot was calculated in order to compare the accuracy and the precision of the 3D SASHA non-denoised vs. 3D SASHA denoised, both for the retrospective and prospective study. In addition, for the prospective study, an AHA segmentation (62) was calculated to compare the accuracy and precision in the different myocardial segments of the whole-heart 3D SASHA for different number of saturation time points before and after denoising. This segmentation enables the analysis of the spatial homogeneity of the accuracy and precision for different number of saturation time points before and after denoising. Three

slices (apex, mid and base) and 16 segments were used to represent the cardiac volume, while the 17th segment represented the blood pool.

8.3 Results

8.3.1 Phantom study

Accuracy and precision measured in three phantom vials are shown in Figure 8.2, with T1 values similar to that of healthy native myocardium (vial #2), post-contrast myocardium (vial #4) and native blood (vial #6), and for different numbers of T1-weighted images in comparison to the gold standard spin echo values, indicated for each vial in Figure 8.2. No significant difference was found in terms of accuracy and precision for the different number of T1-weighted images before and after denoising (respectively $P = 0.99$ and $P = 0.98$) (Figure 8.2). However, an improvement in precision of about 36% in average was observed after denoising for all the number of T1-weighetd images considered. The nominal scan time for the original 3D SASHA sequence (nine images

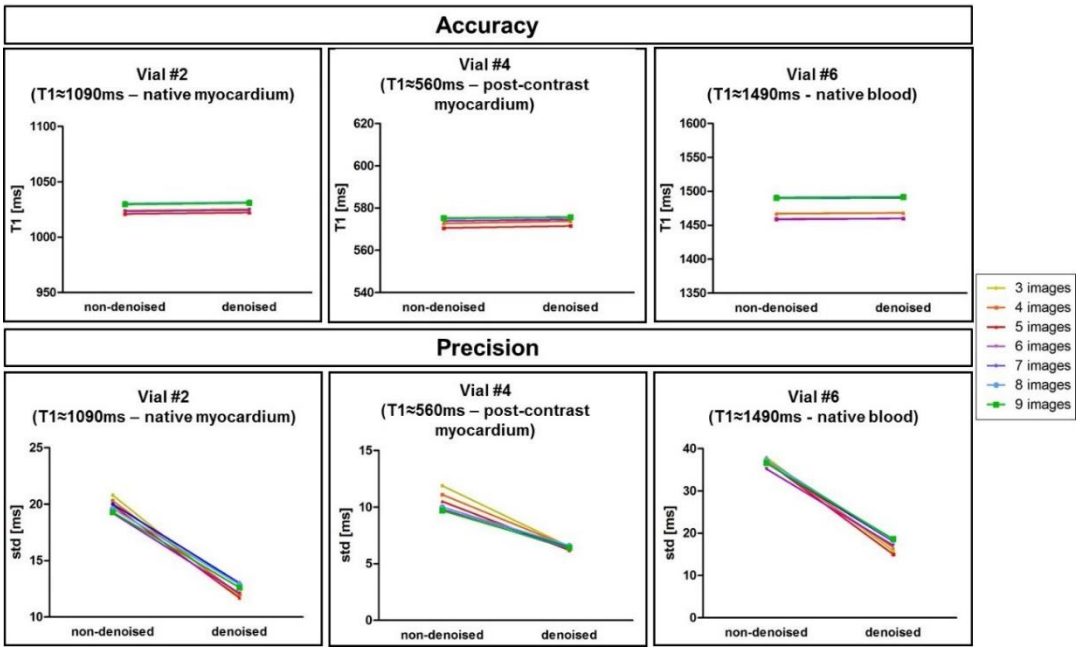

Figure 8.2: Accuracy and precision of three representative vials of the T1 phantom, measured before and after 3D denoising. The number of T1-weighted images considered to generate the T1 maps was modified retrospectively from three to nine (step size of one), indicated by the different colours.

acquired along the recovery curve) was 4:14 minutes:seconds while would have taken only 1:25 minutes:seconds with three images.

8.3.2 Healthy subject study

Healthy subjects study

Retrospective study: The accuracy and precision averaged over all ten healthy subjects for the retrospective study (three to nine images considered for mapping) both before and after denoising is shown in Figure 8.3. There was no statistical significant difference between the accuracy measured on the T1 maps reconstructed with three compared to nine T1-weighted images, both before and after denoising (respectively $P = 0.48$ and $P = 0.14$). There was a statistical difference ($P < 0.05$) between the precision measured on the

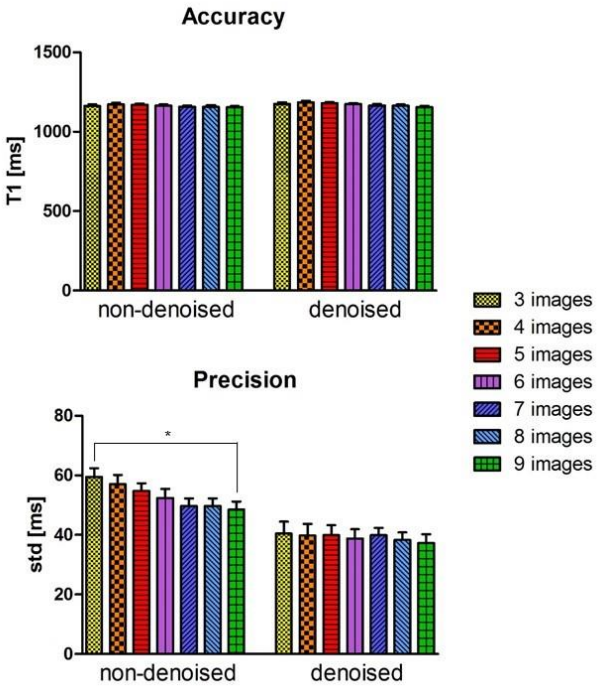

Figure 8.3: Accuracy and precision averaged between the ten healthy subjects for the retrospective study (3 to 9 images considered for T1 mapping). A ROI was manually drawn in the septum of the myocardium in the mid slice of the 3D SASHA T1 maps before (non-denoised) and after (denoised) denoising. Statistical significance difference is indicated by * (p value 0.045).

T1 maps reconstructed with three and nine T1-weighted images before denoising, while there was no statistical difference after denoising ($P = 0.99$).

There was no statistical difference between the precision measured on the T1 maps reconstructed with four to nine T1-weighted images, both before and after denoising ($P = 0.99$).

The Figure 8.4 shows the Bland-Altman plot of the accuracy and precision of the 3D SASHA non-denoised vs. 3D SASHA denoised T1 maps obtained using from three to nine T1-weighted images. The bias indicated in the plot show that there was a slight improvement both in terms of accuracy and precision after 3D denoising when an increased number of T1-weighted images were used.

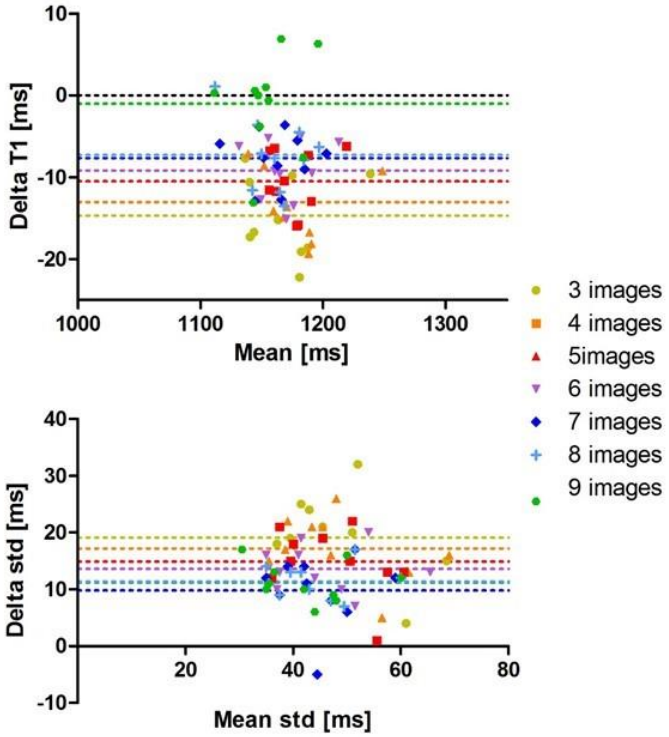

Figure 8.4: Bland-Altman plot of the accuracy (Delta T1) and precision (Delta std) of the non-denoised vs denoised 3D SASHA using from three to nine T1-weighted images for imaging, indicated with different colors in the figure. The bias of each measurement is also indicated in the plot.

3D SASHA T1 maps of two representative healthy subjects, obtained using a different number of saturation time points (respectively three, four, five and nine points) before and after denoising are shown in Figure 8.5. The 3D denoising technique permits to

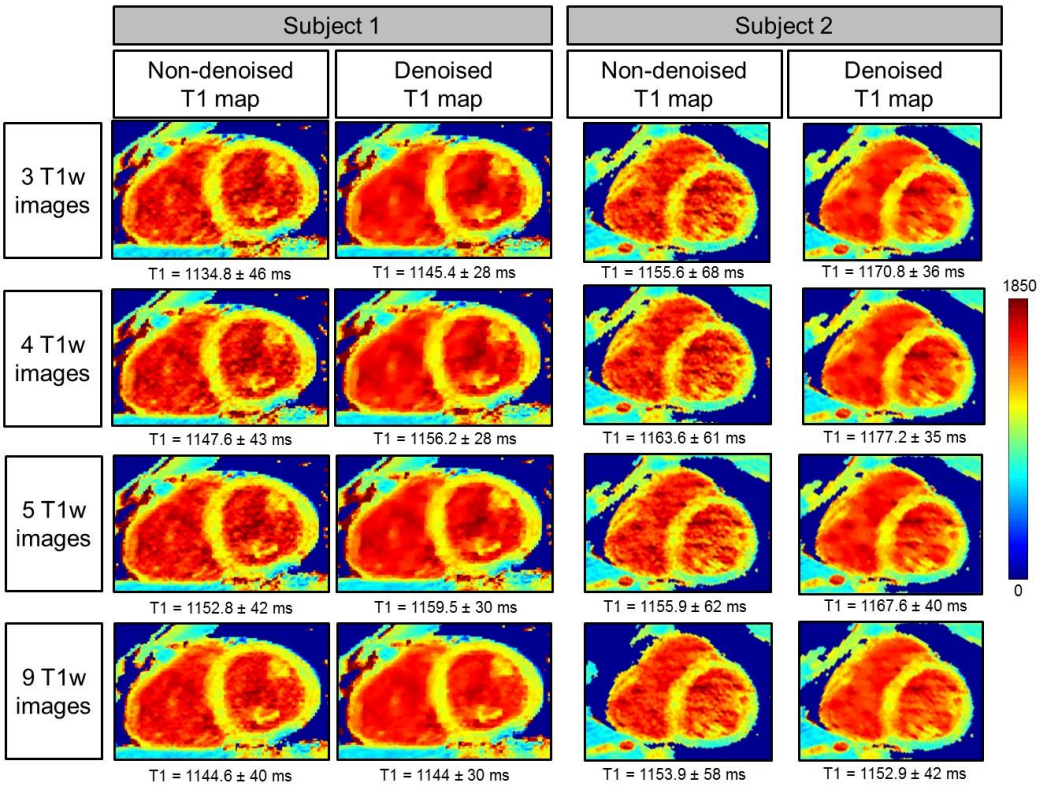

Figure 8.5: Myocardial 3D SASHA T1 maps of two representative healthy subjects before and after 3D denoising, with the accuracy and precision measured on the corresponding myocardial septum. The T1 maps were retrospectively reconstructed by using respectively three, four, five and nine saturation time points along the recovery curve.

recover the loss in precision due to the lower number of images along the recovery curve and to achieve comparable image quality between the T1 maps reconstructed with a different number of T1-weighted images.

Prospective study: The accuracy and precision averaged over all ten healthy subjects for the prospective study (three, five and nine T1-weighted images considered for mapping) both before and after denoising is shown in Figure 8.6a. There was no statistical difference between the accuracy measured on the T1 maps reconstructed using different number of T1-weighted images, both before (P = 0.73) and after (P = 0.64) denoising.

There was a statistical difference ($P < 0.05$) between the precision measured on the T1 map acquired with three and nine T1-weighted images before denoising. After applying the 3D denoising technique, the precision was recovered with no statistical difference ($P = 0.27$) when three or nine images where used for T1 mapping. However, if five images were acquired instead of three, the precision improved by about 12%. The average scan time for the original 3D SASHA sequence (nine images along the recovery curve) was 12 minutes. Scan time was reduced to 7:05 and 5:06 minutes:seconds when respectively 5 and 3 images were acquired. Figure 8.6b shows the Bland-Altman plots of the accuracy and precision of the 3D SASHA non-denoised vs. denoised for the three different acquisitions using three, five and nine T1-weighted images. The difference in terms of accuracy between non-denoised and denoised 3D SASHA is smaller when five and nine

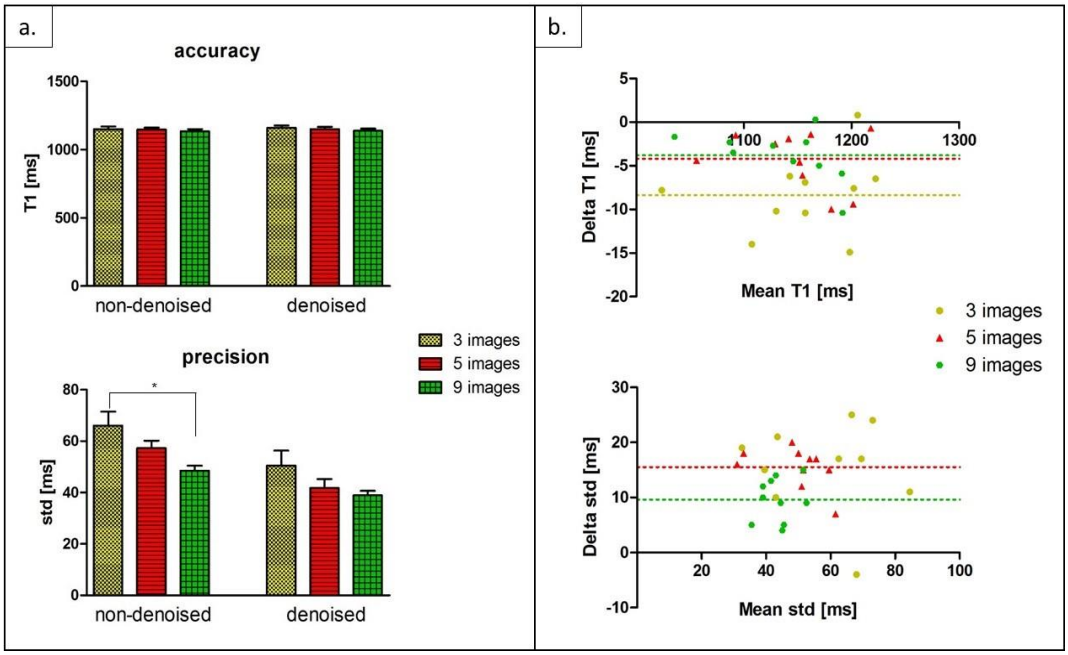

Figure 8.6: a) Accuracy and precision averaged between the ten healthy subjects, acquired prospectively with 3D SASHA using three (yellow bar), five (red bar) and nine (green bars) saturation time points along the recovery curve. The measurements were performed before (non-denoised) and after (denoised) denoising in the mid slice in the septum of the myocardium. Statistical significant difference is indicated by * (p value 0.034). b) Bland Altman plot comparing the accuracy (on top) and precision (on bottom) of the 3D SASHA non-denoised vs. 3D SASHA denoised using three-five and nine T1-weighted images. Bias are reported for each graph.

images are used. In terms of precision, the 3D denoising method has a major impact on the T1 maps acquired with three and five images.

The 3D denoising technique permitted to preserve image quality of the 3D SASHA T1 maps when five T1–weighted images were acquired, as shown in Figure 8.7 in two representative healthy subjects for the prospective acquisition. However, if only three T1-weighted images were acquired, the delineation of the myocardial borders and the papillary muscles was slightly degraded, as indicated with the white arrows. As the acquisition becomes longer with a higher number of saturation time points, it is also more prone to motion artefacts, as indicated by the blue arrows in the T1 maps for subject 1.

Figure 8.8 shows the AHA segmentation for the accuracy and precision measured on the 3D SASHA T1 maps acquired using three, five and nine T1-weighted images, reconstructed both before and after 3D denoising. The 3D denoising technique does not affect the accuracy of the 3D SASHA T1 maps for all the three different acquisitions (with three, five and nine T1-weighted images). The degree of heterogeneity in percentage are 9.5%, 9.8% and 14% for the denoised 3D SASHA using respectively three, five and nine T1-weighted images. The denoised 3D SASHA with three and five T1-weighted images have comparable degree of heterogeneity to the 2D MOLLI presented in Piechnik et al. (31), while with nine T1-weighted images the T1 variability is slightly

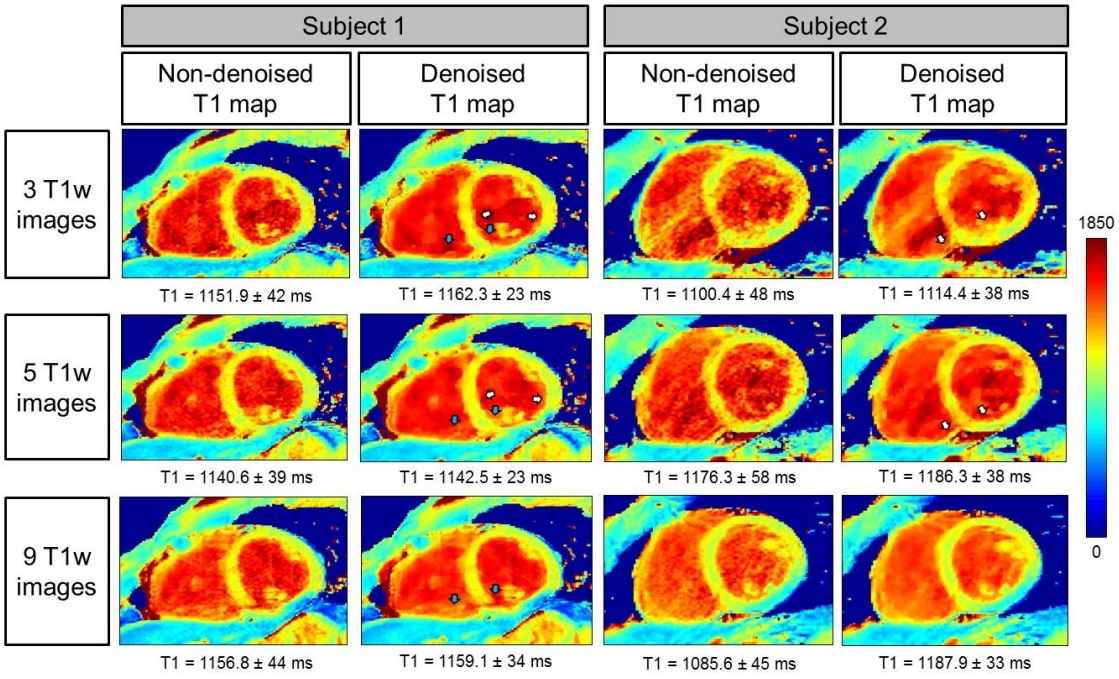

Figure 8.7: 3D SASHA T1 maps of two representative subjects acquired prospectively with three, five and nine T1-weighted images along the saturation recovery curve. The accuracy and precision measured in the myocardial septum are indicated for each T1 map. T1 maps were reconstructed before and after 3D denoising. There was an improvement in the image quality in terms of myocardial and pupillary muscles delineation after 3D denoising (white arrows). Motion artefact (blue arrows) can be introduced if more images are acquired due to the longer scan time.

higher. Instead the precision considerably improves after denoising across the whole left ventricle, particularly when three and five images are acquired.

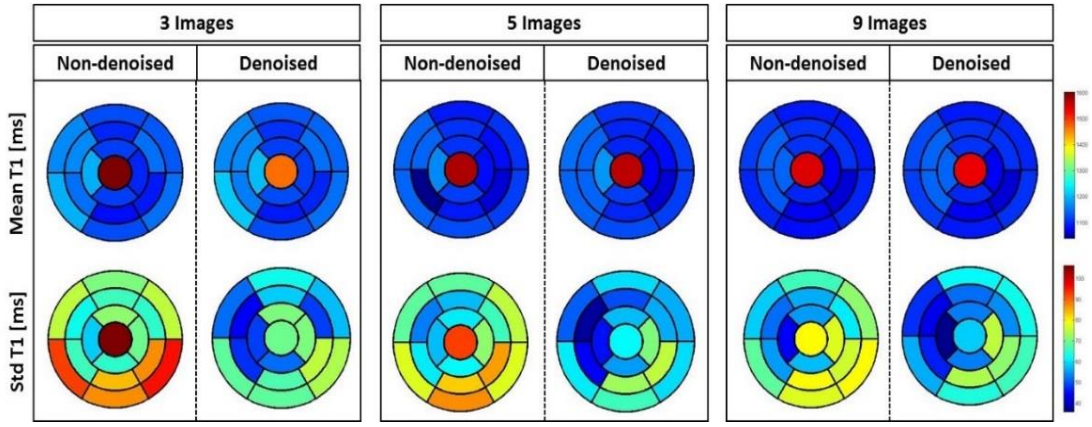

Figure 8.8: AHA plots for the accuracy (mean) and precision (standard deviation) of the 3D SASHA T1 maps from the ten healthy subjects of the prospective study. The T1 maps were acquired using three, five and nine T1-weighted images and they were obtained both before and after denoising. The accuracy is not affected after denoising, acquiring either 3, 5 or 9 images. Instead the precision improves after denoising for all the three different cases.

8.4 Discussion

This study proposes to accelerate the 3D SASHA myocardial T1 mapping technique by reducing the number of saturation time point images acquired along the recovery curve. Our retrospective experiments in a standardized phantom and healthy subjects demonstrate that reducing the number of T1-weighted images used for the T1 fitting has very little impact on the accuracy of the T1 maps. However, it has a direct impact on image quality and precision of the T1 maps. To recover the loss in precision and image quality of the myocardial T1 maps when a reduced number of T1-weighted images is acquired, a novel 3D denoising technique is employed. The proposed approach was validated prospectively in healthy subjects.

The phantom and healthy subjects' retrospective experiments demonstrated that the accuracy of 3D SASHA T1 mapping was not affected if the number of T1-weighted

images considered for T1 mapping was reduced to three images. Moreover, the accuracy was not affected by the application of the 3D denoising technique. Conversely, the precision was reduced when a smaller number of T1-weighted images was employed, with a statistical difference between using three and nine images. No statistical difference was observed in precision after denoising when the number of T1-weighted images was reduced from nine to three. Image quality was affected by the number of time point images used for mapping, which was improved after applying the proposed 3D denoising technique.

For the prospective experiments in healthy subjects, the 3D SASHA was acquired using three, five and nine T1-weighted images along the recovery curve. These experiments confirmed the results obtained from the retrospective study: the accuracy of the T1 maps was not affected by the different number of T1-weighted images acquired nor with the application of the 3D denoising technique. There was a statistical difference in precision between the T1 maps acquired with three and nine images before denoising. However, no statistical difference was observed after denoising. The AHA segmentation provided a 3D visualization of the accuracy and precision across the whole left ventricle, both before and after 3D denoising. The segmentation confirmed that the accuracy is maintained almost constant despite the smaller number of T1-weighted images acquired and the use of the 3D denoising technique, with T1 variability comparable to the 2D MOLLI data previously published in literature (31) when the 3D SASHA data are acquired with three and five T1-weighted images. Instead, the denoised 3D SASHA data acquired with nine T1-weighted images showed higher T1 variability within the left ventricle. In contrast the precision decreased when a reduced number of acquired T1-weighted images was used for T1 mapping. However, precision improved considerably after denoising. In spite of not being significantly different, the precision of the T1 map obtained from five T1-

weighted images before denoising was about 12% higher than that of the T1 map reconstructed using three images. In terms of image quality the delineation of the myocardial borders was in general worst in the T1 maps reconstructed from three images in comparison to the corresponding T1 maps reconstructed from five images (Figure 8.7). Some motion related artefacts were observed in the acquisitions with five and nine images consistent with the longer required scan times. In general a better compromised between image quality and motion related artefacts is observed when the T1 map is reconstructed using five images.

The scan time was considerably reduced with the proposed approach by acquiring a smaller number of T1-weighted images. However, it was still dependent on the efficiency of the diaphragmatic navigator and its unpredictable scan time, which can severely drop in patients with irregular breathing patterns. Alternative motion compensation techniques, such as image-based navigation and self-navigation (38,48,86), will be investigated in future studies to achieve 100% respiratory scan efficiency and consequently to further accelerate the scan, which can provide more comfort to the patient and reduce the risk of introducing additional bulk motion artifacts associated with long scans.

The saturation time points were selected along the T1 recovery curve in order to provide an equal distribution between the shortest and the longest saturation time, following the original implementation of the 2D SASHA (6) imaging sequence. Further investigation is warranted to understand the effect of a different selection of the sampling points in terms of accuracy and precision of the T1 map (87).

The 3D Beltrami denoising technique employed in this study permits to considerably improve image quality and the precision of the 3D SASHA T1 maps, independently of the number of T1-weighted images acquired (ranging from nine to three). The denoising

is a post-processing step and is directly applied to the T1-weighted images. Future studies will investigate the integration of the denoising technique as regularization directly in the reconstruction process to further accelerate the scan.

Only native 3D SASHA T1 mapping was performed in this study. Further studies will investigate the acquisition of accelerated native and post-contrast 3D SASHA myocardial T1 maps in patients with cardiovascular disease to enable the measurement of extracellular volume fraction, which has been demonstrated to be useful to detect diffuse myocardial fibrosis (23). For further validation of the proposed approach, clinical studies would need to be conducted as future work.

8.5 Conclusions

In conclusion, this study demonstrates the feasibility of accelerating free-breathing 3D SASHA T1 mapping by acquiring fewer (three to five) saturation time point images along the recovery curve. This was achieved by using a 3D denoising method to maintain the high precision of the T1 maps and ensure adequate image quality. The proposed technique permits to acquire a whole-heart high-resolution T1 map in approximately 7 minutes, achieving both high accuracy and precision.

Chapter 9 - Whole-heart T1 mapping using a 2D fat image navigator for respiratory motion compensation

The main idea of the study has been conceived and designed by Dr Markus Henningsson, Professor René Botnar and Giovanna Nordio (GN). GN implemented the imaging sequence, acquired, reconstructed and analysed the data. Dr Torben Schneider supported the implementation of the imaging sequence. Dr Gastao Cruz and Dr Teresa Correia helped with the image reconstruction. Dr Aurelien Bustin implemented the denoising algorithm.

The manuscript was written and reviewed by all authors and it was submitted to the *Magnetic Resonance in Medicine* journal.

This study was presented by GN at the 25th Scientific Meeting of the International Society for Magnetic Resonance in Medicine meeting in Honolulu, Hawaii USA 2017, and at the 26th Scientific Meeting of the International Society for Magnetic Resonance in Medicine meeting in Paris, France 2018.

9.1 Introduction

Several different imaging techniques have been devised and validated for myocardial T1 mapping, using inversion recovery (5), saturation recovery (6) or a combination of both (7) to perturb the longitudinal magnetization. As described in Chapter 3, MOLLI (5) is an inversion-recovery based technique, which is characterized by high T1 precision, although it tends to underestimate the T1 values. An alternative solution has been proposed, which is the SASHA sequence (6), that uses saturation recovery pulses and is characterized by higher accuracy but lower precision compared to MOLLI. Both these T1 mapping sequences have been implemented as single shot 2D imaging techniques and only one single slice is acquired per breath-hold. For high-resolution T1 mapping, a free-breathing, whole-heart 3D quantitative T1 mapping technique would be preferable, since it would allow complete volumetric coverage of the heart with potentially higher image resolution, allowing visualization of small myocardial structures and pathologies. A 3D SASHA (10) imaging sequence has been recently proposed, which allows to image the whole-heart in free-breathing. This technique shows similar T1 accuracy to 2D SASHA, but with improved precision. In the approach described in (10), a 1D dNAV with gating and tracking was acquired just prior to imaging to compensate for respiratory motion. Other techniques have been proposed for free-breathing pre-contrast and post-contrast myocardial T1 mapping to assess diffuse fibrosis after contrast administration, which use the 1D dNAV to minimize the respiratory motion (35,36,88). Although 1D dNAV gating and tracking enables respiratory motion compensation for the T1-weighted images, it has some limitations. The motion is estimated from the foot-head displacement of the lung-liver interface instead from the heart itself and thus requires a motion model. In addition, the scan efficiency of the 1D dNAV is typically 40-50% in healthy subjects, but can be considerably lower in patients with irregular breathing patterns. This prolonged and

unpredictable scan time limits the applicability of this technique in very sick patients and precludes achieving the high spatial resolution necessary to visualize small focal fibrosis. Self-navigation (48) and image-based navigator (45) techniques have been recently proposed to estimate directly the respiratory-induced motion of the heart and correct for it, enabling 100% respiratory scan efficiency and thus shorter and predictable scan times. iNAV techniques have been used for coronary artery MRI and shown good motion estimation and correction performance (38,72,89,90). However, iNAVs have not yet been extended to parametric 3D T1 mapping due to the technical challenges of this technique which include: interference between the image navigator and the T1-weighted images that can affect the accuracy and precision of the T1 measurement, low SNR of the navigators due to the effect of saturation pulses and the long T1 of blood, and change of contrast of the navigators during the acquisition of different T1-weighted images.

This work proposes to address these challenges by combining the 3D SASHA imaging sequence with a fat-iNAV (49,91) in order to enable whole-heart translational motion-corrected 3D T1 mapping with high image resolution in a clinically acceptable and predictable scan time. With the fat-iNAV, epicardial fat is excited and the navigator images are used to directly estimate the respiratory motion of the heart, which has several theoretical advantages. Firstly, with this approach the fat excitation pulses should not affect the (diagnostic) water signal and thus not influence T1 quantification. Second, fat has a short T1 and therefore yields T1-weighted navigator images with relatively high signal even for short saturation delays while a water navigator would suffer from varying signal intensities for different saturation delays, potentially compromising image registration and motion estimation.

9.2 Materials and Methods

9.2.1 Fat-navigator acquisition and motion correction

Conventional image-based navigator techniques excite both water and fat signals to obtain low-resolution images of the heart at every heartbeat. Since fat magnetization recovers faster than that of water after the application of a saturation pulse, fat-selective navigator measures a more constant signal at different saturation delays in contrast to water selective navigators, and thus may improve motion estimation.

A schematic diagram of the framework used for image acquisition, motion estimation/correction using fat-iNAV and T1 map generation are shown in Figure 9.1.

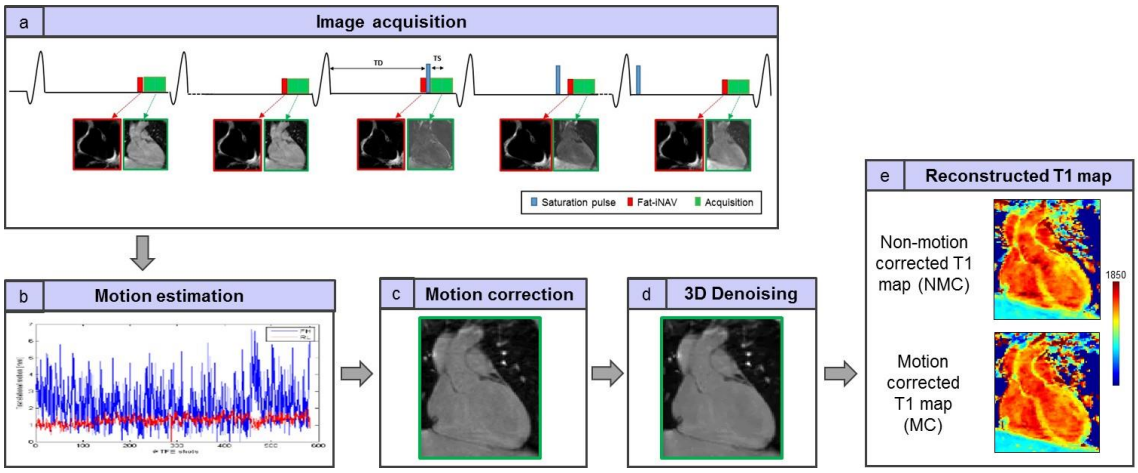

Figure 9.1: Framework of the proposed approach. a) The 3D SASHA imaging sequence was combined with fat-iNAVs for respiratory motion compensation. b-c) 2D translational motion correction was applied on the T1-weighted images. d) Prior to T1 fitting, the images were denoised using the 3D denoising algorithm proposed in (61). e) T1 maps were reconstructed before and after motion correction.

Data were acquired using the 3D SASHA imaging sequence described in (10). A segmented 3D k-space acquisition was used: first, all image k-space segments with no magnetization preparation were acquired, also called infinity images, and assumed to be acquired at an infinite saturation delay. Three "pause" cardiac cycles were added between the acquisitions of these k-space segments to ensure full recovery of the magnetization. Subsequently, an interleaved segmented acquisition was performed with preceding

saturation pulse and increasing saturation delays. A 2D fat-iNAV was acquired immediately prior to the T1-weighted image acquisition in mid-diastole. 2D foot-head and right-left displacements were estimated by selecting a region of interest (ROI) around the heart in the fat-iNAV images. An iNAV at end-expiration was chosen as reference frame and then translational motion was estimated between the reference and any subsequent iNAV using a normalized cross-correlation registration algorithm. The spatial shift calculated in the image domain from the fat-iNAVs images (equation 11) was used to correct the k-space of each T1-weighted image using the phase shift property of the Fourier transform (equation 12). SENSE Cartesian reconstruction was then used to recover the motion corrected T1-weighted images.

The acquisition parameters used for the fat-iNAV acquisition were: 3 x 3 mm^2 in plane image resolution, FOV = 300 x 300 mm^2, slice thickness 20 mm, 15˚ flip angle, TR/TE = 1.5 ms/7.2 ms, fate selective = 1331 binomial pulse (92), SENSE factor of 2, linear profile order, Cartesian fast echo planar imaging acquisition with 5 excitations and an EPI factor of 9, resulting in a temporal resolution of 73 ms. Translational motion correction and T1 mapping reconstruction were performed offline using MATLAB (MathWorks, Natick, MA). SENSE Cartesian reconstruction was performed for both non-motion corrected and motion corrected 3D SASHA datasets. A denoising method was applied to the T1-weighted images of both the 2D and 3D SASHA acquisitions before parametric fitting in order to reduce the noise and improve both image quality and T1 precision of the T1 maps (11,61). A three-parameter fitting model was then used to reconstruct offline the T1 maps respectively for the two datasets, with a pixel-wise fitting approach.

9.2.2 Phantom experiment

A phantom with nine agar/$NiCl_2$ vials was scanned using the proposed fat-iNAV T1 mapping approach with T1 values ranging from 250 ms to 1500 ms (67). The T1 phantom

data was acquired with an inversion recovery spin-echo (IRSE) acquisition, providing reference T1 values, and the 2D and 3D SASHA imaging sequences with fat-iNAV for comparison purposes. Sequence parameters for IRSE were: FOV = 150 x 150 mm^2, spatial resolution 1.95 x 1.95 mm^2, 10 mm slice thickness, repetition time (TR) between inversion pulses = 7000 ms, TE = 6 ms, 20 inversion times varying from 50-5000 ms. The imaging parameters for the 2D SASHA sequence were: FOV = 300 x 280 mm^2, spatial resolution 1.7 x 2.1 x 10 mm^3, flip angle = 70˚, TR/TE = 2.4 ms/1.2 ms, SENSE factor of 2. The imaging parameters for the 3D SASHA technique were: FOV = 300 x 300 mm^2, spatial resolution 2 x 2 x 4 mm^3, reconstructed image resolution 2 x 2 x 2 mm^3, flip angle = 35˚, TR/TE = 3.2 ms/1.6 ms, SENSE factor of 2, balanced steady-state free precession (bSSFP) acquisition, Cartesian trajectory with radial k-space shutter, low-high profile order and coronal view. For the 3D SASHA, a total of eight images were acquired and three pause heart cycles were performed between the acquisitions of k-space segments of the infinity image.

To investigate potential interference between the fat-iNAV and 3D SASHA acquisition, two different slices of the 3D SASHA acquisition were analysed, one in the same slice location as the fat-iNAV (slice with fat-iNAV) and one parallel to the iNAV at a more distal location (16 mm) (slice without fat-iNAV). T1 measurements were then obtained in the two slices and compared with the Bland-Altman analysis and the Spearman test for correlation.

To compare the navigator signal between the fat-iNAV and conventional non-spectrally selective navigator excitation, the T1 phantom and a phantom containing fat were scanned using the 3D SASHA imaging sequence with either of the two navigator acquisition approaches (38). The signal of the fat-iNAV was measured in the phantom containing fat, while the signal of the conventional navigator was measured in the vial of the T1 phantom

with a T1 value similar to that of blood. The 2D SASHA T1 values of the phantom were also compared with the T1 values acquired using the 3D SASHA imaging sequence with and without fat-iNAV.

9.2.3 In vivo experiments

The study was performed in accordance with the Declaration of Helsinki (2000). All subjects recruited in this study provided written informed consent with study approval from the Institutional Review Board (1/11/12). Ten healthy subjects (age = 31 ± 3 years, 6 male) were imaged on a 1.5T Ingenia Philips MR system (Philips Healthcare, Best, The Netherlands) with a 28-channel coil array and using the 3D SASHA imaging sequence with the fat-iNAV described in Figure 1. For comparison 2D SASHA was acquired during breath-hold in a mid-ventricular slice. The same imaging parameters used for the 3D SASHA and 2D SASHA imaging sequences for the phantom experiment were used for the in vivo study. The 2D SASHA imaging sequence was acquired in short axis view, while the 3D SASHA imaging sequence in coronal view.

For one of the subjects, the 3D SASHA acquisition was performed twice, both using the fat-iNAV and the conventional non-spectrally selective excitation navigator, to compare the respiratory motion of the heart estimated using the two different navigators. In both cases a normalized cross-correlation was used for motion estimation.

9.2.4 Image analysis

T1 maps were reconstructed using a three-parameter fitting approach, both before and after translational motion correction. For the phantom study, a ROI was manually drawn in the nine vials and the mean and standard deviation of the T1 measurements were measured as an estimate of the accuracy and the precision of the T1 map respectively. For statistical analysis, GraphPad Prism v5 for Windows (GraphPad Software, La Jolla, CA) was used. The T1 values measured in the phantom in the two different slices (with and

without fat-iNAV) were compared using a Bland-Altman plot and the correlation using a Spearman test. The T1 values measured in the phantom from the 3D SASHA acquisitions with and without the fat-iNAV were compared to the T1 values from the 2D SASHA sequence using a Bland-Altman plot. For the in vivo study, a ROI was manually drawn in the myocardial septum and the mean and the standard deviation of the T1 values were measured as an estimate of respectively the accuracy and precision. The in vivo dataset, acquired in coronal view, were reformatted in the short axis view to the same slice as 2D SASHA for comparison using Horos software v1.1.7. An AHA segmentation was used to compare the accuracy and precision of the 3D SASHA with fat-iNAV before and after motion correction and for 3D visualization of the left ventricle. The cardiac volume was represented in 16 segments for three slices (apex, mid and base), with the segment 17 corresponding to the blood pool. The value in each segment was averaged over the ten healthy subjects.

9.3 Results

9.3.1 Phantom experiment

Table 3 shows the mean and standard deviation measured on the nine vials of the T1 phantom using the IRSE, 2D SASHA and 3D SASHA imaging sequences. For the 3D SASHA sequence, the T1 values were measured in two different slices (slice with and without fat-iNAV). There was a good agreement between the IRSE and the 3D SASHA imaging sequence, for both slices.

Table 3: Mean and standard deviations measured in the nine vials of the T1 phantom using the inversion recovery spin-echo (IRSE), 2D SASHA and 3D SASHA for two different slices.

vials	IRSE [ms]	2D SASHA [ms]	3D SASHA (slice without fat-iNAV) [ms]	3D SASHA (slice with fat-iNAV) [ms]
1	428 ± 10	436 ± 6	446 ± 4	442 ± 4
2	559 ± 10	564 ± 9	585 ± 5	576 ± 3
3	309 ± 9	306 ± 7	308 ± 4	309 ± 4
4	1078 ± 24	1099 ± 20	1110 ± 28	1121 ± 17
5	1283 ± 24	1351 ± 22	1342 ± 25	1334 ± 31
6	792 ± 13	815 ± 9	801 ± 7	805 ± 8
7	456 ± 8	454 ± 5	461 ± 4	461 ± 4
8	1507 ± 34	1565 ± 28	1554 ± 20	1559 ± 27
9	254 ± 6	256 ± 4	256 ± 3	256 ± 3

The correlation between the T1 measurements on the two different 3D SASHA slices is shown in Figure 9.2, where a significant correlation ($r^2 = 0.99$, $P < 0.0001$) was found.

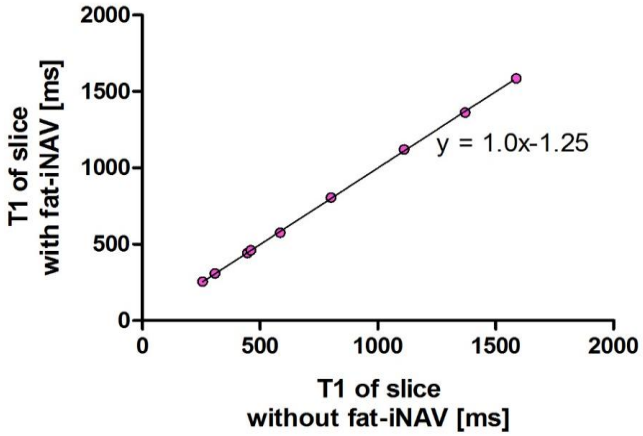

Figure 9.2: Correlation between the T1 values measured on the T1 phantom in the two different slices of the 3D SASHA acquisition, one corresponding to the fat-iNAV (slice with fat-iNAV) and one outside the area of excitation of the fat-iNAV (slice without fat-iNAV). The identity line is also indicated in the graph.

Figure 9.3 shows the Bland Altman plot comparing the T1 values measured in the two slices of the 3D SASHA acquisition. There is no bias between the two set of measurements, while the 95% limits of agreements are equal to 12.5ms.

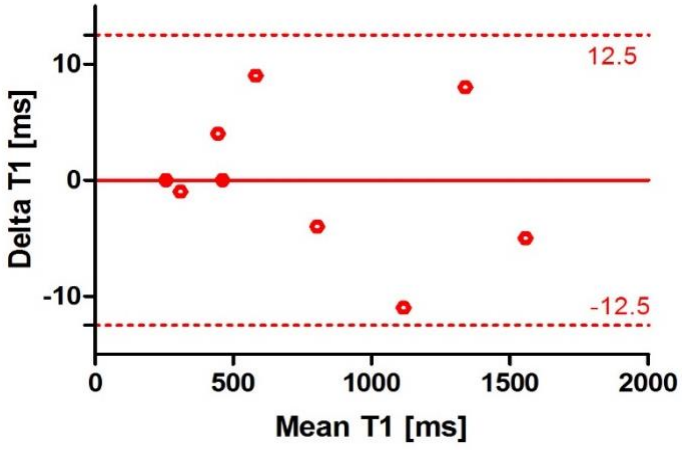

Figure 9.3: Bland-Altman plot comparing the 3D SASHA acquired on the two different slices (without and with fat-iNAV). The mean and the 95% limits of agreement are reported in the graph.

Figure 9.4 shows the signal of the fat (red) image navigator and the water (blue) image navigator (acquired with a non-spectrally selective excitation pulse), measured at

different saturation times. The signal for the fat-iNAVs is similar for all saturation times, while it increases significantly for the water image navigator with increasing saturation delay time and particularly for the infinity image water iNAV. Figure 9.5 shows the Bland-Altman plot comparing the T1 values measured on the 2D SASHA T1 map to the

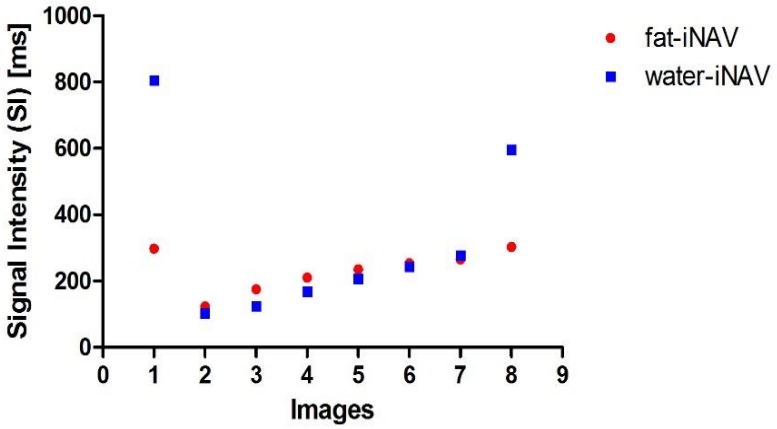

Figure 9.4: Comparison of the signal measured in the conventional (blue) and fat (red) image navigator, for each different T1 weighted images of theT1 phantom.

3D SASHA T1 map acquired with (red dot) and without (blue square) fat-iNAV. The fat-iNAV does not affect the estimation of the T1 values.

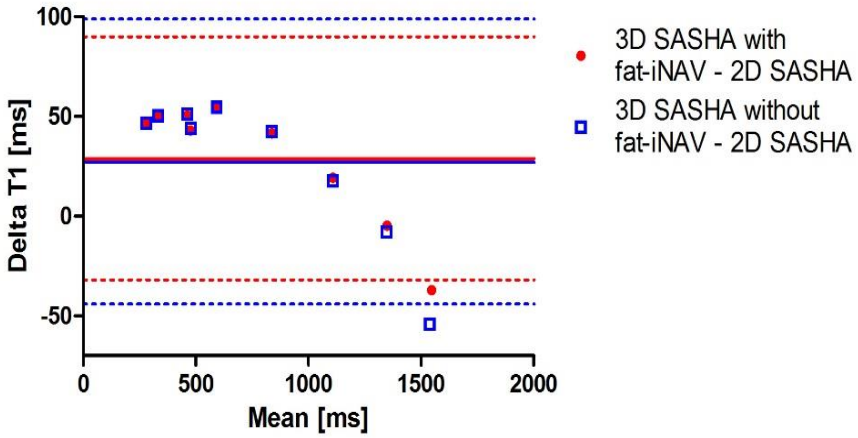

Figure 9.5: Bland-Altman plot comparing the T1 values measured on the 2D SASHA T1 map and the 3D SASGA T1 map with (red dot) and without (blue suare) fat-iNAV.

9.3.2 In vivo experiments

Figure 9.6 compares the translational motion estimated using a conventional non-spectrally selective excitation for the water image navigator (Figure 9.6a) and the fat-iNAV (Figure 9.6b) for one healthy subject. The change in contrast of the acquired 3D SASHA images with different T1-weighting are reflected in the navigators with non-spectrally selective excitation which causes a change in the trend of the translational motion estimated between the acquisition of the infinity images (green box) and the beginning of the acquisition of the saturated images (orange box). In addition, the change in contrast of the water image navigator makes it challenging to correct to a common reference iNAV used for the image registration, which causes errors in the motion estimation. Consequently, residual motion also affect the quality of the reconstructed T1 map, where the precision are lower compared to the T1 map reconstructed using the fat-iNAV, as shown in Figure 9.6.

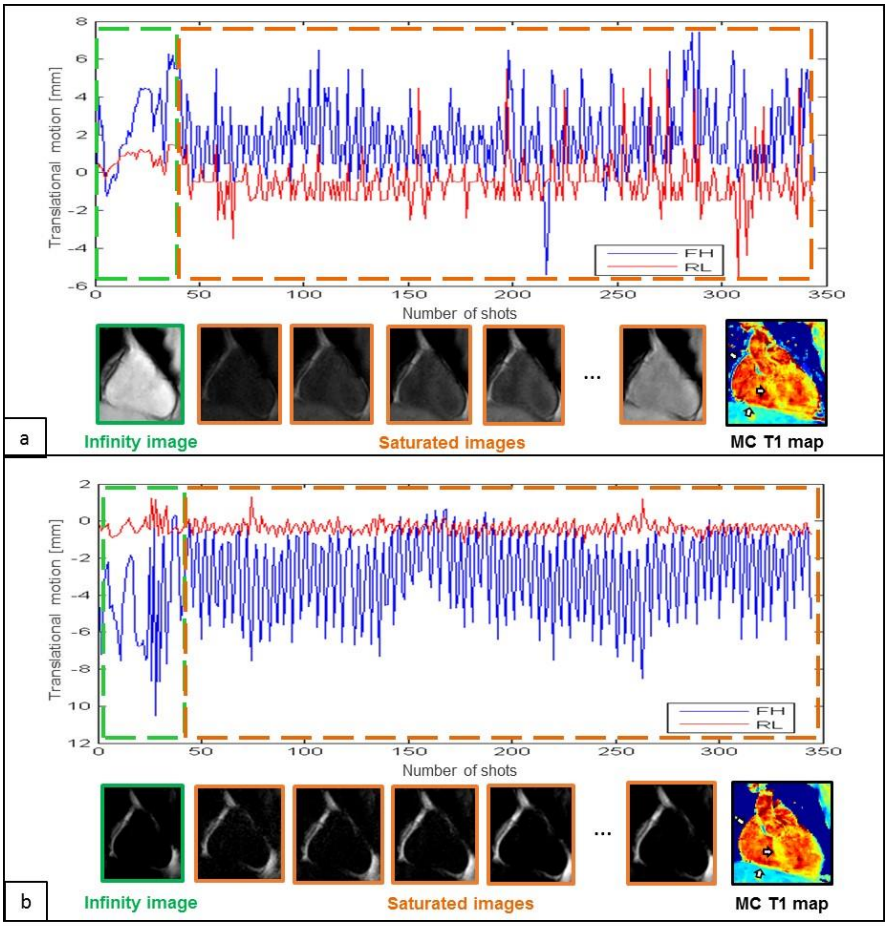

Figure 9.6: Foot-head (FH blue signal) and right-left displacement (RL red signal) of the heart measured with the conventional navigator (a) and the proposed fat-iNAV (b) for one representative subject. The corresponding image navigators of the non-saturated images (infinity image, green), and of the saturated images (orange) are shown below the displacements, together with the motion corrected (MC) 3D SASHA T1 maps respectively using the motion estimated from the water (a) and the fat (b) iNAVs.

Figure 9.7 shows the T1-weighted images and the 3D SASHA myocardial T1 map for one representative subject with no motion correction (NMC) and after 2D translational motion correction (MC). There was an improvement in the delineation of the myocardium and papillary muscle after motion correction, as indicated by the white arrows, both in the T1-weighted images and the T1 map. The corresponding fat-iNAVs are shown for the different saturation times with no visible change in image contrast. The isotropic reconstruction of 3D SASHA allows reformatting the dataset in arbitrary imaging planes.

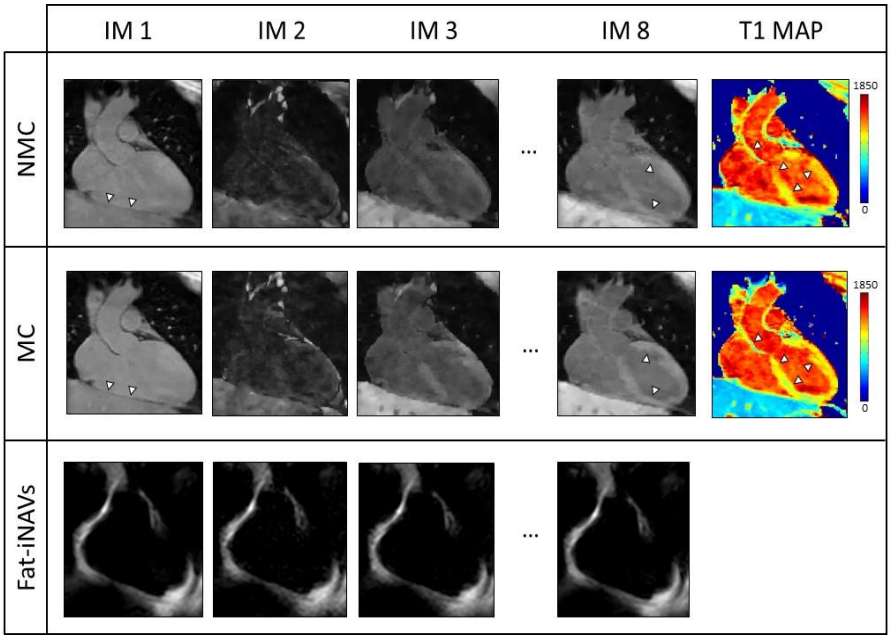

Figure 9.7: T1-weighted images and myocardial T1 map non-motion corrected (NMC) and motion corrected (MC) for one representative subject. In the bottom row the fat-iNAVs of the corresponding T1-weighted images are shown.

Figure 9.9 shows the reformat of the 3D SASHA T1 maps in short axis view for three representative subjects before and after respiratory motion correction, in comparison with the corresponding 2D SASHA T1 maps. After translational motion correction the delineation of the myocardial borders and the papillary muscles improves, as indicated in Figure 9.9. There is good agreement between the T1 measured in the septum of the myocardium between the 3D SASHA and 2D SASHA T1 maps, with an improvement in the precision for the 3D SASHA T1 map, due to the denoising method (61) and due to the higher SNR compared to the 2D SASHA. The precision of the 3D SASHA T1 maps further improves after translational motion correction as shown in Figure 9.8 for all the ten subjects. This is also confirmed by the AHA plot (Figure 9.9), which shows that the precision is improved for most segments after motion correction, with the exception of the inferior segments. This might be due to residual motion. The average total scan time for the 3D SASHA imaging sequence was of 7 minutes.

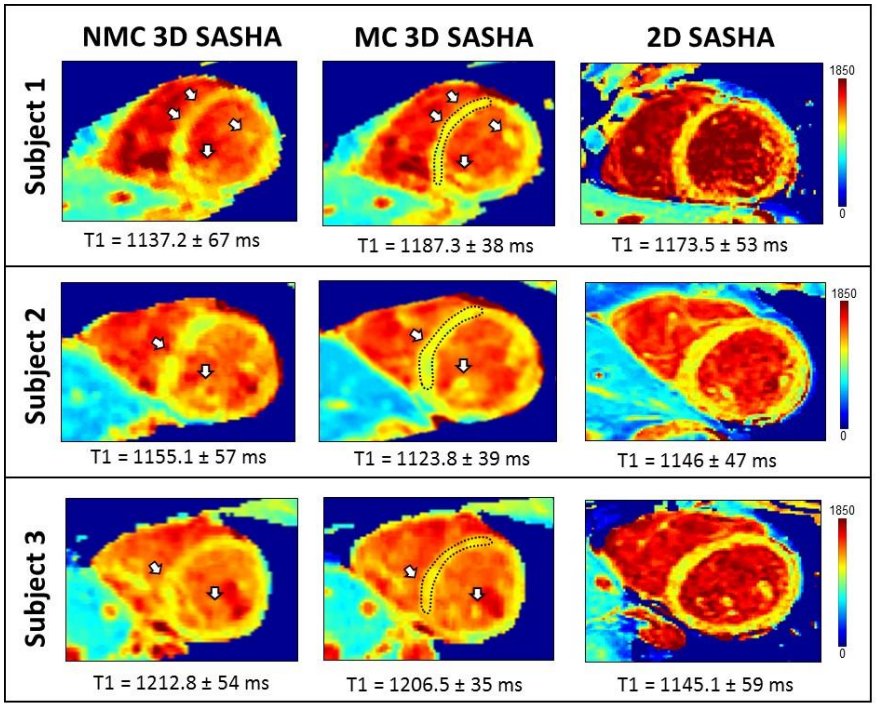

Figure 9.9: Short axis view of the myocardial T1 maps using the non-motion corrected (NMC) and motion corrected (MC) free-breathing fat-iNAV 3D SASHA and breath hold 2D SASHA imaging sequences for three representative subjects. Mean and standard deviations were measured in the myocardial septum (dotted ROI).

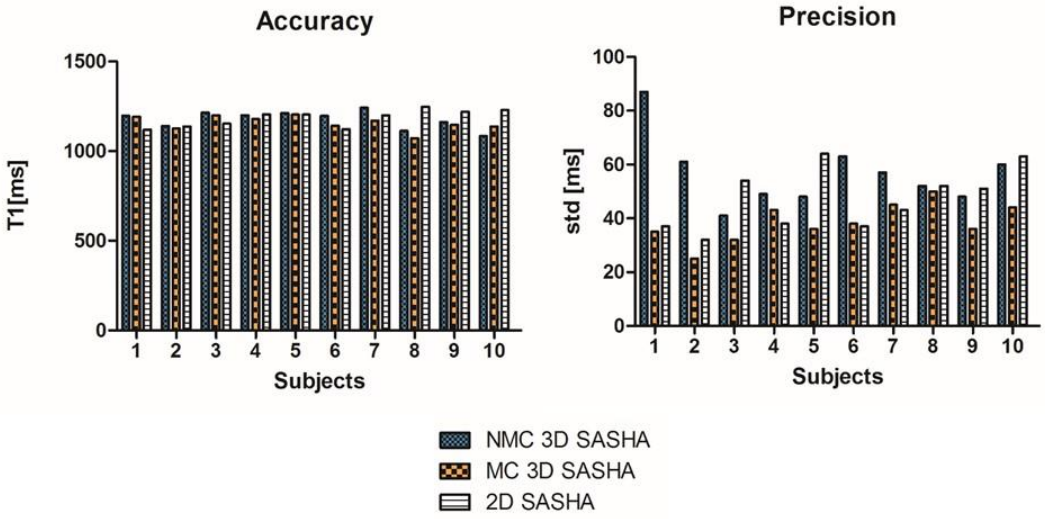

Figure 9.8: Accuracy and precision measured on the non-motion corrected (NMC, blue), motion corrected (MC, orange) 3D SASHA, and 2D SASHA (white) T1 maps for the ten healthy subjects. All the three techniques have been previously denoised. The T1 values were measured in the septum of the myocardium.

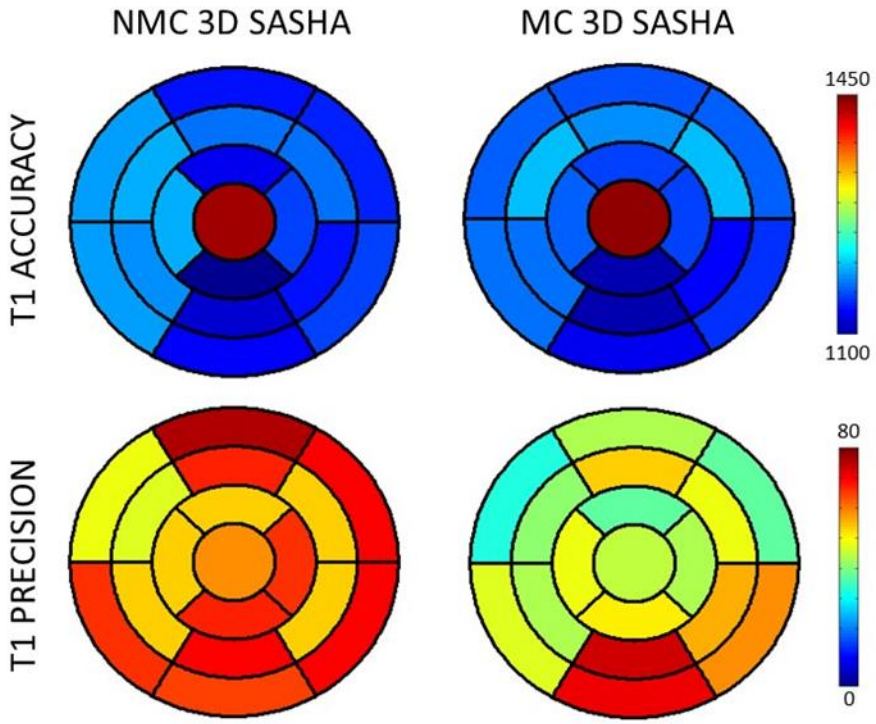

Figure 9.10: AHA plot of the left ventricle, shown for the non-motion corrected (NMC) and motion corrected (MC) 3D SASHA (n = 10 subjects). The cardiac volume is represented in 16 segments and three slices (apex, mid and base), while the center represents the blood pool. The precision improves after motion correction, although low precision was found in the inferior wall after motion correction due to residual motion artefacts.

9.4 Discussion

In this study, a new fat image-based navigator for free-breathing 3D myocardial T1 mapping is proposed. The fat-iNAV has been combined with the previously proposed 3D SASHA myocardial T1 mapping technique (10), enabling increased coverage, high spatial resolution, 100% respiratory scan efficiency and predictable scan time. Ideally, the fat-iNAV only excites signal from epicardial fat, without affecting the water signal of the 3D SASHA T1 mapping acquisition and does not introduce systematic bias of the T1 measurement. This has been demonstrated through the T1 phantom experiment, which shows good agreement between the T1 values measured in two different slices, one without fat-iNAV and one corresponding with the fat-iNAV (Figure 9.3).

In patients with significant amounts of epicardial fat, the image navigator will have more tissue from which to estimate respiratory motion, which may yield better respiratory motion correction. In the current work, fat suppression was used to minimize signal from subcutaneous and pericardial fat in the T1 maps, primarily to avoid motion artefacts (ghosting) arising from these tissues. Visualization of fat is of interest to detect fatty infiltration of the myocardium. Although fat-iNAV RF-pulses may cause saturation effects of the fat signal for the T1 maps, the use of low flip angles combined with few RF excitations and the short T1 of fat means that more than 85% of the longitudinal magnetization remains immediately after the fat-iNAV has been performed. Therefore, there is only a minor loss in fat signal-to-noise ratio in the regions where the fat-iNAV and T1 map overlap. An alternative solution could be a Dixon iNAV in concert with Dixon T1 mapping, which would provide fat-based motion tracking and allow to directly visualize fatty infiltration in the fat only images.

The signal of the fat-iNAVs is relatively constant between the acquisitions of the different saturation time points, as shown in Figure 9.4. This is also confirmed in vivo, where the contrast of the fat-iNAVs is visually maintained constant along the whole acquisition, due to a faster recovery of the fat signal after the saturation pulse compared to the water signal, ensuring a robust estimation of the respiratory motion of the heart (Figure 9.6). Non-spectrally selective excitation results in different contrast at different saturation times and this can affect the estimation of the respiratory motion, as shown in Figure 9.6a. The incorrect estimation of the translational motion using the water iNAVs has a direct impact on the motion-corrected T1 map, where residual motion affects the image quality and the delineation of the myocardium. In addition, the precision is lower on the T1 map motion-corrected using the water iNAVs compared to the T1 map motion-corrected using the fat-iNAVs.

After respiratory motion correction there is an improvement in the image quality of the T1 maps, with an improved delineation of the myocardial borders and papillary muscles and improved precision (Figure 9.7, Figure 9.9). However, only 2D translational motion correction has been used in this study, while a more advanced motion correction approach that also takes into account more complex motion, such as affine or non-rigid motion, may further improve the T1-weighted images and the T1 precision (52).

Compared to the original implementation of the 3D SASHA imaging technique, where a 1D diaphragmatic NAV was used for gating and tracking, the acquisition has been considerably accelerated using the fat-iNAV reducing the scan time to 7 minutes. Due to the reduced scan time, it was possible to achieve higher image resolution and to reconstruct the images with isotropic resolution, which permits to retrospectively reformat the images in an arbitrary plane. T1 values measured in the myocardial septum using the 3D SASHA technique are comparable to that of the 2D SASHA, with an improvement in the precision after respiratory motion correction (Figure 9.8). In fact, as previously shown (11), the 3D denoising approach permits to considerably improve the precision of the 3D SASHA imaging technique. In addition, the SNR of the 3D SASHA acquisition is higher than that of the 2D SASHA, and this contributes as well to the improvement of the precision of the T1 map. The precision of the 3D SASHA T1 maps further improves after translational motion correction, as indicated by the AHA plot in Figure 9.9. However, in the inferior regions the precision is still lower after motion correction, probably due to residual motion. The use of more advanced motion compensation techniques and more motion tolerant k-space trajectories could reduce the residual motion and further improve the precision in these segments.

Parallel imaging has been used to accelerate the acquisition, however more advanced undersampling techniques such as compressed sensing (93) would permit to achieve

higher acceleration factors and consequently may further improve image resolution (75). In the current study, a Cartesian trajectory has been used for the 3D SASHA image acquisition. However, non-Cartesian trajectories may be more robust to motion, and may permit a further improvement in the image quality of the T1-weighted images as well as the T1 map.

9.5 Conclusion

This study proposed a new approach for respiratory motion correction for 3D free-breathing myocardial T1 mapping, using a fat image-based navigator. The proposed fat-iNAV permits to correctly estimate the respiratory motion of the heart, guaranteeing 100% respiratory scan efficiency and predictable scan time, as well as isotropic resolution.

Chapter 10 – Conclusion and future work

10.1 Conclusion

This PhD thesis introduces a novel imaging technique for 3D myocardial T1 mapping, called 3D SASHA (10). This technique permits to image the whole-heart in free breathing, with high accuracy and improved precision compared to the conventional 2D SASHA sequence. Different approaches to further improve the precision and to accelerate the acquisition of the 3D SASHA technique are also presented in this thesis.

Myocardial T1 mapping is a powerful diagnostic and prognostic technique for different cardiomyopathies. Compared to the late gadolinium enhancement, it permits to visualize both the presence of local and diffuse fibrosis (**Chapter 2**). **Chapter 3** gives an overview of the different T1 mapping imaging techniques that have been proposed in the last years. Different prepulses and acquisition schemes have been investigated in order to achieve the best compromise between acquisition time, image resolution, accuracy and precision of the T1 measurements. Initially 2D T1 mapping imaging sequences have been proposed, however a free-breathing 3D quantitative T1 mapping would benefit from a complete myocardial coverage with higher SNR and spatial resolution than a 2D acquisition. In **Chapter 6** a 3D saturation-recovery based (3D SASHA) T1 mapping technique is

proposed (10), which allows for whole coverage of the left ventricle with increased image resolution compared to the 2D MOLLI (5) and 2D SASHA (6) imaging techniques. 3D SASHA also permits to achieve higher accuracy and improved precision compared to the 2D SASHA acquisition.

A 3D acquisition can be challenging since it requires longer scan time and consequently a free-breathing acquisition is mandatory. **Chapter 4** illustrates the different approaches that have been proposed for respiratory motion compensation. The 1D diaphragmatic navigator has been widely used in cardiac MR, since it can be easily combined with different cardiovascular imaging sequences and it is relatively easy to use. The 3D SASHA technique presented in **Chapter 6** is combined with the 1D dNAV for respiratory motion compensation, allowing free-breathing acquisition of the whole left ventricle (10). However the 1D dNAV has some limitations, since the maximum navigator efficiency achievable is of approximately 50%, prolonging the duration of the acquisition, and the respiratory motion of the heart are estimated from the lung-liver interface thus rewiring a motion model. These limitations can be overcome with the image-based navigator technique, which allows to estimate the respiratory motion of the heart from the heart itself (45).

Chapter 9 combines the previous 3D SASHA imaging sequence with a fat-iNAV for respiratory motion compensation. While with the conventional image-based navigator techniques both the water and fat signal are excited to obtain low-resolution images of the heart at every heartbeat, with the fat-iNAV only the myocardial fat signal is excited and used to track the translational respiratory motion of the heart (49). Compared to the conventional water navigator, the fat-selective navigator measure a more constant signal at different saturation delays and this ensures a correct estimation of the respiratory motion of the heart. This work demonstrates that the fat-iNAV permits to correctly

estimate the respiratory motion of the heart and to correct the single T1-weighted images, without interfering with the T1 quantification. In addition, the fat-iNAV guarantees 100% scan efficiency, with predictable scan time and higher isotropic image resolution.

Another important aspect of myocardial T1 mapping is the trade-off between accuracy and precision of the T1 quantification. 3D SASHA shows high accuracy in the T1 estimation, however the precision of the T1 measurement is still lower compared to the most clinically used 2D MOLLI techniques. Post-processing denosing method (**Chapter 5**) could help to reduce the noise of the images, improve the precision and the image quality of the T1 maps. A denoising technique based on a Beltrami regularization has been recently proposed for the 2D SASHA imaging sequence, showing good improvements in terms of noise reduction (61). This denoising approach has been extended to a 3D application and it has been successfully applied on the 3D SASHA imaging sequence (**Chapter 7**). The 3D Beltrami denoising permits to preserve the accuracy of the 3D SASHA acquisition, while considerably improving the precision, which becomes comparable to the one of the 2D MOLLI technique.

Chapter 8 extends the use of the 3D Beltrami denoising method to accelerate the 3D SASHA acquisition. A reduced number of saturation time points used for the fitting process of the 3D SASHA sequence are acquired, shortening the scan time from 12 to 7 minutes. The 3D Beltrami denoising technique is then used as a post-processing step to recover the loss in precision, without affecting the T1 accuracy.

10.2 Future work

The characterization of the myocardial tissues can provide important information for the diagnosis of different cardiomyopathies. Myocardial T1 mapping has played a crucial role in the non-invasive tissue characterization of the myocardium, with the potential of

replacing invasive biopsy (17). Different T1 mapping imaging techniques have been proposed in the last years, which investigate the best way to achieve accurate and precise myocardial T1 maps, in the shortest acquisition time and with the higher volumetric coverage. The use of a saturation recovery prepulse to generate T1-weighting has shown in the 2D SASHA imaging technique advantages in terms of accuracy compared to the inversion-recovery based 2D MOLLI technique. This has been confirmed by the 3D SASHA imaging sequence presented in this work, which allows also 3D coverage of the heart in free-breathing. There is another interesting approach for T1 mapping that has been proposed by Weingartner et al. (7), called SAPPHIRE imaging sequence, which combines the use of the saturation and inversion recovery prepulses. This technique showed improvement in both accuracy and precision compared to the other available T1 mapping techniques (9), however it has only been implemented for a 2D single-shot acquisition in breath-hold. The SAPPHIRE acquisition could be extended to a 3D implementation using the approach proposed for the 3D SASHA imaging sequence, which would combine the advantage of high accurate and precise T1 measurements with a whole coverage of the heart in free-breathing.

The 3D SASHA sequence proposed in Chapter 6 and Chapter 9 uses a Cartesian trajectory for the acquisition. Instead further study on alternative sampling trajectories, such as radial or spiral, should be considered in the future. To accelerate the acquisition SENSE parallel imaging has been used with an acceleration factor of 2. More advanced acceleration technique, such as compressed sensing and low-rank (94,95), could allow a faster acquisition and consequently a further improvement in the image resolution.

Chapter 9 presents the 3D SASHA imaging sequence combined with the fat-iNAV for respiratory motion compensation. Only FH and RL displacements were estimated from the image navigators and used to correct the T1-weighetd images. However a non-rigid

approach would better describe the respiratory motion of the heart, allowing further improvements in the image quality of the images (52).

In order to reduce the noise and improve the precision of the 3D SASHA T1 maps, the 3D Beltrami denoising method has been used in this PhD thesis. The denoising method was used as a post-processing step, applied directly on the reconstructed motion corrected T1-weighted images. Instead the integration of the denoising algorithm in the reconstruction step would further accelerate the acquisition and it would also simplify the whole framework.

The methods proposed in this thesis were tested and validated on a T1 phantom and on healthy volunteers. Future works will validate the methods on clinical studies with patient with different cardiovascular diseases.

Bibliography

1. Burt JR, Zimmerman SL, Kamel IR, Halushka M, Bluemke DA. Myocardial T1 mapping: Techniques and Potential Applications. RSNA [Internet] 2014.

2. Kramer CM. The Role of CMR in Cardiomyopathies. J. Nucl. Med. [Internet] 2015;56:39S–45S. doi: 10.2967/jnumed.114.142729.

3. Doltra A, Amundsen BH, Gebker R, Fleck E, Kelle S. Emerging concepts for myocardial late gadolinium enhancement MRI. Curr. Cardiol. Rev. 2013;9:185–190.

4. Gulani V, Calamante F, Shellock FG, Kanal E, Reeder SB. Gadolinium deposition in the brain: summary of evidence and recommendations. Lancet. Neurol. 2017;16:564–570. doi: 10.1016/S1474-4422(17)30158-8.

5. Messroghli DR, Radjenovic A, Kozerke S, Higgins DM, Sivananthan MU, Ridgway JP. Modified Look-Locker inversion recovery (MOLLI) for high-resolutionT1 mapping of the heart. Magn. Reson. Med. 2004;52:141–146. doi: 10.1002/mrm.20110.

6. Chow K, Flewitt JA, Green JD, Pagano JJ, Friedrich MG, Thompson RB. Saturation recovery single-shot acquisition (SASHA) for myocardial T 1 mapping. Magn. Reson. Med. 2014;71:2082–2095. doi: 10.1002/mrm.24878.

7. Weing S, Akc M, Basha T, Kissinger K V, Goddu B, Berg S, Manning WJ, Nezafat R. Combined Saturation / Inversion Recovery Sequences for Improved Evaluation of Scar and Diffuse Fibrosis in Patients with Arrhythmia or Heart Rate Variability. Magn. Reson. Med. 2014;1034:1024–1034. doi: 10.1002/mrm.24761.

8. Weingartner S, Moeller S, Schmitter S, Auerbach E, Kellman P, Shenoy C, Akcakaya M. Simultaneous multislice imaging for native myocardial T1 mapping: Improved spatial coverage in a single breath-hold. Magn. Reson. Med. 2017;78:462–471. doi: 10.1002/mrm.26770.

9. Roujol S, Weingärtner S, Foppa M, Chow K, Kawaji K, Ngo LH, Kellman P,

Manning WJ, Thompson RB, Nezafat R. Accuracy, Precision, and Reproducibility of Four T1 Mapping Sequences: A Head-to-Head Comparison of MOLLI, ShMOLLI, SASHA and SAPPHIRE. Radioloy 2014;272.

10. Nordio G, Henningsson M, Chiribiri A, Villa ADM, Schneider T, Botnar RM. 3D myocardial T_1 mapping using saturation recovery. J. Magn. Reson. Imaging 2017:1–10. doi: 10.1002/jmri.25575.

11. Nordio G, Bustin A, Henningsson MOS, Odille F, Prieto Vasquez C, Botnar RM. 3D SASHA myocardial T1 mapping with high accuracy and improved precision. In: Magnetic Resonance Materials in Phyisics, Biology and Medicine. ; 2018.

12. Fan D, Takawale A, Lee J, Kassiri Z. Cardiac fibroblasts, fibrosis and extracellular matrix remodeling in heart disease. Fibrogenesis Tissue Repair 2012;5:15. doi: 10.1186/1755-1536-5-15.

13. Krenning G, Zeisberg EM, Kalluri R. The origin of fibroblasts and mechanism of cardiac fibrosis. J. Cell. Physiol. 2010;225:631–637. doi: 10.1002/jcp.22322.

14. Valiente-Alandi I, Schafer AE, Blaxall BC. Extracellular matrix-mediated cellular communication in the heart. J. Mol. Cell. Cardiol. [Internet] 2016;91:228–237. doi: 10.1016/j.yjmcc.2016.01.011.

15. Pattanayak P, Bleumke DA. Tissue characterization of the myocardium: state of the art characterization by magnetic resonance and computed tomography imaging. Radiol. Clin. North Am. 2015;53:413–423. doi: 10.1016/j.rcl.2014.11.005.

16. Kellman P, Hansen MS. T1-mapping in the heart: accuracy and precision. J. Cardiovasc. Magn. Reson. [Internet] 2014;16:2. doi: 10.1186/1532-429X-16-2.

17. Radenkovic D, Weingartner S, Ricketts L, Moon JC, Captur G. T1 mapping in cardiac MRI. Heart Fail. Rev. 2017;22:415–430. doi: 10.1007/s10741-017-9627-2.

18. Haaf P, Garg P, Messroghli DR, Broadbent DA, Greenwood JP, Plein S. Cardiac T1

Mapping and Extracellular Volume (ECV) in clinical practice: a comprehensive review. J. Cardiovasc. Magn. Reson. [Internet] 2016;18:89. doi: 10.1186/s12968-016-0308-4.

19. Cannao PM, Altabella L, Petrini M, Ali M, Secchi F, Sardanelli F. Novel cardiac magnetic resonance biomarkers: native T1 and extracellular volume myocardial mapping. Eur. Heart J. Suppl. 2016;18:E64–E71. doi: 10.1093/eurheartj/suw022.

20. Liang Z, Lauterbur PC. Principles of Magnetic Resonance Imaging. IEEE Press; 2000.

21. Syed A. M, Raman V. S, Simonetti P. O. Basic Principles of Cardiovascula MRI. Springer; 2015.

22. McRobbie W. D, Moore A. E, Graves J. M, Prince R. M. MRI From Picture to Proton. Second. (Press CU, editor.).; 2006.

23. Mewton N, Liu C, Croisille P, Bluemke D, Lima J. Assessment of Myocardial Fibrosis with Cardiac Magnetic Resonance. J Am Coll Cardio 2012;57:891–903. doi: 10.1016/j.jacc.2010.11.013.Assessment.

24. Timothy D.W. Claridge. High-Resolution NMR Techniques in Organic Chemistry. Third Edit.; 2016.

25. Elster AD, Burdette JH. Questions and answers in magnetic resonance imaging. Second edi.; 2001.

26. Lota AS, Gatehouse PD, Mohiaddin RH. T2 mapping and T2* imaging in heart failure. Heart Fail. Rev. 2017;22:431–440. doi: 10.1007/s10741-017-9616-5.

27. Bieri O, Scheffler K. Fundamentals of balanced steady state free precession MRI. J. Magn. Reson. Imaging 2013;38:2–11. doi: 10.1002/jmri.24163.

28. Look D, R. Locker D. Time saving in measurement of NMR and EPR relaxation times. 1970. doi: 10.1063/1.1684482.

29. Flacke SJ, Fischer SE, Lorenz CH. Measurement of the gadopentetate dimeglumine

partition coefficient in human myocardium in vivo: normal distribution and elevation in acute and chronic infarction. Radiology 2001;218:703–710. doi: 10.1148/radiology.218.3.r01fe18703.

30. Scheffler K, Hennig J. T(1) quantification with inversion recovery TrueFISP. Magn. Reson. Med. 2001;45:720–723.

31. Piechnik SK, Ferreira VM, Dall'Armellina E, Cochlin LE, Greiser A, Neubauer S, Robson MD. Shortened Modified Look-Locker Inversion recovery (ShMOLLI) for clinical myocardial T1-mapping at 1.5 and 3 T within a 9 heartbeat breathhold. J. Cardiovasc. Magn. Reson. 2010;12:69. doi: 10.1186/1532-429X-12-69.

32. Ma D, Gulani V, Seiberlich N, Liu K, Sunshine JL, Duerk JL, Griswold MA. Magnetic resonance fingerprinting. Nature 2013;495:187–192. doi: 10.1038/nature11971.

33. Weigel M. Extended phase graphs: dephasing, RF pulses, and echoes - pure and simple. J. Magn. Reson. Imaging 2015;41:266–295. doi: 10.1002/jmri.24619.

34. Panda A, Mehta BB, Coppo S, Jiang Y, Ma D, Seiberlich N, Griswold MA, Gulani V. Magnetic Resonance Fingerprinting-An Overview. Curr. Opin. Biomed. Eng. 2017;3:56–66. doi: 10.1016/j.cobme.2017.11.001.

35. Weingartner S, Roujol S, Akcakaya M, Basha TA, Nezafat R. Free-breathing multislice native myocardial T1 mapping using the slice-interleaved T1 (STONE) sequence. Magn. Reson. Med. 2014. doi: 10.1002/mrm.25387.

36. Weingartner S, Akcakaya M, Roujol S, Basha T, Stehning C, Kissinger K V, Goddu B, Berg S, Manning WJ, Nezafat R. Free-breathing post-contrast three-dimensional T1 mapping: Volumetric assessment of myocardial T1 values. Magn. Reson. Med. 2015;73:214–222. doi: 10.1002/mrm.25124.

37. Santelli C, Nezafat R, Goddu B, Manning WJ, Smink J, Kozerke S, Peters DC.

Respiratory bellows revisited for motion compensation: preliminary experience for cardiovascular MR. Magn. Reson. Med. 2011;65:1097–1102. doi: 10.1002/mrm.22687.

38. Henningsson M, Botnar RM. Advanced Respiratory Motion Compensation for Coronary MR Angiography. Sensors (Basel) 2013:6882–6899. doi: 10.3390/s130606882.

39. Ehman RL, Felmlee JP. Adaptive technique for high-definition MR imaging of moving structures. Radiology 1989;173:255–263. doi: 10.1148/radiology.173.1.2781017.

40. Piccini D, Littmann A, Nielles-Vallespin S, Zenge MO. Respiratory self-navigation for whole-heart bright-blood coronary MRI: methods for robust isolation and automatic segmentation of the blood pool. Magn. Reson. Med. 2012;68:571–579. doi: 10.1002/mrm.23247.

41. Sachs TS, Meyer CH, Hu BS, Kohli J, Nishimura DG, Macovski A. Real-time motion detection in spiral MRI using navigators. Magn. Reson. Med. 1994;32:639–645.

42. Danias PG, McConnell M V, Khasgiwala VC, Chuang ML, Edelman RR, Manning WJ. Prospective navigator correction of image position for coronary MR angiography. Radiology 1997;203:733–736. doi: 10.1148/radiology.203.3.9169696.

43. Hamdan A, Asbach P, Wellnhofer E, Klein C, Gebker R, Kelle S, Kilian H, Huppertz A, Fleck E. A prospective study for comparison of MR and CT imaging for detection of coronary artery stenosis. JACC. Cardiovasc. Imaging 2011;4:50–61. doi: 10.1016/j.jcmg.2010.10.007.

44. Larson AC, White RD, Laub G, McVeigh ER, Li D, Simonetti OP. Self-gated cardiac cine MRI. Magn. Reson. Med. 2004;51:93–102. doi: 10.1002/mrm.10664.

45. Henningsson M, Smink J, Razavi R, Botnar RM. Prospective respiratory motion correction for coronary MR angiography using a 2D image navigator. Magn. Reson.

Med. 2013;69:486–494. doi: 10.1002/mrm.24280.

46. Scott AD, Keegan J, Firmin DN. Beat-to-beat respiratory motion correction with near 100% efficiency: a quantitative assessment using high-resolution coronary artery imaging. Magn. Reson. Imaging 2011;29:568–578. doi: 10.1016/j.mri.2010.11.004.

47. Henningsson M, Prieto C, Chiribiri A, Vaillant G, Razavi R, Botnar RM. Whole-heart coronary MRA with 3D affine motion correction using 3D image-based navigation. Magn. Reson. Med. 2014;71:173–181. doi: 10.1002/mrm.24652.

48. Henningsson M, Koken P, Stehning C, Razavi R, Prieto C. Whole-Heart Coronary MR Angiography With 2D Self-Navigated Image Reconstruction. Magn. Reson. Med. 2012;445:437–445. doi: 10.1002/mrm.23027.

49. Kawaji K, Spincemaille P, Nguyen TD, Thimmappa N, Cooper MA, Prince MR, Wang Y. Direct coronary motion extraction from a 2D fat image navigator for prospectively gated coronary MR angiography. Magn. Reson. Med. 2014;71:599–607. doi: 10.1002/mrm.24698.

50. Keegan J, Gatehouse PD, Yang G-Z, Firmin DN. Non-model-based correction of respiratory motion using beat-to-beat 3D spiral fat-selective imaging. J. Magn. Reson. Imaging 2007;26:624–629. doi: 10.1002/jmri.20941.

51. Pruessmann KP, Weiger M, Bornert P, Boesiger P. Advances in sensitivity encoding with arbitrary k-space trajectories. Magn. Reson. Med. 2001;46:638–651.

52. Cruz G, Atkinson D, Henningsson M, Botnar RM, Prieto C. Highly efficient nonrigid motion-corrected 3D whole-heart coronary vessel wall imaging. Magn. Reson. Med. 2017;77:1894–1908. doi: 10.1002/mrm.26274.

53. Batchelor PG, Atkinson D, Irarrazaval P, Hill DLG, Hajnal J, Larkman D. Matrix description of general motion correction applied to multishot images. Magn. Reson. Med. 2005;54:1273–1280. doi: 10.1002/mrm.20656.

54. Glover GH, Pauly JM. Projection reconstruction techniques for reduction of motion effects in MRI. Magn. Reson. Med. 1992;28:275–289.

55. Liao JR, Pauly JM, Brosnan TJ, Pelc NJ. Reduction of motion artifacts in cine MRI using variable-density spiral trajectories. Magn. Reson. Med. 1997;37:569–575.

56. Pruessmann KP, Weiger M, Scheidegger MB, Boesiger P. SENSE: sensitivity encoding for fast MRI. Magn. Reson. Med. 1999;42:952–962.

57. Griswold MA, Jakob PM, Heidemann RM, Nittka M, Jellus V, Wang J, Kiefer B, Haase A. Generalized autocalibrating partially parallel acquisitions (GRAPPA). Magn. Reson. Med. 2002;47:1202–1210. doi: 10.1002/mrm.10171.

58. Tikhonov AN. Solution of incorrectly formulated problems and the regularization method. Sov. Math. 1963;4:1035–1038.

59. Rudin LI, Osher S, Fatemi E. Nonlinear total variation based noise removal algorithms. Phys. D Nonlinear Phenom. [Internet] 1992;60:259–268. doi: https://doi.org/10.1016/0167-2789(92)90242-F.

60. Kimmel R, Malladi R, Sochen N. Images as Embedded Maps and Minimal Surfaces: Movies, Color, Texture, and Volumetric Medical Images. Int. J. Comput. Vis. [Internet] 2000;39:111–129. doi: 10.1023/A:1008171026419.

61. Bustin A, Ferry P, Codreanu A, Beaumont M, Liu S, Burschka D, Felblinger J, Brau ACS, Menini A, Odille F. Impact of denoising on precision and accuracy of saturation-recovery-based myocardial T1 mapping. J. Magn. Reson. Imaging 2017. doi: 10.1002/jmri.25684.

62. Cerqueira MD, Weissman NJ, Dilsizian V, Jacobs AK, Kaul S, Laskey WK, Pennell DJ, Rumberger JA, Ryan T, Verani MS. Standardized Myocardial Segmentation and Nomenclature for Tomographic Imaging of the Heart. Circ. Cardiovasc. Imaging 2002:539–542.

63. Messroghli DR, Radjenovic A, Kozerke S, Higgins DM, Sivananthan MU, Ridgway JP. Modified look-locker inversion recovery (MOLLI) for high-resolution T 1 mapping of the heart. Magn. Reson. Med. 2004;52:141–146. doi: 10.1002/mrm.20110.

64. Coniglio A, Di Renzi P, Vilches Freixas G, et al. Multiple 3D inversion recovery imaging for volume T1 mapping of the heart. Magn. Reson. Med. 2013;69:163–170. doi: 10.1002/mrm.24248.

65. Clique H, Cheng H-LM, Marie P-Y, Felblinger J, Beaumont M. 3D myocardial T1 mapping at 3T using variable flip angle method: pilot study. Magn. Reson. Med. 2014;71:823–829. doi: 10.1002/mrm.24688.

66. Ogg RJ, Kingsley PB, Taylor JS. WET, a T1- and B1-insensitive water-suppression method for in vivo localized 1H NMR spectroscopy. J. Magn. Reson. B 1994;104:1–10. doi: 10.1006/jmrb.1994.1048.

67. Captur G, Gatehouse P, Kellman P, et al. A T1 and ECV phantom for global T1 mapping quality assurance: The T1 mapping and ECV standardisation in CMR (T1MES) program. J. Cardiovasc. Magn. Reson. [Internet] 2016;18:1–3. doi: 10.1186/1532-429X-18-S1-W14.

68. Barral J k., Gudmundson E, Stikov N, Etezadi-Amoli M, Stoica P, Nishimura DG. A Robust Methodology of In Vivo T1 Mapping. Magn. Reson. Med. 2010;64:1057–1067. doi: 10.1002/mrm.22497.

69. Etienne A, Botnar M, Muiswinkel AMC Van, Boesiger P, Manning WJ, Stuber M. " Soap-Bubble " Visualization and Quantitative Analysis of 3D Coronary Magnetic Resonance Angiograms. 2002;666:658–666. doi: 10.1002/mrm.10253.

70. McHugh ML. Interrater reliability: the kappa statistic. Biochem. Medica [Internet] 2012;22:276–282.

71. Stehning C, Bo P, Nehrke K, Eggers H, Stuber M. Free-Breathing Whole-Heart

Coronary MRA With 3D Radial SSFP and Self-Navigated Image Reconstruction. 2005;480:476–480. doi: 10.1002/mrm.20557.

72. Aitken AP, Henningsson M, Botnar RM, Schaeffter T, Prieto C. 100% Efficient three-dimensional coronary MR angiography with two-dimensional beat-to-beat translational and bin-to-bin affine motion correction. Magn. Reson. Med. 2015;74:756–764. doi: 10.1002/mrm.25460.

73. Rogers T, Dabir D, Mahmoud I, Voigt T, Schaeffter T, Nagel E, Puntmann VO. Standardization of T1 measurements with MOLLI in differentiation between health and disease – the ConSept study. J. Cardiovasc. Magn. Reson. [Internet] 2013;15:1. doi: 10.1186/1532-429X-15-78.

74. Mcdiarmid AK, Broadbent DA, Higgins DM, et al. The effect of changes to MOLLI scheme on T1 mapping and extra cellular volume calculation in healthy volunteers with 3 tesla cardiovascular magnetic resonance imaging. 2015;c:503–510. doi: 10.3978/j.issn.2223-4292.2015.04.07.

75. Doneva M, Börnert P, Eggers H, Stehning C, Sénégas J, Mertins A. Compressed Sensing Reconstruction for Magnetic Resonance Parameter Mapping. 2010;1120:1114–1120. doi: 10.1002/mrm.22483.

76. Roujol S, Foppa M, Weingartner S, Manning WJ, Nezafat R. Adaptive registration of varying contrast-weighted images for improved tissue characterization (ARCTIC): application to T1 mapping. Magn. Reson. Med. 2015;73:1469–1482. doi: 10.1002/mrm.25270.

77. Jang J, Nakamori S, Nezafat R. Improving precision of myocardial T1 mapping with 3-parameter model using tissue characteristic-based denoising. In: Proceedings of the 25th Annual Meeting of ISMRM Hawaii USA. ; 2017.

78. Zosso D, Bustin A. A primal-dual projected gradient algorithm for efficient

Beltrami regularization. UCLA CAM Rep. 2014:14–52.

79. Kimmel R, Sochen N, Malladi R. From high energy physics to low level vision. Scale-sp. Theory Comput. Vis. 1997;1252:236–247. doi: 10.1007/3-540-63167-4_18.

80. Zhu M, Chan T. An efficient primal-dual hybrid gradient algorithm for total variation image restoration, Tech. rep., UCLA CAM report 08-34. 2008.

81. Gai ND, Stehning C, Nacif M, Bluemke DA. Modified Look-Locker T1 evaluation using Bloch simulations: human and phantom validation. Magn. Reson. Med. 2013;69:329–336. doi: 10.1002/mrm.24251.

82. Rogers T, Dabir D, Mahmoud I, Voigt T, Schaeffter T, Nagel E, Puntmann VO. Standardization of T1 measurements with MOLLI in differentiation between health and disease – the ConSept study. J. Cardiovasc. Magn. Reson. [Internet] 2013;15:78. doi: 10.1186/1532-429X-15-78.

83. Wang X, Joseph AA, Kalentev O, Merboldt K-D, Voit D, Roeloffs VB, van Zalk M, Frahm J. High-resolution myocardial T1 mapping using single-shot inversion recovery fast low-angle shot MRI with radial undersampling and iterative reconstruction. Br. J. Radiol. 2016;89:20160255. doi: 10.1259/bjr.20160255.

84. Stainsby JA, Zhang L, Wright GA. Accelerated myocardial T1 mapping using SMART1Map and compressed sensing with temporal PCA. J. Cardiovasc. Magn. Reson. [Internet] 2014;16:O9. doi: 10.1186/1532-429X-16-S1-O9.

85. Chen X, Mehta B, Salerno M, Epstein F. High Resolution Myocardial T1 Mapping Using MOLLI with Parallel Imaging and Compressed Sensing. In: In Proceedings of the 21st Annual Meeting of ISMRM, Salt Lake City, Utah. ; 2013.

86. Moghari MH, Roujol S, Chan RH, et al. Free-breathing 3D cardiac MRI using iterative image-based respiratory motion correction. Magn. Reson. Med. 2013;70:1005–1015. doi: 10.1002/mrm.24538.

87. Akcakaya M, Weingartner S, Roujol S, Nezafat R. On the selection of sampling points for myocardial T1 mapping. Magn. Reson. Med. 2015;73:1741–1753. doi: 10.1002/mrm.25285.

88. Weingartner S, Akcakaya M, Roujol S, Basha T, Tschabrunn C, Berg S, Anter E, Nezafat R. Free-breathing combined three-dimensional phase sensitive late gadolinium enhancement and T1 mapping for myocardial tissue characterization. Magn. Reson. Med. 2015;74:1032–1041. doi: 10.1002/mrm.25495.

89. Ginami G, Neji R, Phinikaridou A, Whitaker J, Botnar RM, Prieto C. Simultaneous bright- and black-blood whole-heart MRI for noncontrast enhanced coronary lumen and thrombus visualization. Magn. Reson. Med. 2018;79:1460–1472. doi: 10.1002/mrm.26815.

90. Wu HH, Gurney PT, Hu BS, Nishimura DG, McConnell M V. Free-breathing multiphase whole-heart coronary MR angiography using image-based navigators and three-dimensional cones imaging. Magn. Reson. Med. 2013;69:1083–1093. doi: 10.1002/mrm.24346.

91. Scott AD, Keegan J, Firmin DN. High-resolution 3D coronary vessel wall imaging with near 100% respiratory efficiency using epicardial fat tracking: reproducibility and comparison with standard methods. J. Magn. Reson. Imaging 2011;33:77–86. doi: 10.1002/jmri.22398.

92. Hauger O, Dumont E, Chateil J-F, Moinard M, Diard F. Water excitation as an alternative to fat saturation in MR imaging: preliminary results in musculoskeletal imaging. Radiology 2002;224:657–663. doi: 10.1148/radiol.2243011227.

93. Lustig M, Donoho D, Pauly JM. Sparse MRI: The application of compressed sensing for rapid MR imaging. Magn. Reson. Med. 2007;58:1182–1195. doi: 10.1002/mrm.21391.

94. Zhang T, Pauly JM, Levesque IR. Accelerating parameter mapping with a locally low rank constraint. Magn. Reson. Med. 2015;73:655–661. doi: 10.1002/mrm.25161.

95. He J, Liu Q, Christodoulou AG, Ma C, Lam F, Liang Z. Accelerated High-Dimensional MR Imaging With Sparse Sampling Using Low-Rank Tensors. IEEE Trans. Med. Imaging 2016;35:2119–2129. doi: 10.1109/TMI.2016.2550204.

96. Arai AE. The cardiac magnetic resonance (CMR) approach to assessing myocardial viability. J. Nucl. Cardiol. 2011;18:1095–1102. doi: 10.1007/s12350-011-9441-5.

97. Kellman P, Arai AE. Cardiac Imaging Techniques for Physicians: Late Enhancement. J. Magn. Reson. Imaging [Internet] 2012;36:529–542. doi: 10.1002/jmri.23605.

98. Larkman DJ, Nunes RG. Parallel magnetic resonance imaging. Phys. Med. Biol. 2007;52:R15–55. doi: 10.1088/0031-9155/52/7/R01.